University of Illinois at Urbana-Champaign

ACRC

Air Conditioning and Refrigeration Center A National Science Foundation/University Cooperative Research Center

Large Eddy Simulations of Particle Dispersion and Deposition in a Turbulent Square Duct Flow

C. M. Winkler, S. P. Vanka and P. S. Hrnjak

ACRC TR-203 October 2002

For additional information:

Air Conditioning and Refrigeration Center
University of Illinois
Mechanical & Industrial Engineering Dept.
1206 West Green Street
Urbana, IL 61801

(217) 333-3115

Prepared as part of ACRC Project #122
An Experimental and Computational Study
of Disperse Two-Phase Flow in Headers
P. S. Hrnjak and S. P. Vanka, Principal Investigators

The Air Conditioning and Refrigeration Center was founded in 1988 with a grant from the estate of Richard W. Kritzer, the founder of Peerless of America Inc. A State of Illinois Technology Challenge Grant helped build the laboratory facilities. The ACRC receives continuing support from the Richard W. Kritzer Endowment and the National Science Foundation. The following organizations have also become sponsors of the Center.

Alcan Aluminum Corporation
Amana Refrigeration, Inc.
Arçelik A. S.
Brazeway, Inc.
Carrier Corporation
Copeland Corporation
Dacor
Daikin Industries, Ltd.
Delphi Harrison Thermal Systems
General Motors Corporation
Hill PHOENIX
Honeywell, Inc.
Hydro Aluminum Adrian, Inc.
Ingersoll-Rand Company
Kelon Electrical Holdings Co., Ltd.
Lennox International, Inc.
LG Electronics, Inc.
Modine Manufacturing Co.
Parker Hannifin Corporation
Peerless of America, Inc.
Samsung Electronics Co., Ltd.
Tecumseh Products Company
The Trane Company
Valeo, Inc.
Visteon Automotive Systems
Wolverine Tube, Inc.
York International, Inc.

For additional information:

Air Conditioning & Refrigeration Center
Mechanical & Industrial Engineering Dept.
University of Illinois
1206 West Green Street
Urbana, IL 61801

217 333 3115

ABSTRACT

In the current dissertation work, the preferential concentration and deposition of heavy solid particles in a downward, fully developed turbulent square duct flow are studied using large eddy simulations. A second-order accurate, finite-volume based fractional step scheme, based on an unstructured Cartesian mesh, is used to integrate the unsteady, incompressible, three-dimensional Navier-Stokes equations. An algebraic multigrid solver is used to solve the Poisson equation resulting from the fractional step method. The subgrid stresses are modeled with a dynamic subgrid kinetic energy model. The particle equation of motion includes drag, lift and gravity forces and is integrated using the fourth-order accurate Runge-Kutta method. The Reynolds number for the square duct is 360, based on average friction velocity and duct width. The grid used is 80×80×128 in the two wall-normal and streamwise directions, respectively.

The preferential concentration of particles is studied assuming that the particles do not modify the turbulence and that particle-particle collisions are insignificant. The continuous and the dispersed phases are treated using Eulerian and Lagrangian approaches, respectively. Four cross-sectional locations representative of the time-mean secondary flow patterns and six particle response times were chosen to study the effect of location and particle inertia on preferential concentration. Variation of vorticity magnitude, swirling strength, strain-rate, and $\nabla\mathbf{u}:\nabla\mathbf{u}$, and their probability distribution functions(PDF), with particle response time and location is shown to demonstrate preferential concentration. Particles are seen to accumulate in regions of high $\nabla\mathbf{u}:\nabla\mathbf{u}$ and strain-rate and in regions of low swirling strength. In general, particles accumulate in regions of low vorticity magnitude. However, near the wall, large particles accumulate in regions of high vorticity magnitude. In addition, instantaneous contours of the above statistics and scatter plots of particle positions in a near-wall plane are presented to illustrate preferential concentration.

Deposition of particles in a square duct is the focus of the second set of simulations. Ten particle response times are studied. Simulations are carried out using one-way coupling as well as select cases using two- and four-way coupling. A particle-particle collision algorithm has been developed. PDFs of deposition location, average streamwise and wall-normal deposition velocities, and deposition rates are presented.

Table of Contents

Page

ABSTRACT i

List of Figures iv

List of Tables vii

Chapter 1. Introduction 1

1.1 Problem Description 2

1.2 Outline of the Thesis 3

Chapter 2. Motivation 4

2.1 Background 4

2.2 Experimental Setup 5

2.3 Experimental Results 6

2.4 Experimental Conclusions 8

Chapter 3. Literature Review 9

3.1 Large Eddy Simulation Models 9

3.2 Square Duct Flow 16

3.3 Non-Square Duct Wall Bounded Single Phase Flows 18

3.4 Gas-Particle Flows 22

3.4.1 Experiments 22

3.4.2 Computations 23

Chapter 4. Governing Equations and Numerical Methods 30

4.1 Governing Equations for the Large Eddy Simulations 30

4.2 Numerical Procedure for the Large Eddy Simulations 32

4.3 Particle Collisions 34

4.4 Validation of the Scheme 38

4.4.1 Channel Flow, Re_τ = 180 Results 39

4.4.2 Channel Flow, Re_τ = 590 Results 41

4.4.3 Summary of Code Validation 42

Chapter 5. Preferential Concentration Results 43

5.1 Visualization of Preferential Concentration in a Near-Wall Plane 44

5.2 Effect of vorticity magnitude 46

5.3 Effect of swirling strength 47

5.4 Effect of strain-rate 47

5.5 Effect of $\tilde{N}u:\tilde{N}u$ 48

Chapter 6. Deposition Results 50

6.1 One-way coupling 50

6.1.1 Wall-Normal Deposition Velocity 50

6.1.2 Streamwise Deposition Velocity 51

6.1.3 Deposition Location 51

6.1.4 Deposition Rates 52
6.2 Effects of Two-Way Coupling and Particle Collisions 52
6.2.1 Low volume fraction ($\phi_v \leq 10^{-4}$) 52
6.2.2 Higher volume fractions ($\phi_v = 10^{-3}$) 53
Chapter 7. Conclusions and Recommendations 55
7.1 Conclusions 55
7.2 Recommendations for Future Work 57
Tables 59
Figures 62
Bibliography 109

List of Figures

Page

Figure 1.1: Contours of Mean Streamwise Velocity 62
Figure 1.2: Mean Secondary Flows in a Square Duct 62
Figure 1.3: Instantaneous Secondary Flows in a Square Duct 63
Figure 2.2.1: Experimental Setup 63
Figure 2.3.1: Centerline Droplet Measurements for 1 g/s 64
Figure 2.3.2: Centerline Droplet Measurements for 2 g/s 64
Figure 2.3.3: Centerline Droplet Measurements for 3 g/s 65
Figure 2.3.4: Centerline Number Density Measurements for 2 g/s, 10% Quality 65
Figure 2.3.5: Size and Velocity Distributions at 60 mm Downstream, 2 g/s, 10% Quality 66
Figure 2.3.6: Size and Velocity Distributions at 80 mm Downstream, 2 g/s, 10% Quality 67
Figure 2.3.7: Size and Velocity Distributions at 100 mm Downstream, 2 g/s, 10% Quality 68
Figure 2.3.8: Size and Velocity Distributions at 120 mm Downstream, 2 g/s, 10% Quality 69
Figure 2.3.9: Distribution Results for 15 g/s, 10% Quality with 3/8" Pipe Inlet 70
Figure 2.3.10: Distribution Results for 15 g/s, 10% Quality with Atomizer Inlet 70
Figure 3.3.1: Example of Wall Boundary in Cut-Cell Logic 71
Figure 4.3.1: Schematic of Colliding Particles 71
Figure 4.4.1: Dynamic Model Grid Logic, 2-Dimensional 72
Figure 4.4.1.2: urms, Channel Flow, Re_τ=180 73
Figure 4.4.1.3: vrms, Channel Flow, Re_τ=180 73
Figure 4.4.1.4: wrms, Channel Flow, Re_τ=180 74
Figure 4.4.1.5: $u'v'$, Channel Flow, Re_τ=180 74
Figure 4.4.1.6: Mean sgs k, Channel Flow, Re_τ=180 75
Figure 4.4.1.7: Mean ν_T, Channel Flow, Re_τ=180 75
Figure 4.4.1.8: Mean C_τ, Channel Flow, Re_τ=180 76
Figure 4.4.1.9: Mean C_ε, Channel Flow, Re_τ=180 76
Figure 4.4.2.1: Mean Velocity Profiles, Channel Flow, Re_τ = 590 77
Figure 4.4.2.2: urms, Channel Flow, Re_τ = 590 77
Figure 4.4.2.3: vrms, Channel Flow, Re_τ = 590 78
Figure 4.4.2.4: wrms, Channel Flow, Re_τ = 590 78
Figure 4.4.2.5: $u'v'$, Channel Flow, Re_τ=590 79
Figure 4.4.2.6: sgsk, Channel Flow, Re_τ=590 79
Figure 4.4.2.7: Mean ν_T, Channel Flow, Re_τ=590 80
Figure 4.4.2.8: Mean C_τ, Channel Flow, Re_τ=590 80
Figure 4.4.2.9: Mean C_ε, Channel Flow, Re_τ=590 81
Figure 5.0.1: Comparison of Mean Streamwise Velocity at x = 0.5 81
Figure 5.0.2: Sampling Positions in Square Duct Cross-Section 82
Figure 5.1.1: Instantaneous Scatter Plot of Particle Positions for $\tau_p^+ = 0.25$, $7.05 \le y^+ \le 10.66$ 82
Figure 5.1.2: Instantaneous Scatter Plot of Particle Positions for $\tau_p^+ = 1.0$, $7.05 \le y^+ \le 10.66$ 82

Figure 5.1.3: Instantaneous Scatter Plot of Particle Positions for $\tau_p^+ = 8.0$, $7.05 \le y^+ \le 10.66$ 83
Figure 5.1.4: Instantaneous Contours of Streamwise Velocity at $y^+=8.85$ 83
Figure 5.1.5: Instantaneous Contours of ? at $y^+=8.85$ 83
Figure 5.1.6: Instantaneous Contours of λ_i at $y^+=8.85$ 83
Figure 5.1.7: Instantaneous Contours of σ_u at $y^+=8.85$ 83
Figure 5.1.8: Instantaneous Contours of $\nabla\mathbf{u}:\nabla\mathbf{u}$ at $y^+=8.85$ 84
Figure 5.1.9: Contours of λ_i at y^+ = (a) 1.76, (b) 35.09, (c) 177.18 84
Figure 5.1.10: Contours of σ_u at y^+ = (a) 1.76, (b) 35.09, (c) 177.18 85
Figure 5.1.11: Contours of $\nabla\mathbf{u}:\nabla\mathbf{u}$ at y^+ = (a) 1.76, (b) 35.09, (c) 177.18 86
Figure 5.1.12: Instantaneous Cross-Sectional Contours of λ_i 87
Figure 5.1.13: Instantaneous Cross-Sectional Contours of σ_u 87
Figure 5.1.14: Instantaneous Cross-Sectional Contours of $\nabla\mathbf{u}:\nabla\mathbf{u}$ 88
Figure 5.2.1: Mean Values of ω in the Near Wall Region ($x^+=177.2$, $y^+=19.8$) 88
Figure 5.2.2: Mean Values of ω in the Vortex Center Region ($x^+=76.7$, $y^+=31.2$) 89
Figure 5.2.5: PDFs of ω in the Near Wall Region ($x^+=177.2$, $y^+=19.8$) 90
Figure 5.2.6: PDFs of ω in the Vortex Center Region ($x^+=76.7$, $y^+=31.2$) 91
Figure 5.2.7: PDFs of ω in the Saddle Region ($x^+=59.5$, $y^+=59.5$) 91
Figure 5.2.8: PDFs of ω in the Duct Center Region ($x^+=177.2$, $y^+=177.2$) 92
Figure 5.3.1: Mean Values of λ_i 92
Figure 5.3.2: PDFs of λ_i in the Near Wall Region ($x^+=177.2$, $y^+=19.8$) 93
Figure 5.3.3: PDFs of λ_i in the Vortex Center Region ($x^+=76.7$, $y^+=31.2$) 93
Figure 5.3.4: PDFs of λ_i in the Saddle Region ($x^+=59.5$, $y^+=59.5$) 94
Figure 5.3.5: PDFs of λ_i in the Duct Center Region ($x^+=177.2$, $y^+=177.2$) 94
Figure 5.4.1: Mean Values of σ_u 95
Figure 5.4.2: PDFs of σ_u in the Near Wall Region ($x^+=177.2$, $y^+=19.8$) 95
Figure 5.4.3: PDFs of σ_u in the Vortex Center Region ($x^+=76.7$, $y^+=31.2$) 96
Figure 5.4.4: PDFs of σ_u in the Saddle Region ($x^+=59.5$, $y^+=59.5$) 96
Figure 5.4.5: PDFs of σ_u in the Duct Center Region ($x^+=177.2$, $y^+=177.2$) 97
Figure 5.5.1: Mean Values of $\nabla\mathbf{u}:\nabla\mathbf{u}$ 97
Figure 5.5.2: PDFs of $\nabla\mathbf{u}:\nabla\mathbf{u}$ in the Near Wall Region ($x^+=177.2$, $y^+=19.8$) 98
Figure 5.5.3: PDFs of $\nabla\mathbf{u}:\nabla\mathbf{u}$ in the Vortex Center Region ($x^+=76.7$, $y^+=31.2$) 98
Figure 5.3.4: PDFs of $\nabla\mathbf{u}:\nabla\mathbf{u}$ in the Saddle Region ($x^+=59.5$, $y^+=59.5$) 99
Figure 5.5.5: PDFs of $\nabla\mathbf{u}:\nabla\mathbf{u}$ in the Duct Center Region ($x^+=177.2$, $y^+=177.2$) 99
Figure 6.1.1.1: Wall-Normal Deposition Velocity, $\rho_p/\rho_f = 1000$, One-way Coupling 100
Figure 6.1.1.2: Wall-Normal Deposition Velocity, $\rho_p/\rho_f = 8900$, One-way Coupling 100
Figure 6.1.2.1: Streamwise Deposition Velocity, $\rho_p/\rho_f = 1000$, One-way Coupling 101
Figure 6.1.2.2: Streamwise Deposition Velocity, $\rho_p/\rho_f = 8900$, One-way Coupling 101
Figure 6.1.3.1: PDFs of Deposition Location, $\rho_p/\rho_f = 1000$, One-way Coupling 102
Figure 6.1.3.2: PDFs of Deposition Location, $\rho_p/\rho_f = 8900$, One-way Coupling 102
Figure 6.1.4.1: Time History of Particle Deposition, $\rho_p/\rho_f = 1000$, One-way Coupling 103

Figure 6.1.4.2: Time History of Particle Deposition, $\rho_p/\rho_f = 8900$, One-way Coupling 103
Figure 6.2.2.1: Wall-Normal Deposition Velocity, Four-way Coupling, 10^5 Initial Particles 104
Figure 6.2.1.2: Streamwise Deposition Velocity, Four-way Coupling, 10^5 Initial Particles 105
Figure 6.2.1.3: PDFs of Deposition Location, Four-way Coupling, 10^5 Initial Particles 105
Figure 6.2.1.4: Time History of Particle Deposition, Four-way Coupling, 10^5 Initial Particles 106
Figure 6.2.2.1: Wall-Normal Deposition Velocity, Two- and Four-way Coupling, Volume Fraction = 10^{-3} 106
Figure 6.2.2.2: Streamwise Deposition Velocity, Two- and Four-way Coupling, Volume Fraction = 10^{-3} 107
Figure 6.2.2.4: Time History of Particle Deposition, Two- and Four-way Coupling, Volume Fraction = 10^{-3} 108

List of Tables

Page

Table 2.2.1: PDPA Parameters 59
Table 2.2.2: Experimental Conditions 59
Table 5.1: Grid Spacing in Cross Section of Square Duct 60
Table 5.2: Particle Properties for Preferential Concentration Studies 61
Table 6.1: Particle Properties for Deposition Simulations 61

Chapter 1. Introduction

Computational fluid dynamics (CFD) has evolved as a widely used approach for the design of engineering equipment involving fluid flow, heat transfer, combustion and particle dynamics. Computational fluid dynamics involves the numerical solution of the partial-differential equations governing fluid flow, known as the Navier-Stokes equations. When the flow becomes turbulent, length scales of a wide range develop in the flow. It is this range of scales that presents one of the biggest problems in CFD. In order to solve the equations in a domain which contains both large and small scales, the computational grid must be fine enough to resolve the smallest scales. It is easy to see that the computational grid can become extremely large, thus requiring an enormous amount of computing time. To deal with this problem, several methods of solving the governing equations have been developed over the years, with each method having its own level of accuracy and level of detail provided by the solution. The most accurate and detailed solutions come from Direct Numerical Simulation (DNS). In DNS, all scales of motion are resolved and the equations are solved without empiricism. This is considered an "exact" method, since the only errors are from the numerical method itself. However, DNS requires vast amounts of computing time and resources which makes it impractical for all but the simplest flows.

The most widely used approach is known as Reynolds averaging, or Reynolds Averaged Navier-Stokes (RANS) methods, where the flow variables are decomposed into mean and fluctuating components and additional equations are developed for the kinetic energy and dissipation. This approach is heavily empirical since numerous constants appear in the modeled equations that must be tuned for every flow. A large amount of research in the past three decades concerning modeling of the Reynolds-stresses through algebraic and differential models has revealed the difficulty (and impossibility) of developing universally accurate models that can represent a wide spectrum of flows. The popular k-ε (Launder and Spalding 1972; Bardina, Huang, and Coakley 1997; Menter 1994; Thangam and Speziale 1992), Reynolds-stress models (Launder, Reece, and Rodi 1975), and nonlinear k-ε models (Speziale 1987) have had limited success in predicting important quantities such as heat transfer, combustion, and particle transport. The principal difficulty has been the representation of the large-scales of turbulence in a universal way across many engineering flows (Moin 1998). Thus, predictions from Reynolds-averaged models have only limited accuracy and can best be used for scoping new designs in a comparative sense without complete reliance on the quantitative accuracy of their performance. The advantage of such simulations, however, is that the required computational resources are very small, and considering current advances in computing hardware, very inexpensive. All current commercial CFD codes (such as FLUENT, CFX, STAR-CD, etc) rely on variations of this method. Often, the engineer does not have the knowledge, time or training to determine the proper choice of models and constants which appear in the vast array of RANS techniques. This leads to an inaccurate calculation which may be significantly far from the true solution.

In recent years, great strides have been made in computing hardware, architecture and software. While single processor speeds have significantly increased since the early days of turbulence modeling, new paradigms of computing based on parallel processing have matured. These combined with advances in parallel numerical algorithms that are robust and scalable provide enormous opportunities for large scale scientific computing. In the last decade, therefore, a new simulation approach for turbulent flows has evolved. The technique, called Large Eddy

Simulation (LES), is based on the premise of simulating the dynamics of the large-scale energy containing turbulence structures and modeling the small scales of turbulence (Lesieur and Metais 1996). Such small scales may be assumed to be isotropic, and universal across a variety of turbulent flows. Unlike DNS, LES is not restricted to simplistic flows. LES would therefore seem to be the best choice for studying complex turbulent flows since it requires less empiricism than RANS methods, yet can still reproduce the large-scale transient structures which dominate many engineering processes like mixing and particle transport.

A deeper understanding of particle transport can lead to more cost-effective paint coatings, better treatment of the inhalation of biological spores in lung branches, and improved designs of industrial clean rooms. Therefore it is important to have a sound understanding of this phenomenon. Computational fluid dynamics has become an important tool for studying particle dispersion in turbulent flows due to the ease with which quantities may be measured which often prove difficult, if not impossible, to measure experimentally. Attempts to predict particle-laden turbulent flows have resulted in computational techniques which can typically be classified as either Eulerian or Lagrangian. Eulerian methods envision the dispersed phase as a cloud and equations governing its momentum and continuity are derived and solved much like the carrier phase. In the Lagrangian method, individual particle trajectories are computed by solving the particle equation of motion. A recent review of computational methods for particle-laden flows is given by Loth (2000).

In geometries such as channels and pipes, multiple homogeneous directions exist which provide a large sample size when averaging statistics. However, in more complex geometries such as a square duct, only one homogeneous direction exists. This facilitates the need for long averaging times which increases the need for efficient solvers. In a square duct, secondary flows are known to exist which are directed towards the corners along the corner bisectors, and towards the center along the wall bisectors. Momentum and scalar quantities are convected along these flows towards the corners and back along the bounding walls. As a result, the contours of streamwise velocity are distorted such that they distort as shown in Fig. 1.1. These secondary flows, also known as Prandtl's second kind, are caused by gradients in the Reynolds stresses. The time mean secondary flows, shown in Fig. 1.2, are symmetric about an $n\pi/2$ rotation, where n is any integer. The instantaneous secondary flows, show in Fig. 1.3, are stronger and more complex. The square duct also has many practical engineering applications such as heat exchangers, ventilation, and turbomachinery (inlets and nozzles). The square duct is also of fundamental interest since it is more complex than channel or pipe flow. Improved turbulence models could be developed from a deeper understanding of the complex three-dimensionality of the square duct problem. Particle transport in a square duct represents many important engineering applications. Direct applications would include dust transport in ventilation systems and droplet transport in evaporators. Understanding how these particles, or droplets, are transported and deposited could lead to improved designs of heat exchanger equipment and better treatment of the inhalation of such toxins as anthrax. Typically, particle transport is studied in isotropic turbulence or in channel/pipe flow. However, it is of more direct engineering interest to understand particle transport in a square duct for the above reasons.

1.1 Problem Description

In this research work, both experimental and computational results are reported. The experimental portion of this thesis deals with Phase-Doppler Interferometry measurements of dispersed two-phase flow in the header of

an evaporator. The header geometry is a square duct, and represents an application where dispersed two-phase flow is of importance. The characterization of the refrigerant (R134a) spray provides the first set of data on R134a droplets formed from a pressure swirl atomizer. These data will provide HVAC researchers information on such topics as evaporation. The computational focus of this thesis involves particle transport in the fully-developed turbulent incompressible flow through a straight duct of square cross-section which was simulated using the Large Eddy Simulation (LES) technique. Preferential concentration of particles and particle deposition were examined through the Lagrangian particle tracking method. Previous particle-laden internal flows have focused on relatively simple geometries such as channels and pipes. Secondary flows are formed in a square duct which may drastically influence the particle dispersion. This work will examine the effect of secondary flows on particle transport. To the author's knowledge, no previous work on particle-laden square duct flow has been reported.

1.2 Outline of the Thesis

The following seven chapters describe the various aspects of this dissertation. Given the tragic circumstances surrounding the shift in research directions during this dissertation, the experimental data collected in the early stages of the research is being presented as a motivation for the computational studies by demonstrating an application where dispersed two-phase flow improves heat exchanger performance. This experimental phase-Doppler study on refrigerant flow is presented in Chapter 2 as a self-contained study. A literature review of the previous work in LES modeling, experimental and computational studies of wall bounded flows, and gas-particle flows, is presented in Chapter 3. The governing equations for LES and particle transport are given in Chapter 4, along with the numerical methods used to solve them. Chapter 5 presents the results of the preferential concentration simulations. Chapter 6 presents the results of the particle deposition simulations. A summary of this dissertation and recommendations for future work are given in Chapter 7.

Chapter 2. Motivation

In this chapter, an experimental study of dispersed two-phase refrigerant flow is presented. Droplet sizes, velocities, and their spatial distributions are reported. Also, a novel method for improving flow distribution in evaporators is reported. Since the focus of this thesis is computational, this chapter is arranged such that it is self-contained; all other portions of this thesis may be ignored by the reader interested in only the experimental aspect of this work. This section also serves as a motivation for the computations in future chapters, as this section demonstrates an application of dispersed two-phase flow in a square duct.

2.1 Background

The heating, ventilation, and air conditioning (HVAC) community has been plagued with the problem of maldistribution of two-phase refrigerant flow in headers of evaporators. The problem is complex as it involves such factors as orientation of the header, header shape, mass flow rate, quality, refrigerant properties, etc. Previous attempts to correct the problem have relied either on simplified models, placement of baffles, flow constrictions or other geometry-specific remedies (Cabuk and Modi 1989; Kim, Choi, and Cho 1995; Chisolm and Wanniarachchi 1992; Wang and Peizhen 1989). However, given the wide range of operating conditions for HVAC systems, particularly in automotive applications, these methods generally fail to produce uniform distribution for the entire range of operating conditions. Unequal distribution of the two-phase flow can lead to significant losses in the efficiency of heat exchangers.

Early modeling of flow distribution was performed by Bajura (1971) and Bajura and Jones (1976). They used simple integral momentum approaches to construct general models for flow distribution in manifolds. An one-dimensional finite difference model was developed by Datta and Majumdar (1982) for predicting two-phase flow distribution in parallel, reverse and mixed flow manifolds. A two-dimensional model was developed by de Moura (1990) based on the two-fluid concept. Only qualitative agreement with experimental measurements of flow distribution was achieved in the above studies. Jones and Galliera (1998) used standard and RNG k-e models in Fluent to benchmark their integral model for flow distribution. They achieved good agreement between the two approaches and note that the integral model approach has a tremendous advantage in terms of computational speed.

The pipeflow downstream of a generic header was examined with Laser Doppler Velocimetry by Yeh and Mattingly (1995). As in most studies involving header flow, they considered water as the working fluid instead of refrigerant. Their velocity data indicate that the header initially produces a highly swirled flow that varies with Reynolds number and roughness conditions. It should be noted that their results are only valid for one header shape. In an attempt to find an optimum header shape, Samson, Stark, and Grote (1988) developed a fan-header concept to evenly distribute an air/water mixture to within 16% of the ideal distribution.

A study on air/water distribution in an adiabatic plate heat exchanger was performed by Rong, Kawaji, and Burgers (1995). They found that the flow distribution was greatly affected by the inlet quality and mass flow rate. Vertical upward flow was found to be more uniformly distributed compared to vertical downward flow. Custom blockages were designed and installed which were shown to improve distribution.

The approach taken in this work is to use a pressure swirl atomizer to create a mist flow inside the header in which the droplets will follow the large-scale vapor motion, thereby uniformly feeding each branch in the header.

Refrigerant will be used rather than air/water since the density ratios of air/water and refrigerant vapor/liquid differ by an order of magnitude. Also, air/water will not capture the rapid evaporation, or "flashing", present after expansion. To the author's knowledge, no similar attempts have ever been previously made by the HVAC community towards reducing maldistribution. Also to the author's knowledge, there is limited, if any, refrigerant droplet size data available from atomizers. Therefore, this work serves two roles. First, to present an application where an aerosol-type flow can enhance heat exchanger equipment. This method of flow distribution is both simple and effective, making it ideal for implementation in existing evaporators. Second, this work will also help characterize the spray found in such a device. These data will be beneficial to designers who are concerned with the evaporation characteristics of such a mist-flow when a heat load is applied in an evaporator, as well as to help construct models for such sprays in evaporators.

2.2 Experimental Setup

The present test setup consists of a refrigeration loop, shown in Fig. 2.2.1, which includes the header and Delavan's WDB8-30 full-cone atomizer. This nozzle had a 30° spray angle and 0.81 mm exit orifice diameter and was used for all droplet measurements presented in this work. Single-phase R-134a liquid is injected via a pressure swirl atomizer, which also serves as the expansion device, into the header. The header is made of transparent walls of clear PVC to allow optical measurements. The header dimensions are 1"x1"x12" with five equally spaced 3/8" NPT exit ports along the bottom of the header. A single component Aerometrics Phase/Doppler Particle Analyzer (PDPA) identical to the one used in Drallmeier and Peters (1994) is used to measure the droplet size and axial (horizontal) velocity at various downstream positions along the centerline of the header. See Table 2.2.1 for the PDPA settings. Refrigerant flow rates of 1, 2 and 3 g/s were used. Higher flow rates were not considered because of film formation on the walls of the header which prevented the PDPA measurements.

Each of the five branches contained a separation cylinder. The liquid flow rates through each branch were determined by collecting the liquid in the cylinder for a given time. The vapor flow rate in each branch was determined by switching a three-way valve group to feed a test branch containing a vapor flow meter. This allowed the vapor flow rate in each branch to be determined one branch at a time. To ensure that both the test branch and the recycling branch had the same pressure drop for a given flow rate, valves were added to each branch and adjusted until the pressure drops were balanced for a given flow rate. The total flow rate, as determined from the sums of the liquid and vapor flow rates, was compared to the measurement from a mass flow meter placed before the nozzle and good agreement was found. This method of determining the distribution was found to be superior to interrogating the region above each exit port with the PDPA and integrating a mass flux over the port area to get a branch flow rate, which leads to a distribution if all ports are sampled. A significant error in this approach to find the distribution with the PDPA is that much of the liquid travels to the ports in films along the walls of the header, or in pools along the bottom of the header. This film flow rate is not measurable with the PDPA, therefore, the distribution given by the PDPA is far from the true distribution. For this reason, the collection cylinders and vapor flow meter were used to find distributions. The droplet size measurements taken with the PDPA are used to judge the homogeneity of the flow inside the header, not as a direct measure of the flow distribution in the exit ports. However, it is logical to assume that a homogeneous mist inside the header is beneficial to flow distribution. In addition, a real heat

exchanger will have a thermal load. The SMD data presented here provides valuable information regarding the evaporation characteristics of the droplets inside the header. The data may also be used in constructing or validating computational models of the refrigerant sprays.

The thermodynamic quality was varied from 0% to 15% in this work. The quality was controlled by adjusting the liquid temperature with a heater before the nozzle. An isenthalpic process was assumed across the nozzle. By knowing the pressure and temperature of the subcooled liquid before the nozzle, and the pressure in the header after the nozzle, the quality in the header can be calculated with any standard thermodynamic refrigerant table or software. The header was assumed to be adiabatic. A needle valve placed upstream from the nozzle is used for fine adjustment of the mass flow rate. This method of determining the quality was compared to the value obtained from the sums of the total flow rates of liquid and vapor through all exit branches and excellent agreement was found.

The range of operating conditions is shown in Table 2.2.2, along with the uncertainties in the measurements. The pressure uncertainty is 0.17% of the full-scale reading. The thermocouples were calibrated in an ice bath, and the uncertainty listed is an average fluctuation about the mean which was determined by examining the time signal data. The uncertainty listed for the phase-Doppler size measurement is based on monodisperse droplet flows, comparison to other techniques, and data repeatability (given in the Aerometrics manual). The velocity uncertainty is based on standard laser Doppler velocimeter measurements.

2.3 Experimental Results

For a given condition, the droplet Sauter mean diameter (SMD) was measured along the centerline of the header. The centerline SMD is used as a representative size of the droplets for the given condition. Measurements along a vertical cross section proved to be unreliable as the PDPA validation rate quickly dropped as the probe volume was moved near the walls due to liquid pools and films on the walls. Typical validation rates along the centerline ranged from roughly 80% to 90%, while validation rates near walls were less than 50% and therefore not used. To ensure correct statistics, typically 10,000 drops were sampled at each location, with no less than 5,000 drops sampled in more challenging measurement conditions. Mass flow rates of 1, 2 and 3 g/s are shown along with qualities from 0% to 15%. However, for the 1 g/s case, shown in Fig. 2.3.1, only 7% quality was obtainable since insufficient pressure drop was created by the nozzle. There are two important trends worth noting. First, the droplet SMD is found to decrease with increasing thermodynamic quality in the header. This is partly due to the refrigerant undergoing a rapid, violent evaporation (called “flashing”) when the liquid is sprayed into a cavity which is below its saturation pressure, as is the case here. The second trend is the decrease in centerline SMD with increasing distance downstream of the nozzle. Due to gravity, the bigger droplets will settle out of the core of the spray and drain into the exit ports, thus leaving only the smaller drops downstream on the centerline. It is important to note that for 0% quality, the centerline SMD appears to increase with increasing distance downstream of the nozzle. This seemingly opposite trend is because that although the probe volume is along the centerline of the header, low momentum jets, such as this 0% quality 1 g/s case, are quickly influenced by gravity and slope downward causing the edge of the jet to be measured as the probe volume is traversed downstream. Drallmeier et al. (1994) have shown that these types of atomizers concentrate the largest droplets at the outer edge of the jet. It is these larger

droplets at the outer edge of the jet that are being measured for this 0% quality case which is why the SMD appears to increase along the centerline for this case. Typical velocities measured inside the header were on the order of 1 m/s, confirming that larger droplets can indeed deviate from their initial trajectories causing this seemingly peculiar trend.

The same nozzle is used in Figs. 2.3.2 and 2.3.3, but the flow rate has been increased to 2 and 3 g/s, respectively. The same trends hold as before, however, additional features begin to become apparent. Notice that for saturated liquid (0% quality) the average SMD along the centerline is decreasing with increasing flow rate. The opposite holds true for nonzero quality. For the qualities tested that were greater than zero, the average centerline SMD was found to increase with increasing flow rate.

The axial variation of the droplet number density along the centerline is shown in Fig. 2.3.4 for 2 g/s and 10% quality. It can be seen that the number density increases for distances up to roughly 90 mm from the inlet, then drops off as the distance downstream of the nozzle increases. There are several factors causing this trend. The number density measurements are dominated by the behavior of the small droplets. Near the nozzle, two factors can be attributed to the increasing droplet number density. First, vapor entrainment can cause smaller droplets to be drawn into the center of the spray thereby increasing the measured number density. Second, due to gravity, the spray sheath (where number densities are typically higher) could be drawn into the probe volume as an axial traverse is being made. Far from the nozzle, all droplets are being lost to the walls of the header and to the exit branches as the spray expands – thus explaining the decrease in number density far from the inlet.

To more clearly display the trends of the droplet size along the centerline of the header, several histograms showing the droplet and velocity distributions at various downstream locations are shown. This will help show the nature of the droplets present in the spray as well as verify that no truncation of the diameter distribution occurred through the PDPA processing. The case shown in Figs. 2.3.5-2.3.8 is 2 g/s and 10% quality, which is close to the middle of the entire test matrix. Four downstream positions are shown in Figs. 2.3.5-2.3.8, at 60, 80, 100 and 120 mm downstream, respectively. Since the intensity of the scattered light is proportional to the drop's cross section, smaller drops will only scatter enough detectable light when they pass through the center of the measurement volume where the laser beam intensity is highest. This makes the effective measurement volume for small drops less than the measurement volume for larger drops. The PDPA software corrects for this bias and generates a corrected count. The size histograms shown represent the corrected count. The droplet size ranges are seen to become more tightly grouped as the distance downstream increases. This confirms the earlier statement that the larger droplets settle out of the core of the spray far from the nozzle. The trend of decreasing droplet size with increasing distance downstream can also be seen.

Horizontal axial velocity distributions are shown to illustrate typical droplet velocities encountered in the header. The velocities measured were on the order of 1 m/s, with a decrease in velocity downstream of the nozzle as the jet spreads. It was not possible to obtain measurements near the nozzle exit as the spray was found to be too dense to obtain reliable phase-Doppler measurements. The velocity vs size scatter plots indicate that the average velocity at a point is not a strong function of the droplet size.

To illustrate the effectiveness of the atomizer approach in reducing maldistribution, a typical case is presented to compare the distribution trends between the atomizer approach and the conventional method of using an expansion valve and 3/8" pipe inlet. The case shown is 15 g/s and 10% quality, which represents a higher flow rate than the PDPA results shown. This is because the flow rates illustrated in the PDPA data were optically thin enough to allow the PDPA measurements, but these flow rates are lower than what are typically encountered in industry. Since industrial applications will be the target of the maldistribution reduction via the atomizer approach, the distribution results should reflect industrial operation conditions. However, as mentioned earlier, these higher flow rates did not permit phase-Doppler measurements. For this reason, the PDPA is used to illustrate the spray dynamics at lower flow rates, while the distribution results are measured at higher, more realistic flow rates. Figures 2.3.9 and 2.3.10 display the liquid distribution results for the pipe inlet and atomizer inlet, respectively. It is clear that in the pipe inlet case, the first branch receives roughly half of the total liquid flow, while the last two branches receive little or no liquid which would lead to dry-out in these tubes and significantly reduce the heat exchanger performance. When the atomizer is used for the same condition, it can be seen in Fig. 2.3.10 that all exit ports receive liquid and the distribution is more uniform than the pipe inlet case. For evaporators, liquid distribution is the main focus of concern, much more so than vapor distribution. It was found that for the flow rates tested, the vapor distribution was highly uniform and not altered significantly by the choice of inlet to the evaporator, and is therefore not shown.

2.4 Experimental Conclusions

A novel method for improving the flow distribution in headers of evaporators has been presented which involves using an atomizer as the expansion device which creates a mist-type flow to more uniformly distribute the refrigerant among the exit ports. Phase-Doppler Particle Analyzer measurements were taken along the centerline of the header for various conditions to determine typical size droplets generated with these types of nozzles. The main trends indicate that the SMD increases with increasing flow rate for nonzero qualities and the SMD decreases downstream of the nozzle. Distribution results indicate that the atomizer approach does indeed provide a more uniform distribution to the exit ports.

Chapter 3. Literature Review

In this chapter, previous work on LES models, square duct flows, other wall-bounded flows, and gas-particle flows is presented. The discussion is limited to incompressible flows. In Section 3.1, the vast array of LES models is reviewed. In Section 3.2, the focus is on square duct flow. In Section 3.3, other wall-bounded flows are reviewed, with an emphasis on computational works. In Section 3.4, gas-particle flows (experimental and computational) are reviewed.

3.1 Large Eddy Simulation Models

LES models have evolved over the last few decades to include a wide range of methodologies. This section will discuss the key features in the vast array of today's LES modeling efforts. The Smagorinsky model has been the most widely used of all LES models. It is simple to program and consumes little additional CPU time, which is perhaps why it remains popular even today. However, several researchers have pointed out fundamental problems with the Smagorinsky model which has led to the development of many other models, such as the dynamic Smagorinsky model, scale similarity model, mixed model, and a class of SGS kinetic energy models. Each of these models will be discussed in this section. It is not possible to discuss all aspects of LES, for example, the ideal LES formulation as given in Langford (2000) and Volker (2000). This thesis will focus on methods that do not require DNS data *a priori*.

Without question, the Smagorinsky model has been the most widely used model in LES. This model assumes the following form for the eddy viscosity:

$$n_T = l^2\sqrt{2S_{ij}S_{ij}} \tag{3.1.1}$$

where l is a length scale commonly chosen to be that suggested by Piomelli, Ferziger, and Moin (1987) and is given by:

$$l = C_S\left\{1-\exp\left[-\left(y^+/A^+\right)^3\right]\right\}^{1/2}\left(\Delta_x\Delta_y\Delta_z\right)^{1/3} \tag{3.1.2}$$

where C_S is Smagorinsky's constant, A^+ is a constant commonly chosen to be 26, y^+ is the nondimensional distance from the wall ($y^+ = yu_t/\nu$) and Δ_x, Δ_y, and Δ_z are filter widths in the x, y and z directions, respectively, and u_τ is the friction velocity. S_{ij} is the strain-rate tensor. In this case, the exponential decaying function in (3.1.2) is known as a wall function, which effectively reduces the eddy viscosity near a wall. In isotropic turbulence, the damping factor is removed from (3.1.2). One drawback of the Smagorinsky model, and most SGS models in general, is that no information about the unresolved scales is gained. By developing a transport equation for the SGS kinetic energy, one can estimate how much energy is in the unresolved scales as well as use this energy to construct a model for the eddy viscosity. This will be discussed later.

Some of the early subgrid-scale comparisons were done by Clark, Ferziger, and Reynolds (1979). This work was among the first to acknowledge the deficiency of eddy viscosity models. Decaying isotropic grid turbulence was simulated using fourth-order finite difference schemes in space and a third-order predictor-corrector method in time on a 64^3 grid. Four models were considered, all of the eddy viscosity type: the traditional

Smagorinsky model, a vorticity model, a kinetic energy model, and a model which assumes constant eddy viscosity. Their conclusion was that no eddy viscosity model can do much better than the Smagorinsky model. However, they note that these results may not apply to complex flows, such as wall-bounded flows.

The limitations of the Smagorinsky model are more clearly identified in Piomelli et al. (1991). The concept of backscatter is used to justify their conclusion. In turbulence, energy may be transferred from the large scales to the small scales, where it is dissipated. However, it is also possible for the small scales to supply energy to the large scales, which is the so-called backscatter. They argue that since the Smagorinsky model is purely dissipative, it cannot capture the physical effects of backscatter. By filtering DNS data on turbulent channel flow, several filters (Gaussian, box, and cutoff filters) were examined and it was found that roughly 50% of all points experience backscatter, regardless of the filter used. Therefore, they conclude that any accurate SGS model would incorporate backscatter effects.

In an attempt to correct the inherent shortcomings of the Smagorinsky model, Germano et al. (1991) developed a dynamic eddy viscosity model. This model allows backscatter, as well as predicts the correct near-wall behavior. The model takes advantage of a mathematical identity which can be expressed as follows. Consider expressing the resolved turbulent stress in the following manner:

$$L_{ij} = \overline{\overline{u}_i \overline{u}_j} - \overline{u}_i \overline{u}_j = T_{ij} - t_{ij} \tag{3.1.3}$$

where the SGS stress at the grid level is denoted t_{ij} while the SGS stress at a second test filter, larger than the grid filter, is denoted T_{ij}. Now if M_{ij} and m_{ij} are models for the anisotropic parts of T_{ij} and t_{ij} then the eddy viscosity model may be expressed as:

$$t_{ij} - \frac{1}{3} t_{kk} \approx m_{ij} = -2C\overline{\Delta}^2 \left|\overline{S}\right| \overline{S}_{ij} \tag{3.1.4}$$

$$T_{ij} - \frac{1}{3} T_{kk} \approx M_{ij} = -2\tilde{\overline{\Delta}}^2 \left|\tilde{\overline{S}}\right| \tilde{\overline{S}}_{ij} \tag{3.1.5}$$

where

$$\tilde{\overline{S}}_{ij} = \frac{1}{2}\left(\frac{\partial \tilde{\overline{u}}_i}{\partial x_j} + \frac{\partial \tilde{\overline{u}}_j}{\partial x_i} \right), \quad \left|\tilde{\overline{S}}\right| = \sqrt{2 \tilde{\overline{S}}_{mn} \tilde{\overline{S}}_{mn}} \tag{3.1.6}$$

The tilde represents the test filter case. Substituting (3.1.4) and (3.1.5) into (3.1.3) gives the following:

$$L_{ij} \overline{S}_{ij} = -2C\left(\tilde{\overline{\Delta}}^2 \left|\tilde{\overline{S}}\right| \tilde{\overline{S}}_{ij} \overline{S}_{ij} - \overline{\Delta}^2 \left|\tilde{\overline{S}}\right| \tilde{\overline{S}}_{ij} \overline{S}_{ij} \right) \tag{3.1.7}$$

At this point, C=C(x,y,z,t) and can be obtained from the previous equations. However, to prevent C from becoming indeterminate, it can be assumed that C = C(y,t) for periodic channel flow, which is studied in Germano et al. (1991), with y being the wall normal direction. Therefore, it is necessary to average over planes parallel to the walls. This gives the following:

$$C(y,t) = -\frac{1}{2}\frac{\left\langle \mathsf{L}_{ki}\overline{S}_{ki}\right\rangle}{\tilde{\overline{\Delta}}^2\left\langle \left|\tilde{\overline{S}}\right|\tilde{\overline{S}}_{mn}\overline{S}_{mn}\right\rangle - \overline{\Delta}^2\left\langle \left|\tilde{\overline{S}}\right|\tilde{\overline{S}}_{pq}\overline{S}_{pq}\right\rangle} \tag{3.1.8}$$

The dynamic eddy viscosity, or the so-called dynamic Smagorinsky, model is then given by:

$$m_{ij} = \frac{\left\langle \mathsf{L}_{ki}\overline{S}_{ki}\right\rangle}{\left(\tilde{\overline{\Delta}}/\overline{\Delta}\right)^2\left\langle \left|\tilde{\overline{S}}\right|\tilde{\overline{S}}_{mn}\overline{S}_{mn}\right\rangle - \left\langle \left|\tilde{\overline{S}}\right|\tilde{\overline{S}}_{pq}\overline{S}_{pq}\right\rangle}\left|\overline{S}\right|\overline{S}_{ij} \tag{3.1.9}$$

This summarizes the dynamic Smagorinsky model, which has been the most widely used dynamic model in recent work. Moin (1998) points out that the reason this model is so widely used is that it vanishes in regions of smooth, or laminar, flow as well as has correct behavior near the wall and states that this model is perhaps the only model to be applied successfully to such a wide range of applications. However, there is a potential shortcoming of this model. Consider the averaging done by Germano et al. (1991). In many flows, there is no homogeneous direction to average over. In this case, the above approach fails unless a different averaging approach is taken. Meneveau, Lund, and Cabot (1996) have developed a Lagrangian time averaging procedure which does not require a homogeneous direction. A new variable is then introduced, the Lagrangian time scale over which averaging takes place. The time scale is chosen such that the model becomes purely dissipative, which guarantees numerical stability. Their results indicate a 10% increase in CPU time compared with the spatially averaged method. By averaging backwards in time over particle trajectories, they achieve as good or better results in isotropic turbulence and fully developed channel flow when compared to the spatially averaged method. For a more statistical look at the dynamic Smagorinsky model, see Germano (1996).

In order to circumvent the shortcomings of Germano's original dynamic model which required a homogeneous direction, Ghosal et al. (1995) have presented a dynamic localization model based on Germano's original work. In flows with no homogeneous direction, an integral equation for C is developed based on a constraint that C must remain positive. In order to allow backscatter of energy, a SGS kinetic energy model is incorporated into their procedure. In this case, C is allowed to have either positive or negative values and the eddy viscosity is based on the SGS kinetic energy, k. Realizability conditions are discussed for their model and they apply their model to isotropic turbulence and a backward facing step. Good agreement is obtained for both cases.

Liu, Meneveau, and Katz (1995) have measured the far-field of a jet using 2-D PIV and then performed *a priori* tests of several subgrid models. They confirmed the poor correlation between the real stresses and those given by the Smagorinsky model. By using a mixed model, they achieved better correlation. Their reasoning behind the success of the mixed model is that the fluctuations of the eddy viscosity term are small compared to the similarity term plus the eddy viscosity term dissipates energy since it is well correlated with the strain-rate tensor, something the similarity term does not handle well.

A comprehensive summary of LES models may be found in Lesieur and Metais (1996). The Smagorinsky model is stated to be too dissipative in the near wall region to allow the growth of viscous instabilities. The dynamic model is reviewed along with a class of spectral models, such as Kraichanan's spectral eddy viscosity model. In

physical space, the structure-function model is stated to be the mimic of a spectral model. A 3-D variation of the structure-function model is discussed where the eddy viscosity is weighted such that it is only significant in regions of space where the flow contains elements of three dimensionality. Bardina's scale-similarity model is reviewed along with the mixed model. A class of quasi-DNS, or no model LES, approaches where the numerical dissipation arising from upwinding are discussed.

A review of six LES models may be found in Vreman, Geurts, and Kuerten (1997). The weakly compressible temporal mixing layer is used as the test case, and the six models considered are: Smagorinsky, similarity, gradient, dynamic Smagorinsky, dynamic mixed, and dynamic Clark model. An *a priori* test is done with filtered DNS data and the following parameters are evaluated: the evolution of the total kinetic energy, backscatter, turbulent and molecular dissipation, and the Fourier energy spectra. Their no-model LES is shown to give better predictions of the total kinetic energy than the Smagorinsky model, with the dynamic mixed model giving the closest results to the filtered DNS kinetic energy data. The Smagorinsky and its dynamic version are shown to not produce any backscatter, and the gradient model artificially removes any backscatter with a limiter concept. None of the models reproduce the filtered DNS levels of backscatter. Some *a posteriori* testing is also done in this paper. In all tests, the Smagorinsky model was given a "bad" rating, with their scale consisting of bad, reasonable, good, and very good. As expected, the dynamic models they considered scored the highest ratings.

An excellent review of the work in scale-invariance modeling may be found in Meneveau and Katz (2000). A detailed look at *a priori* and *a posteriori* studies is provided along with various methods of separating the large scales from the small scales with techniques such as orthonormal basis functions. The Smagorinsky model along with its limitations are discussed in detail. The dynamic Smagorinsky model is reviewed favorably. Bardina's similarity model is discussed, along with its mixed model variation. Other less traditional models such as kinetic energy models and gradient models are also briefly reviewed. Testing of LES models based on comparison between real and modeled stresses is considered by reviewing the work on optimal LES approaches.

While still an eddy viscosity model, Schumann (1975) employs the use of the SGS kinetic energy, k_{sgs}, to find the eddy viscosity rather than relying on a Smagorinsky approach. He considers channels and annuli, but the key feature in this paper is his kinetic energy model. The eddy viscosity is split into two parts, the locally isotropic and inhomogeneous parts. A transport equation is developed for the SGS kinetic energy, k, which includes convection, production, dissipation, viscous gross scale dissipation and diffusion. One unique approach is that the strain-rate tensor in the production term is based on the fluctuating velocities rather than the total velocities. This ensures zero production in the case of laminar flow. Some empiricism is required in order to set the constants in his model, and satisfactory agreement was obtained using the new SGS model.

Schmidt and Schumann (1989) continue the work of Schumann's model by investigating the convective boundary layer. No effort is made to split the SGS stresses as Schumann had originally done. Instead, a single refined transport equation for the SGS kinetic energy is developed which includes buoyancy. To ensure non-negative values of k, the second-order upwind scheme MPDATA of Smolarkiewicz is used. Much emphasis is placed on their second-order closure model for their kinetic energy equation. Fair agreement is obtained when comparing with experimental atmospheric data.

The issue of subgrid length scales has been addressed by Schumann (1991). Three length scales are considered. The first is the simplest with the length scale, l, equal to the minimum of the local grid width or the product of a constant and the distance from the surface. Second, he considers a Deardorff-type model which is the same as the first except now l is the minimum of the first model or a buoyancy length scale. Lastly, he considers a stability limited vertical scalar diffusion model. He finds that the results for scalar dispersion are only weakly sensitive to the length scale chosen. Schumann then accepts the first-order closure model for his SGS kinetic energy equation instead of his second-order model in the previous work. He cites realizability problems which are absent from the first-order model as the reason for its choice and produces results which show little quantitative difference between the two models. When examining the maximum scalar concentration on a coarse grid, an 18% difference is found between the different length scale choices.

In the class of SGS kinetic energy models, one of the simplest to understand is that of Yoshizawa (1982). Using a statistical viewpoint, he derives a subgrid model that states the total derivative of the SGS kinetic energy is equal to production minus dissipation. Or, in mathematical terms:

$$\frac{Dk_{sgs}}{Dt} = \nu_T \left|\overline{S}\right|^2 - 1.9\frac{k_{sgs}^{3/2}}{\Delta}, \quad \nu_T = 0.066\Delta k_{sgs}^{1/2} \tag{3.1.10}$$

where Δ is the local grid scale. He assumes that the triple velocity correlation and the pressure-velocity correlation vanish to the first order. He also states that production and dissipation dominate in channel and pipe flows. No simulations are carried out in this paper.

It is only natural that a dynamic version of the SGS kinetic energy model would be developed. Kim and Menon (1995) propose the dynamic SGS kinetic energy model and compare it to DNS, Germano's dynamic model, and a previous dynamic k-equation model. They consider averaging their dynamic model in a local cube, but argue that this is not what a true dynamic model should entail. Instead of averaging just for the sake of numerical stability, they propose a dynamic method which requires no averaging. A method similar to the way Germano set up his two filter system is formulated and calculations are performed for Taylor-Green vortex flow. A non-staggered grid with second-order time accuracy and fifth-order (convective terms) and sixth-order (viscous terms) spatial accuracy is used. Agreement with DNS is found to be better than the other models tested, even the celebrated dynamic Smagorinsky model. In addition, lower computational costs are experienced when compared to the previous dynamic k-equation model. By performing the simulations on two different grids, they confirm that the grid resolution was not the deciding factor. The quantities they considered include the flatness factor, the time evolution of the model coefficients for the various models, skewness factor, and production and dissipation rates of the SGS kinetic energy.

In another effort to evaluate the various subgrid models, Menon, Yeung, and Kim (1996) conduct a comparison of many models, including the scale similarity, Smagorinsky, kinetic energy, dynamic kinetic energy, and dynamic eddy viscosity model. They use *a priori* tests to determine the local subgrid stresses and energy transfer in isotropic turbulence. They find that the scale similarity model loses correlation with a decrease in the grid resolution when compared to the behavior of the kinetic energy model. With an increase in Reynolds number,

the dynamic k-equation model performed better than the dynamic Smagorinsky model. The dynamic models also performed well even on coarse grids, and much better than the fixed coefficient models.

The dynamic subgrid kinetic energy, given in detail in Kim and Menon (1997), can be summarized as follows. The transport equation for the subgrid kinetic energy, k_{sgs}, is given as

$$\frac{\partial k_{sgs}}{\partial t} + \bar{u}_i \frac{\partial k_{sgs}}{\partial x_i} = ?_T \left|\bar{\mathbf{S}}\right|^2 - e + \frac{\partial}{\partial x_i}\left(?_T \frac{\partial k_{sgs}}{\partial x_i} \right) \tag{3.1.11}$$

where the eddy viscosity, ν_T, is given by

$$?_T = C_\tau \bar{?} k_{sgs}^{1/2} \tag{3.1.12}$$

and the dissipation rate, ε, is given by

$$e = C_\varepsilon \frac{k_{sgs}^{3/2}}{\bar{?}} \tag{3.1.13}$$

where $\bar{\Delta}$ is the grid scale and C_ε and C_τ are dynamically determined. The resolved strain-rate tensor, $\bar{\mathbf{S}}$, is expressed as

$$\bar{S}_{ij} = \frac{1}{2}\left(\frac{\partial \bar{u}_i}{\partial x_j} + \frac{\partial \bar{u}_j}{\partial x_i} \right) \tag{3.1.14}$$

and its magnitude is defined as

$$\left|\bar{\mathbf{S}}\right| = \sqrt{2\bar{S}_{ij}\bar{S}_{ij}} \tag{3.1.15}$$

Let the "hat" notation symbolize the application of the test filter to a quantity and the "overbar" notation symbolize application of the grid filter. The Leonard stress tensor is then defined as

$$L_{ij} = \widehat{\bar{u}_i \bar{u}_j} - \hat{\bar{u}}_i \hat{\bar{u}}_j \tag{3.1.16}$$

The kinetic energy at the test filter level can be found from the trace of (3.1.16)

$$k_{test} = \frac{1}{2}\left(\widehat{\bar{u}_k \bar{u}_k} - \hat{\bar{u}}_k \hat{\bar{u}}_k \right) \tag{3.1.17}$$

The dissipation at the test filter level is expressed as

$$e_{test} = \left(? + ?_T\right)\left(\frac{\partial \bar{u}_i}{\partial x_j}\frac{\partial \bar{u}_i}{\partial x_j} - \frac{\partial \hat{\bar{u}}_i}{\partial x_j}\frac{\partial \hat{\bar{u}}_i}{\partial x_j} \right) \tag{3.1.18}$$

Through a similarity assumption between the subgrid stress tensor and the Leonard stress tensor, one can arrive at the following equation

$$L_{ij} = -2C_t \hat{?} k_{test}^{1/2} \hat{\bar{S}}_{ij} + \frac{1}{3} d_{ij} L_{kk} \tag{3.1.19}$$

The least-square method of Lilly (1992) is then used to obtain a formula for C_τ

$$C_\tau = \frac{1}{2}\frac{L_{ij}s_{ij}}{s_{ij}s_{ij}} \tag{3.1.20}$$

where

$$s_{ij} = -\hat{?}\,k_{test}^{1/2}\hat{\bar{S}}_{ij} \tag{3.1.21}$$

By invoking a similarity assumption between the dissipation at the test filter and grid filter level, an equation for the dissipation at the test filter level is given as

$$e_{test} = C_\varepsilon \frac{k_{test}^{3/2}}{\hat{?}} \tag{3.1.22}$$

One may now calculate C_τ and C_ε. This model was used in the bulk of this dissertation. These constants have been constrained to be positive in this dissertation.

There are two aspects of LES which remain in debate. They are the choice of the filter and the choice of the subgrid model. The various filters will now be discussed. There are several filters available for LES, such as the spectral cutt-off filter, Gaussian filters, and top-hat filters. There is implicit filtering in any finite difference/finite volume formulation since length scales smaller than the grid width cannot be resolved. This is known as box or top-hat filtering in finite-difference formulations, and sharp cut-off filters in spectral representations. Some researchers state that the filtering length scale should not be dependent on the grid resolution, therefore, they suggest applying an explicit filter (called "prefiltering") such as the Gaussian filter. The argument against that is prefiltering removes information that has already been resolved and therefore is computationally expensive. The three filters just discussed have the following representations in physical and spectral space:

Gaussian filter:

$$G_i(x_i - x'_i) = \left(\frac{6}{p?_i}\right)^{1/2} \exp\left(\frac{-6(x_i - x'_i)^2}{?_i^2}\right), \quad G_i(k_i) = \exp\left(\frac{-k_i^2?_i^2}{24}\right) \tag{3.1.23}$$

Spectral sharp cut-off filter:

$$G_i(x_i - x'_i) = \frac{2\sin\left[p(x_i - x'_i)/?_i\right]}{p(x_i - x'_i)}, \quad G_i(k_i) = \begin{matrix} 1 & |k_i| \le p/?_i \\ 0 & \text{otherwise} \end{matrix} \tag{3.1.24}$$

Top-hat filter:

$$G_i(x_i - x'_i) = \begin{matrix} \frac{1}{?_i} & |x_i - x'_i| < ?_i/2 \\ 0 & \text{otherwise} \end{matrix}, \quad G_i(k_i) = \frac{\sin(k_i?_i/2)}{k_i?_i/2} \tag{3.1.25}$$

Due to its simplicity and robustness, top-hat filtering remains popular for finite-volume simulations. It is typically implemented through implicit grid filtering.

3.2 Square Duct Flow

There are a number of previous studies on turbulent flow in geometries such as isotropic turbulence, channels and pipes (Yeung and Pope 1989; Kim, Moin, and Moser 1987; Eggels et al. 1994). However, only a few studies on internal flows with only one homogeneous direction have been conducted. Perhaps the first observation of mean secondary flows in a rectangular duct were made by Nikuradse (1930). He observed that mean streamwise contours bulged towards the corners, a feature not seen in circular ducts or laminar flow in rectangular ducts. The secondary velocities are usually only 1-3% of the streamwise bulk velocity in magnitude, but can significantly alter such things as heat and mass transfer near the walls. Prandtl (1952) termed these flows as secondary flows of the second type (the first type arises due to streamwise curvature). Turbulent fluctuation were suspected as the cause of these flows. He argued that velocity fluctuations tangential to streamwise velocity contours in regions of contour curvature cause a transverse mean flow to arise which is directed towards the corners.

Brundrett and Baines (1964) experimentally measured the velocity field and Reynolds stresses in a square duct. They found that the streamwise vorticity in fully-developed flow is primarily produced by the gradients in the normal Reynolds stresses. Since the streamwise vorticity is strongly correlated to the secondary flows, they suggest that the secondary flows are caused by the gradients in the Reynolds stresses. In the range of Reynolds numbers that they examined (Re = 20000 to 83000), no qualitative difference was observed in the secondary flows other than secondary flows tend to penetrate deeper into the corners with an increase in the Reynolds number.

Demuren and Rodi (1984) performed calculations of flow in straight, non-circular ducts and reviewed the various algebraic stress models. They developed algebraic expressions for the Reynolds stresses by simplifying earlier models and retaining the gradients of the secondary velocities. Mean flow and turbulence quantities were found to be predicted well, but the secondary velocities were found to be under-predicted. Bradshaw (1987) points out that the main challenge is the behavior of the pressure-strain term in the Reynolds-stress transport equations. He suggests that if models based on these equations fail to reproduce the decline in shear-stress magnitude in boundary layers with cross-flow, then it will be unlikely that any future similar model will do any better. Kajishima and Miyake (1992) discuss the eddy viscosity models for a square duct. They state that the secondary flows are produced as a result of the imbalance between the gradient of the turbulence stress and the corresponding pressure in near-corner regions. This mandates careful treatment of the near wall region.

One of the first LES studies of secondary flows in a square duct was performed by Madabhushi and Vanka (1991). Using LES with a mixed spectral-finite difference code and the Smagorinsky model, they studied flow at Reynolds number 360 based on friction velocity and duct width. Since it is necessary to correctly predict the near wall behavior, a 65x65x32 grid was used in the x, y and z directions, respectively, with stretching in the x and y directions (the two wall directions). An interesting feature they found in the secondary flows is that the instantaneous secondary velocities can be as high as ten times the averaged values, which necessitated the use of a smaller time step than that predicted by using the mean velocities. The secondary flows were found to convect mean flow momentum from the center of the duct to the corners. This caused a bulging of the streamwise velocity contours towards the corners. They attribute the lack of symmetry in their cross section contour plots to an insufficient averaging time. Due to the large fluctuations previously mentioned, the 16 time units used to average the equations in their simulations was not enough, although the asymmetry is not so overwhelming that the results

are invalid. Comparisons with experiments are made, although the experimental data is at much higher Reynolds numbers (60,000 to 250,000 compared to the LES of 5810 based on centerline velocity). Therefore, only qualitative comparisons are made since the Reynolds number effects are not known for this flow. Symmetry is found about each corner bisector, which is expected. By examining the LES and experimental data, it is seen that the secondary flows penetrate deeper into the corner region with an increase in Reynolds number. Turbulence statistics are measured and the turbulent kinetic energy is found to decrease with increasing Reynolds number. Much like turbulent channel flow, streaky wall structures were found in the square duct. The various terms of the vorticity equation are compared and the production due to the gradient of the difference in the normal Reynolds stresses and the production due to the gradient in the secondary Reynolds shear stress are found to dominate when compared to convection and diffusion. For further reading, see Madabhushi (1993) and Madabhushi and Vanka (1993).

Gavrilakis (1992) performed a DNS of turbulent flow in a square duct at Re = 4400, based on bulk velocity and hydraulic diameter. His simulation involved 16.1 million grid points using finite difference methods. Turbulence statistics at the wall bisectors are compared to plane channel data and good agreement is found despite the presence of secondary flows in the square duct. After averaging the mean secondary flows about the octants, an additional flow cell is found between the corner cell and the wall bisector. This additional flow cell is relatively weak and not reported in experimental data. The wall shear stress is influenced by the secondary flows. The wall shear stress has a maximum at each wall mid-point as well as near the main secondary flow cells in the corners. Viscous diffusion of the vorticity was found to have a more significant role than secondary convection.

Huser and Biringen (1993) performed a DNS of turbulent flow in a square duct at Re = 600, based on mean friction velocity and duct width. Turbulence statistics along the wall bisector are compared with simpler flows and found to have excellent agreement. Terms in the Reynolds averaged streamwise vorticity equation display the mechanism that produces secondary flows via the secondary Reynolds stresses. Convection of streamwise velocity causes distorted isotachs that can only be caused by secondary flows. Strong turbulence production was found near the wall bisector, with weak production at the corner bisector. This produces positive and negative convection of the mean streamwise velocity at the respective locations, as they demonstrated by examining the terms in the Reynolds averaged streamwise velocity equation. Dominant ejection structures are produced during a bursting event and are composed of two streamwise counter-rotating vortices. Corners have reduced mean shear and prohibit ejections from occurring here, which allows a mean secondary flow from the core of the duct to the corner.

Recently, Xu and Pollard (2001) performed simulations of turbulent flow in a square duct and a square annular duct. Using the Smagorinsky model with wall functions, they examined flow at Re = 200 based on the half hydraulic diameter and average friction velocity. They note that even for a square duct, previous DNS studies do not agree for the mean streamwise velocity profile. They explain the mechanisms responsible for the generation of the secondary flows by examining the anisotropy of the Reynolds stress distributions. They develop a universal relation between the average streamwise velocity and the distance away from a concave corner along the corner bisector by using curve fitting techniques. Secondary flows in the annular duct are shown to consist of a chain of counter-rotating vortex pairs around both the convex and concave corners in the annular square duct.

3.3 Non-Square Duct Wall Bounded Single Phase Flows

Many researchers have examined wall bounded flows in geometries other than square ducts: a comprehensive review is beyond the scope of this thesis. This section will focus on the major studies in recent years, with an emphasis on computations.

Laser-Doppler Velocimetry measurements of the velocity distribution and reattachment length behind a backward facing step were performed by Armaly et al. (1983). Results are reported for a range of Reynolds numbers of $70 < Re < 8000$, which covers the laminar, transitional, and turbulent regimes. Numerically, 2-D finite difference simulations were also performed with 45x45 nodes and are in close agreement with experiments up to a Reynolds number of 400. Above Re = 400, they state the three-dimensionality of the experiment prevented the 2-D equations from accurately predicting the flow. They report an additional recirculation region on the wall opposite the step, which they claim has not been presented before.

A 3-D corner step experiment was the subject of work done by Stokes, Glauser, and Gatski (1998). This is one of the logical next steps when considering a more complex flow than a traditional backward step which has been studied extensively. 3-D LDV is used to measure the mean flow velocities as well as the Reynolds normal and shear stresses and turbulent kinetic energy. Secondary flows are observed within two stepheights of the streamwise step edge. A database of the first and second order statistics is formed for further comparison with turbulence modeling by other future researchers.

Turbulent channel flow has been a topic of much research. Tafti and Vanka (1990) have done a detailed LES of channel flow at a Reynolds number of 180 based on channel half-height and friction velocity. Using a finite volume approach and staggered grid, they employed the Smagorinsky model to calculate the eddy viscosity. A comparison with DNS data shows good agreement, with 5% error in the calculated friction factor with their coarse grid (32x64x32 cells). Their fine grid (66x66x66 cells, with stretching) showed worse agreement in the means, but better agreement in turbulent statistics. They suggest that perhaps the stretching in the wall direction decreased the accuracy of the calculation and state a uniform 66x66 cross section would have worked better. Also, the use of an iterative multigrid approach in solving the pressure Poisson equations gave a significant speed up in the execution time.

In another study of channel flow, Blackburn (1998) performed LES with the Smagorinsky model in conjunction with a van Driest-type wall damping function suggested by Piomelli. This wall damping function essentially removes the Smagorinsky model near the wall. With nearly 0.25 million nodes, the simulation met the grid spacing requirements suggested by Piomelli for resolving the near-wall layer. A friction Reynolds number of 651 is used for LES and compared with experimental results at a friction Reynolds number of 640. Satisfactory agreement in the buffer layer is obtained, however, poor agreement near the wall is attributed to experimental error. Two other simulations are conducted as well, a no-model LES on the same grid and the Smagorinsky model without a wall damping function. The no-model approach gives correct near-wall behavior, but poor results in the outer region. Without a damping function, the Smagorinsky model gives poor results in the mean flow throughout the domain. When comparing the fluctuating velocities, they find that their LES with a wall function over predicts the streamwise rms velocity by roughly 20%.

A highly resolved channel flow DNS calculation was performed by Kim, Moin, and Moser (1987). The numerical method consists of spectral method - Fourier series in both the spanwise and streamwise directions with Chebychev polynomials in the wall normal direction. The Reynolds number based on friction velocity and channel half-height was 180. It was found that although good agreement was obtained in the turbulence statistics, the Reynolds stresses were consistently lower than the experimental values, yet the computed vorticity near-wall fluctuations were higher than experimental results. They suggest possible error in the experiment and renormalize the experimental data by a corrected shear velocity and obtain excellent agreement except with the calculated turbulence intensities, which still remain lower than the experimentally reported values.

In complex geometries, it is often necessary to use unstructured grids to resolve the flow. Simons and Pletcher (1998) consider isotropic turbulence and channel flow, using 3 SGS models for the isotropic case: the monotone integrated large eddy simulation (MILES) which does not use a specific model but rather the numerical dissipation as the eddy viscosity, the Smagorinsky model, and the dynamic model of Germano. A tetrahedral and hexahedral finite volume formulation are used to construct the unstructured mesh. Both methods gave good results for isotropic turbulence, however, difficulty was encountered which prevented the tetrahedral grid from being used in channel flow. For channel flow, the Smagorinsky model was modified with a wall damping function and was the only SGS model considered for the channel simulation. The rms quantities are slightly underpredicted for a Reynolds number of 2800 based on channel half-height and bulk velocity.

Turbulent recirculating flows have been widely studied due to their complex eddy structure and engineering importance. Zang, Street, and Koseff (1993) chose the lid-driven cavity to study with LES. The dynamic mixed model was used in conjunction with a finite volume method to simulate Reynolds numbers of 3200, 7500 and 10000. A multigrid method is used to solve the Poisson equation, and the equations are discretized on a nonstaggered stretched grid. Excellent agreement in the mean statistics is obtained when compared to experimental data. The rms statistics also compare favorably along the centerplane, with slight underprediction near the top and downstream walls. A derivation is given to show the proper way to compare experimentally measured Reynolds stresses, which contain contributions from large and small scales, to LES measured Reynolds stresses, which contain only large scales.

Jordan and Ragab (1994) examine the lid-driven cavity with LES and DNS. LES with the Smagorinsky model and van Driest damping is used for Re = 10000, whereas DNS is used for laminar flow at Re=5000. Both techniques are compared at Re = 7500. They examine the Taylor-Görtler-like (TGL) vortices formed in the spanwise plane. They find that the TGL vortices break down at Re=10000 according to the LES predictions. They claim that at Re = 5000, the flow is still laminar and the TGL vortices change rapidly in size, with 9 TGL vortex pairs along the cavity bottom. But at Re = 10000, the turbulence begins to distort the vortex pairs. Near the downstream secondary eddy (DSE), the DSE is found to feed fluid to the TGL pairs which also entrain more fluid from the primary recirculation vortex. Upstream of the DSE, the TGL vortex pairs entrain fluid directly from the main recirculation region. For a comprehensive review of driven-cavity flows see Shankar et al. (2000).

The backward step has been a critical benchmark for turbulence codes, and a detailed review of two-equation models for backward steps is presented in Thangam and Speziale (1992). They report two major sources of

errors in k-ε equations, the first being inadequate grid resolution and the second being improper modeling of the Reynolds stresses. They state that a properly tuned two-equation k-ε model can give surprisingly accurate results, especially compared to previous one-equation models or the so-called zero-equation model. For instance, when the standard k-ε model was modified to include anisotropic eddy viscosity, the reattachment point was found to be within 3% of experimental values, compared to 12% for models with three-layer wall functions.

A 2-D highly resolved backward step calculation was performed by Thangam and Hur (1991). The finite volume method is used with two versions of the k-ε equations, a standard and nonlinear model. They find that even with fine resolution (166x73 and 332x146) the standard model is unable to predict the flow field and that nonlinear terms must be incorporated into the model to account for normal stress differences. However, only 10% accuracy is obtained when compared to the experimental reattachment length, indicating that even the best k-ε model is still short of completely predicting the flow.

The stability of backward step flow at Re = 800 was studied by Gresho et al. (1993). Four 2-D codes were used: a finite element code with time marching for the unsteady equations, a finite element method for the steady equations and stability problem, a second-order finite difference method to solve the equations in streamfunction form, and a spectral method. With each code, they concluded that the flow was both steady and stable for any size perturbation. This study was undertaken due to the statement of other researchers who claimed the flow to be transient, but this work could find no so such transient features.

Neto et al. (1993) used DNS and LES to simulate the vortices in backward facing step flow. For LES, they choose a structure-function SGS model. A finite volume code with a staggered grid is used. White noise is imposed upon an inflow velocity field to simulate the turbulence. Two cases were considered, a low step and high step case. The former was at Re = 38000 and the latter was at Re = 6000, based on step height and inlet free stream velocity. A fully developed outflow condition is imposed at $x/h \approx 30$. They show that the coherent vortical structure of the flow is similar to a two-dimensional forced mixing layer which has main vortices shed after the step and then secondary longitudinal hairpin vortices between them. Their structure-function LES is found to compare better with experiments than a Smagorinsky model or k-ε models.

A DNS calculation of a backward facing step was performed by Le, Moin, and Kim (1997). A staggered grid is used with a convective outflow condition. They show that the effects of the outflow condition are confined to within one step height of the exit. They used a Reynolds number of 5100 based on step height and inlet free-stream velocity and they considered an expansion ratio of 1.2. When studying the reattachment length, they found oscillatory behavior in its location. They attribute this to a large-scale shear layer structure curling up behind the step and growing, then once it eventually detaches the reattachment length suddenly decreases as another structure begins to grow. They also used four different methods to determine the reattachment length: the location of the first grid point away from the wall with zero mean streamwise velocity, the location of zero wall shear stress, the location of the mean dividing streamline, and a p.d.f. method where the location is defined as where the flow has a 50% forward flow fraction. They find that the first three methods are within 0.1% of each other, and only 2% from the p.d.f. approach. They report a mean reattachment length of 6.28h. They observe negative skin friction in the recirculation region, and positive skin friction in a secondary recirculation bubble near the step's lower corner (0.05

< x/h < 1.0). Excellent agreement in the mean velocity is obtained when compared to experiments. They also indicate that the flow has not fully recovered at a distance of x/h = 20.

In an effort to reduce computational costs in resolving the near wall region, Nikitin et al. (2000) have proposed the concept of detached-eddy simulation (DES). In DES, the near wall region is represented by a RANS model and the core region is modeled with LES. Their DES model was applied in channel flow at various Reynolds numbers. Using three different codes, which are in agreement with each other, they find that the skin friction coefficient is roughly 15% low. Also, by varying the grid and Reynolds number, they experience trade-off problems with the accuracy of the viscous, modeled, and resolved shear stress.

One reason that the second-order central differencing approach is popular is that it is energy conserving. However, an increase in accuracy would give less numerical dissipation and the effect of subgrid models would be more easily seen. In a recent paper by Gullbrand (2000), a conservative fourth-order code is used in turbulent channel flow. Data are compared to the results from a spectral DNS code and a second-order finite difference code. A staggered grid is used and the convective term is written in a skew-symmetric form to ensure conservation of kinetic energy. A 128x128x128 grid is used and excellent agreement is obtained at Re_τ=180 when comparing the mean and rms velocities. Little difference is shown between the second and fourth-order codes. Neither the fourth-order or second-order code can match the spectra produced by the spectral code at high wavenumbers, which is expected due to the implicit top-hat filtering in any finite volume type code. LES is used on a 69x49x48 grid with the dynamic Smagorinsky model at Re_τ = 395. The mean velocity is predicted well, while the rms quantities are underpredicted in the wall and spanwise directions, and overpredicted in the streamwise directions. Again, the spectra show that the high wavenumbers are contaminated from numerical errors.

To enhance the code developed in this research work, CART3D, it would be of engineering importance to implement a cut-cell method which allows arbitrary geometries to be studied. The Cartesian method allows higher order spatial discretizations to be incorporated efficiently. There are various methods of incorporating cut-cells into a Cartesian framework, as illustrated in Ye et al. (1999) and Johansen and Colella (1998). The method outlined in Gullbrand, Bai, and Fuchs (1998) will be considered here. Consider the following example in Figure 3.3.1. An arbitrary wall has been placed in a Cartesian grid. To ensure the high order accuracy near the wall, the cut-cell approach in the reference above is outlined in the following manner. Three cell types may be identified: an interior cell which does not intersect the wall, a cut-cell which is intersected by a wall, and a wall cell which remains totally outside the wall. Higher order Lagrangian interpolation is used to find the dependant variables at cut cells and wall cells. Extrapolation is sometimes necessary for wall cells. To find the values of scalars at the wall which have a boundary condition of zero normal derivatives (such as species mass fraction), a line normal to the wall is drawn which passes through point P, the cell center of the cut-cell. To interpolate the value at C, points P, B, A, D and E are used. To determine the values of the scalar at point A, for example, the cell centers of interior cells are interpolated, in this case points Q, R, S and T. Similarly for the other points along the normal. One can obtain the values at point P by setting the normal derivative to zero at C in this manner. Velocity components may be interpolated in a similar fashion by requiring no slip at the wall and interpolating to find desired interior values. This cut-cell method will allow any geometry to be modeled by the enhanced code.

3.4 Gas-Particle Flows

3.4.1 Experiments

Kulick, Fessler, and Eaton (1994) used LDV to study the interaction of particles and turbulence in channel flow. Mass loadings of up to 80% were considered for 50 and 90 μm glass and 70 μm copper particles. They found that the fluid turbulence was decreased by the particles, with more attenuation at larger Stokes numbers and less modification in the streamwise direction compared to the cross-stream directions. They attribute this to the particles being unable to respond to the high frequency fluctuations in the cross-stream directions. A greater degree of turbulence attenuation was found in channel flow when compared with isotropic turbulence. The fluid mean velocity profiles were unmodified by the particles.

The preferential concentration of heavy particles by turbulence has been studied experimentally in a channel flow by Fessler, Kulick, and Eaton (1994). Photographs were taken by illuminating the flow with a laser sheet. Several particle sizes were studied including 25, 50 and 90 μm glass, 70 μm copper, and 28 μm Lycopodium. Maximum preferential concentration of particles is found when the Stokes number based on the Kolmogorov time scale is approximately one. They find that their experimental Stokes number prediction for maximum concentration is slightly higher than what is given computationally by other researchers. They say this may be due to their using larger experimental grid spacing in their photographs when compared to the grid spacing in computations.

Experimental PIV measurements of particle-laden channel flow were made by Paris and Eaton (1999). They used 150 μm glass particles which had a Stokes number of 97 based on the Kolmogorov time scale at the channel center plane. At 25% mass loading, the lateral and longitudinal velocity correlation functions display a modification of the functions at large length scales when compared to the unladen case. They also find a decrease in dissipation with higher mass loadings. They claim this is due to a decrease in the turbulence level of the continuous phase with an increase in mass loading. And since the dissipation must balance the turbulence production for a fully developed channel, the dissipation had to decrease with an increase in mass loading.

The backward-facing step flow with particles was studied with LDV by Fessler and Eaton (1997). They used particles having Stokes numbers from 0.5 to 7.4. They found that large particles ($St > 3$) did not enter the recirculation zone. The smallest particles did enter the recirculation zone and demonstrated that they follow the large-scale structures. Within the shear layer, the fluid had higher wall normal fluctuations than the particles, yet the particles had higher streamwise fluctuations. They say the latter is due to cross-stream mixing of particles, where particles of high inertia cross over into low speed regions of fluid. This is supported by high Stokes number particles displaying even higher streamwise fluctuations. They were able to find no consistent trend when the mass loading was varied. They also seeded particles within the shear layer and showed that the particles concentrate in the high strain rate regions between vortices.

An experimental study of turbulence modification by particles in a backward-facing step was performed by Fessler and Eaton (1999). Three particle sizes were considered, 90 and 150 μm glass spheres and 70 μm copper spheres, with 3-40% mass loading. LDV was used to measure all velocities in the study. Since the Stokes number for all particles were larger than one, few particles were entrained into the recirculation region. The gas phase mean velocity was not significantly changed by the presence of particles. The particles tended to lag behind the fluid

velocity near the step, indicating a negative slip. However, since the fluid must decelerate after expansion, the particles then exceeded the fluid velocity far downstream of the step. No measurable change in the turbulence was seen with the 90 μm glass particles. The other two particle classes did show turbulence modification for high mass loadings, especially above y/h > 1. Turbulent fluctuations were reduced by as much as 35% for 40% mass loading of the 150 μm glass particles.

Turbulence modification by particles in a water tank was studied experimentally by Parthasarathy and Faeth (1990a). They used LDV to measure the particle velocity fluctuations as well as the one- and two-point correlations of fluid velocity fluctuations. Glass particles of 0.5, 1 and 2 mm were used which represents a much larger particle size range than other researchers have used. They found that the streamwise fluid velocity fluctuations were roughly twice that of the cross-stream direction fluctuations, indicating that the particle wakes were significant. They also state that the velocity fluctuations can be correlated based on the rate of dissipation of particle energy in the fluid. Parthasarathy and Faeth (1990b) also studied the turbulent dispersion of particles in water using LDV. They compare the standard drag curve for a sphere to their experimentally observed drag, and find the two values are within 14% of each other. This is partly due to the experimental particles containing a fraction that are slightly elliptic in shape, rather than spherical. The particle velocity fluctuations were larger than the liquid velocity fluctuations for all test conditions. Using probability density functions to stochastically simulate the particle motion, they suggest that the turbulent dispersion may be more accurately simulated via this approach than earlier methods which contain *ad hoc* elements which should be avoided.

An axisymmetric round jet laden with 55 μm glass particles was studied with LDV and flow visualization by Longmire and Eaton (1992). They find that for light mass loadings, the structure of the jet is very similar to a single-phase jet. Vortex ring structures dominate the near-field of the jet and persist in jets with mass loadings up to 0.65. They conclude that dispersion is dominated by convection rather than diffusion. Preferential concentration of particles is seen near the vortex ring structures. The particles tend to collect in the "saddle" regions between vortices.

Crowe et al. (1995) have observed that in the wake of a bluff body, particles tend to accumulate along the edges of vortex structures. They term this phenomenon “focusing”, analogous to the preferential concentration which is the topic of this work. Particles with a Stokes number (St) of unity are found to exhibit the maximum focusing. However, they only studied Stokes numbers of 0.01, 1.0, and 100, which do not accurately resolve the trend around St = 1, where the focusing effect is maximum.

In a mixing layer, Tageldin and Cetegen (1997) experimentally observed size-selective dispersion of droplets. They found rapid entrainment of small droplets and found a much slower entrainment of large droplets due to Stokes number effects. This confirms the findings of Lazaro and Lasheras (1992a, 1992b) who also mention that the particle concentration field is related to the streaky nature of the large-scale structures.

3.4.2 Computations

DNS was used by Squires and Eaton (1990) to understand the modification of isotropic turbulence by particles. It was found that particles collect in regions of low vorticity and high strain rate. The range of Stokes numbers was from 0.075 to 1.5, based on the longitudinal integral length scale and square root of 1/3 of the kinetic

energy. Extremely light particles were found to demonstrate less preferential concentration, and extremely heavy particles exhibited no preferential concentration since they did not respond to flow fluctuations. The energy and dissipation spectra at high wavenumbers were found to increase with the addition of particles. They state that the heavy particles tend to modify the turbulence more homogeneously than the small particles do. With an increase in mass loading, the smaller particles reduced their trend of preferential concentration in low vorticity regions, while particles with larger time constants increased the tendency to collect in low vorticity regions.

Particle dispersion in isotropic turbulence was studied with DNS by Squires and Eaton (1991a). Particle dispersion was seen to decrease significantly in the presence of an external body force. This reduction was found to be greater in directions normal to the particle drift compared to directions parallel to the drift. Good agreement with experiments was obtained. The particle inertia was found to increase the eddy diffusivity of particles, with between 2 to 16% increases seen over that of the fluid.

DNS was used to track the trajectories of 10^6 particles in the work of Squires and Eaton (1991b). Isotropic turbulence was considered and the computational grid contained 64^3 points. Stokes numbers of 0.075, 0.15, and 0.52 were considered. Particles were shown to collect in regions of low vorticity and high strain rate, with the most severe preferential concentration taking place for St=0.15. This suggests that instead of enhancing mixing, turbulence may inhibit the mixing of particles. They support this by stating that instantaneous number densities were seen as much as 25 times the mean value.

Using DNS, Elghobashi and Truesdell (1992) studied the dispersion of particles in decaying isotropic turbulence. They include viscous and pressure drag forces, force due to fluid pressure gradient, an added mass inertial force, Basset force, and gravity. A second-order staggered finite difference code with 96^3 grid points is used. Three particle classes are studied (corn, glass, copper). To allow time for the particles to adjust to the turbulence and remove any error with the initial particle conditions, the mean-square relative velocity is used as a measure to decide when the particles became independent of their initial injection. They compare the mean-square displacement of the particles to experiments and obtain good agreement. The velocity frequency spectra of the particles without considering gravity shows that at low wavenumbers, the turbulence energy of the particles is greater than that of the surrounding fluid. They show that in the gravity direction, the dominant forces are buoyancy and drag.

The modification of turbulence due to the presence of small solid particles is studied via DNS by Elghobashi and Truesdell (1993). They find that the particles augment the turbulence energy at high wavenumbers. An increase in the dissipation rate is seen when particles are present which indicates a faster transfer of energy from the large scales to the small scales. The energy also decays faster with particles than without particles. An anisotropic transfer of energy to the small scales is seen when gravity is included. The two-way coupling effects are found to be larger at higher volume fractions.

Considering only the drag force on the particles, Boivin, Simonin, and Squires (1998) used DNS to simulate particle laden isotropic turbulence on a 96^3 grid. They neglect particle-particle collisions and gravitational settling. It is found that the particles dissipate more kinetic energy as the mass loading increases, while at the same time being independent of the particle relaxation time. They also state that the particles transfer energy from the

large scales of motion back to the small scales of motion, thereby modifying the turbulence. They point out that in two-way coupling, it may not be appropriate to describe the coupling in terms of the small-scale variable since the turbulence is distorted across the entire spectrum. They say that higher Reynolds numbers must be considered before that conclusion can be drawn.

Boivin, Simonin, and Squires (2000) considered LES of gas-particle isotropic turbulence using *a priori* testing of several SGS models, including the Smagorinsky model, scale-similarity, dynamic Smagorinsky, and dynamic mixed model. The dynamic mixed model accurately predicted the p.d.f. of the subgrid dissipation in the *a priori* study. Some *a posteriori* testing was done with the dynamic mixed model. They show that the dynamic mixed model correctly predicts the spectra, with particles transferring energy to the high wavenumbers. They point out that in LES, the SGS model may be less important since some of the dissipation is handled through fluid-particle interaction particularly at high mass loadings.

Uijttewaal and Oliemans (1996) examined particle dispersion and deposition in vertical pipes. They used both LES and DNS to study friction Reynolds numbers of 360, 1000, and 2100 and a range of dimensionless particle relaxation times from 5 to 10^4. They find that the deposition coefficient scales with the turbulence integral time scale. The wall impact velocity is seen to peak around $\tau_p^+ = 200$. They state that the use of larger particles is questionable as it leads to large particle Reynolds numbers which are not appropriate when using the Saffman lift force. To more accurately represent the dispersion of small particles, they suggest taking into account the effects of the subgrid turbulence on the particle motion, a suggestion that we employ by adding subgrid fluctuations (calculated from a dynamic subgrid kinetic energy model) to the fluid velocity at the particle positions.

Brooke, Hanratty, and McLaughlin (1994) looked at the free-flight mixing and deposition of aerosol particles using DNS in channel flow. They find that particles deposit in one of two ways: diffusion to the wall and free flight towards the wall. The latter is seen to be the dominant mechanism. Free flight of a particle is assumed to begin when the velocity of a particle and fluid element are equal at a location. They mention that particles do get trapped at the wall, and if a long enough time passes, they may deposit due to diffusion. But they point out it is more likely that they will be ejected from the near wall layer, and then travel back to the wall in free flight and deposit in that manner.

Large Eddy Simulation was used by Wang and Squires (1996a) to study particle laden channel flow at Re_τ=180 and 644. Neglecting particle-particle collisions, they used the dynamic eddy viscosity model and included drag and gravitational forces. By only considering one-way coupling, the carrier phase was not modified by the particles. They include a SGS kinetic energy equation and add the SGS fluctuations to the particle velocity and show that the SGS fluctuations contribute to less than 1% change in the particle rms fluctuations. Three particle types are considered: 28 μm Lycopodium, 50 μm glass and 70 μm copper. They followed the trajectories of 250,000 particles to obtain the particle statistics. This number of particles was shown to be sufficient for resolving the statistics. Near the wall, the Lycopodium particles closely match the mean carrier flow, with a slight lag since the particles tend to collect in low speed streaks. The glass and copper particles are seen to have higher velocities than the fluid, which agrees with experimental data at Re_τ=180. However, at Re_τ = 644, there are significant differences in the LES and previous experimental data. The experiments show the particles matching the fluid

velocity at $y^+>10$, while the LES shows the particles leading the flow throughout the domain. Also, the particle velocities are experimentally shown to increase near the wall at this higher Reynolds number, something LES does not predict. This could be due to the poor near wall resolution of LES. The rms quantities compare well at $Re_\tau=180$, and good agreement is obtained at $y^+>10$ for $Re_\tau = 644$. Again, the near-wall region shows poor agreement at this higher Reynolds number. However, even some past DNS calculations show poor agreement in particle statistics near the wall, indicating that perhaps the wall collision model is in error (elastic collisions were assumed). The LES simulations reproduced the preferential concentration of particles by turbulence near the wall and near the centerline.

Particle deposition in channel flow was studied with LES by Wang and Squires (1996b). This study used the dynamic model of Germano in conjunction with a one-way coupling approach. Reynolds numbers of 180 and 1000 were examined, based on channel half-width and friction velocity. They assumed that particle deposition occurred whenever a particle was within one radius of the wall. The initial particle velocities were equal to the local fluid velocity and 20,000 particles were randomly placed in the channel for each time constant. They include a shear-lift force which is shown to be small in comparison to the drag. The streamwise velocity slip ratio is found to be larger than the wall normal slip ratio. The maximum particle concentration is found near the wall. When the results are compared with DNS, the particles with the largest relaxation times are found to compare the best. This is because LES accurately simulates the large-scales, and the largest particles are most likely to be influenced by the large-scales. To account for not resolving the small-scales, Schumann's model is used to add a SGS fluctuation to the particle. They find almost no effect of this fluctuation on large particles ($\tau^+ = 6$), with small particles ($\tau^+ = 2$) being affected by as much as 30% in the ratio of wall-normal component of averaged fluid velocity for depositing particles to wall-normal turbulence intensity. It is also found that the lift force increases the particle deposition.

DNS of particle deposition in a channel with a free slip surface was examined by van Haarlem, Boersma, and Nieuwstadt (1998). They studied two particle classes, $\tau_p^+ = 5$ and 15, and used 200,000 particles for each class. One-way coupling was assumed. For $\tau_p^+ = 5$, deposition rates are higher for the free slip channel than the no-slip channel. But for $\tau_p^+ = 15$, trend is reversed. For either case, $\tau_p^+ = 15$ had higher deposition rates than $\tau_p^+ = 5$. They find that particles which deposit were brought to the wall by fluctuations which originated far from the wall, confirming the free flight study done by Brooke, Hanratty, and McLaughlin (1994).

Zhang and Ahmadi (2000) examined aerosol particle transport and deposition in channels. A $16\times64\times64$ grid without a subgrid model is used for the simulations. Their particle equation of motion includes lift, drag, gravity and Brownian diffusion. Brownian diffusion is shown to be important for particles smaller than 0.1 μm. 8192 particles were used in their simulations to evaluate statistics. For horizontal ducts, they found that gravity increases deposition by sedimentation on the lower wall. For vertical ducts, when gravity was in the flow direction, deposition rates were higher since when gravity is in the flow direction the lift force will act towards the walls.

The dispersion of small, dense particles in a planar shear layer between two fluids of different density and viscosity was the subject in Soteriou and Yang (1999). The Lagrangian transport element method (TEM) is used to obtain the numerical solution. They vary the Stokes number to arrive at the following conclusions: at small Stokes numbers the particles follow the flow and are dispersed in proportion to the growth of the shear layer, at moderate

Stokes numbers the particles disperse beyond the shear region, and at large Stokes numbers the particles are unaffected with minimal dispersion. By varying the viscosity ratio, the trend of particle dispersion with Stokes number still held, only the values at which different behaviors were observed shifted. The magnitude of the dispersion was found to decrease with an increase in the viscosity ratio of the two fluids. Dispersion was found to decrease with any amount of variable density for the moderate Stokes number particles. Small particles were found to have an increase in dispersion with increasing density ratio.

DNS and LES of particle motion was done by Armenio, Piomelli, and and Fiorotto (1999) to study the effect of SGS velocity fluctuations in channel flow at Re_τ=175. Two subgrid models were used, the Smagorinsky model and its dynamic formulation. The DNS data were filtered to remove the small scales and study the effect of filtering on particle dispersion. This removed any modeling errors since the filtering was done *a posteriori*. They found that the dispersion is not strongly dependent on small-scale motion. Two grids were considered for LES, 48x48x97 and 64x64x97. They found that the Lagrangian statistics were very sensitive to the modeling errors. The fine grid LES dispersion statistics compared to within 8% of the DNS results. The Smagorinsky model gave poor estimations of the statistics. They conclude that a fine grid with an accurate SGS model can give good particle statistics.

A discrete vortex model was used by Chung and Troutt (1988) to study particle dispersion in an axisymmetric jet. They state that the Stokes number is the crucial parameter in determining particle dispersion in a jet. They say that for Stokes numbers on the order of one may be dispersed faster than the fluid. Small Stokes numbers were found to disperse at the fluid dispersion rate. Large particles were found to disperse less than the fluid dispersion rate. The jet mean and fluctuating velocities compared well with experiments.

DNS was used to simulate particle dispersion in a mixing layer by Ling et al. (1998). They show that the streamwise large-scale structures develop from initial perturbations and the unstable wavelength in the spanwise direction is shown to be roughly two-thirds of the unstable wavelength in the streamwise direction. They claim the particle dispersion in the three-dimensional mixing layer is dominated by two-dimensional structures. Particles with Stokes numbers of order one are shown to preferentially concentrate at the perimeter of the large-scale structures.

Yang et al. (2000) performed experiments in a plane wake to determine the particle dispersion properties. Knowing that the vortex structures can highly concentrate particles, they use laser pulsed imaging to visualize glass beads in the wake of a blunt trailing edge. They use two sizes of particles, 10 and 30 μm, with air as the continuous phase. They find that particles with Stokes number of order one (St = $1.44 \pm 44\%$) have the largest dispersion in the cross stream direction, even significantly greater than small Stokes number particles (St = $0.15 \pm 44\%$) which essentially follow the flow fluctuations. The uncertainty in the Stokes number arises from a range of $\pm 20\%$ standard deviation in the diameter. This trend in dispersion is in agreement with past studies, both numerical and experimental.

It is known that particles in isotropic turbulence preferentially accumulate in regions of low vorticity and high strain-rate (Squires and Eaton 1991b). Ferry and Balachandar (2001) examined channel flow and showed that other fluid statistics, such as the swirling strength, λ_i, and maximum strain, σ_u, provide a better indication of the preferential concentration of particles. They demonstrated that particles collect in regions of low λ_i and high σ_u. The

swirling strength, which is the magnitude of the imaginary part of the complex conjugate eigenvalue pair of the fluid velocity gradient tensor, has been used to identify vortices (Zhou et al. 1998; Adrian, Balachandar, and Liu 2001). The swirling strength is zero at locations where the eigenvalues of $\nabla\mathbf{u}$ are all real. A positive value of λ_i corresponds to a local dominance of rotation-rate over strain-rate (Adrian et al. 2001). Vorticity can arise from either swirling or shear. However, it is the swirl that has a greater centrifugal effect on particles than shear and hence swirling strength is a better choice than vorticity for preferential concentration studies. The maximum strain, σ_u, is the minimal eigenvalue of the strain-rate tensor. Other quantities which are useful in identifying regions of preferential concentration of particles include $\nabla\mathbf{u}:\nabla\mathbf{u}$ and enstrophy (Druzhinin and Elghobashi 1998).

To fully appreciate the meaning of $\nabla\mathbf{u}:\nabla\mathbf{u}$, one must examine its derivation. Consider an Eulerian formulation of the particle velocity field. To first order, if one neglects body forces, the particle velocity field, $\mathbf{u}_p$, may be expressed as a function of the fluid velocity field, $\mathbf{u}$, and particle response time, t_p, as follows

$$\mathbf{u}_p = \mathbf{u} - t_p\left(\frac{\partial \mathbf{u}}{\partial t} + \mathbf{u}\cdot\nabla\mathbf{u}\right) \tag{3.4.2.1}$$

Maxey (1987) has shown that this particle velocity field is not divergence free. Taking the divergence of (3.4.2.1) gives

$$\nabla\cdot\mathbf{u}_p = -t_p\frac{\partial u_j}{\partial x_i}\frac{\partial u_i}{\partial x_j} = -t_p\nabla\mathbf{u}:\nabla\mathbf{u} \tag{3.4.2.2}$$

It is clear from (3.4.2.2) that particles will accumulate where $\nabla\mathbf{u}:\nabla\mathbf{u}$ is positive.

Recently, Vance and Squires (2002) studied the parallel implementation of a Eulerian-Lagrangian two-phase flow model. They considered one-way coupling with collisions in a turbulent channel flow. The particle equation of motion included drag and gravity. Subgrid fluctuations are neglected when interpolating the fluid velocity to a particle position. Their collision detection algorithm achieves nearly perfect parallel speedup whereas their fluid calculation lags in parallel performance due to its inability to efficiently run on parallel machines. They test their method on machines with up to 32 processors. Even with parallel processing, the bulk of the total calculation time resides in the detection of particle-particle collisions. Their algorithm divides the domain into partitions and a particle is allowed to collide with any particle in the 27 neighbor cells surrounding the particle. They state that this is sufficient to detect all binary collisions within a time step. They discuss how to partition the domain to reduce communication costs between processors during the particle transport calculation.

Turbulence modulation in a rotating channel flow was studied using DNS by Pan, Tanaka, and Tsuji (2002). They find that for large particles, the inclusion of particle-particle collisions yields higher turbulent kinetic energy compared to the case of no collisions. Near the center of the duct, the collisions augment the turbulence energy at low wave numbers. Near the walls, the entire spectrum is augmented due to collisions. A hard-sphere model was used when considering collisions. They showed that turbulence kinetic energy may be transferred from the streamwise direction to the other directions through collisions in a rotating channel.

The behavior of small particles in the wall region of a horizontal channel was studied using DNS by Pedinotti, Mariotti, and Banerjee (1992). One-way coupling was assumed in their simulations. More uniform

distributions were found for particles with very small and very large time constants. When the dimensionless time constant was approximately 3 (based on the friction velocity and kinematic viscosity), the maximum preferential concentration was observed. This was examined by studying the presence of particles in low speed streaks. Qualitative agreement with experiments is seen, but due to the higher Reynolds number of the experiments, a direct conclusion about the differences cannot be made.

Wang and James (1999) use an Eddy Interaction Model (EIM) to simulate gas-particle channel flow. EIM reconstructs the instantaneous flow field from the mean flow field and assumes that it is comprised of eddies whose lifetimes and length scales can be figured from the mean quantities. Standard two-equation turbulence models are used to provide this information, therefore the reconstructed fluctuations are isotropic, which is a drawback of the method in highly anisotropic regions such as near walls. They attempt to correct this flaw by incorporating damping functions into the EIM, and achieve improved results when compared to the standard EIM. Deposition velocities are in good agreement with experiments, except for small particles which they attribute to the lack of a lift force in their calculations.

Wang et al. (1997) study the effect of the lift force on particle deposition velocity in turbulent flow using LES. They state that the Saffman formula overpredicts the deposition velocity when compared to experiments. They develop an "optimum" lift force which they state is the most accurate to expression to date. This optimum force is three times smaller than the Saffman force. They find that the optimum force makes the deposition velocity less dependant upon the particle relaxation time. However, they also note that neglecting the lift force completely gives even better results when compared to the experiments.

Chapter 4. Governing Equations and Numerical Methods

In this chapter, the governing equations and the associated numerical methods used in this research for the LES calculations of fully-developed turbulent flow through a duct of square cross-section are discussed. In Section 4.1, the governing equations for the fluid and particles are discussed along with the filtering procedure. In Section 4.2, the numerical methods used to solve the governing equations for the fluid flow and particle transport are described. In Section 4.3, the algorithm for interparticle collisions is described. In Section 4.4, the code validation results are presented.

4.1 Governing Equations for the Large Eddy Simulations

In the current study, the Navier-Stokes equations for incompressible, three-dimensional flow are solved in Cartesian coordinates. The governing equations in their non-dimensional form are:

$$\nabla \cdot \mathbf{u} = 0 \tag{4.1.1}$$

$$\frac{\partial \mathbf{u}}{\partial \mathbf{t}} + \nabla \cdot (\mathbf{uu}) = -\nabla p + \frac{1}{\mathrm{Re}} \nabla \cdot \nabla \mathbf{u} - \boldsymbol{f} \tag{4.1.2}$$

The velocity and length scales used to non-dimensionalize the above equations are the friction velocity, u_τ, and square duct width, d, respectively. The time scale then becomes d/u_τ. Since one-way coupling is being considered, there is no particle force term in the momentum equation. The term $\boldsymbol{f}$ on the right hand side of (4.1.2) represents the sum of the forces exerted by the fluid on the particles (drag and lift) and is the effect of two-way coupling. This term is zero for one-way coupling simulations. The effect of particles on the fluid are included in the Navier-Stokes equations as point forces acting at the particle centers. Since the particle locations do not necessarily coincide with the fluid velocity grid locations, $\boldsymbol{f}$ must be calculated at the fluid velocity positions.

In our calculations, a given particle contributes to a finite stencil of fluid grid points surrounding the particle. This approach requires the calculation of fluid velocities at the particle position. This involves interpolation of the surrounding fluid velocities to a given particle location, known as forward interpolation. Second degree Lagrange polynomials are used for interpolation, which involve 27 surrounding fluid grid points. Once $\boldsymbol{f}$ at a particle location has been calculated, it is interpolated back to the 27 surrounding grid points, called backward interpolation. This is done using the same Lagrange weighting functions that were calculated using forward interpolation. Sundaram and Collins (1996) have shown that forward and backward interpolations should be symmetric for accurate numerical representation of the overall (fluid + particle) energy balance equation.

If one were to filter the Navier-Stokes equations such that only the large scales of motion were simulated and the effects of the small scales were replaced with a model, one would arrive at the fundamental principle of Large Eddy Simulation (LES). The filtered variable $\overline{\chi} = \chi - \chi'$, where χ' is the unresolved portion of the variable, is defined by:

$$\overline{\chi}(x_1, x_2, x_3, t) = \int_{-\infty}^{\infty}\int\int \left(G_i(x_i - x_i')\right)\chi(x_1', x_2', x_3', t)\,dx_1'\,dx_2'\,dx_3' \tag{4.1.3}$$

In wave space, the equivalent form of the filtered variable is:

$$\overline{\chi}(k_1, k_2, k_3, t) = \prod_{i=1}^{3} \left(G_i(k_i)\right) f(k_1, k_2, k_3, t) \tag{4.1.4}$$

where $G_i(x_i - x_i')$ and $G_i(k_i)$ is the filter function which satisfies

$$\int_{-\infty}^{\infty}\int\int \left(\prod_{i=1}^{3} G_i(x_i - x_i') \right) dx_1' dx_2' dx_3' = 1 \tag{4.1.5}$$

After one filters the Navier-Stokes equations, the filtered form becomes the following:

$$\frac{\partial \overline{u}_j}{\partial x_j} = 0 \tag{4.1.6}$$

$$\frac{\partial \overline{u}_i}{\partial t} + \frac{\partial}{\partial x_j}\left(\overline{\overline{u}_i \overline{u}_j} + \overline{\overline{u}_i u_j'} + \overline{u_i' \overline{u}_j} + \overline{u_i' u_j'}\right) = -\frac{\partial \overline{p}}{\partial x_i} + \frac{1}{\mathrm{Re}_\tau}\frac{\partial^2 \overline{u}_i}{\partial x_j \partial x_j} - \bar{f}_i + 4\delta_{i3} \tag{4.1.7}$$

Let the last three terms in the convective derivative be defined as the sub-grid stresses, Q_{ij}:

$$Q_{ij} = -\left(\overline{\overline{u}_i u_j'} + \overline{u_i' \overline{u}_j} + \overline{u_i' u_j'}\right) \tag{4.1.8}$$

The sub-grid scale (SGS) stresses should be consistent upon contraction (i=j). A new variable t_{ij} and a modified pressure $\overline{P}$ are defined as follows:

$$t_{ij} = Q_{ij} - \frac{1}{3} Q_{kk} d_{ij} \tag{4.1.9}$$

$$\overline{P} = \overline{p} + \frac{1}{3} Q_{kk} \tag{4.1.10}$$

Commonly, an eddy viscosity model is chosen to represent the SGS stresses in terms of an eddy viscosity, also called turbulent viscosity, as follows:

$$t_{ij} = 2\nu_T S_{ij}, \quad S_{ij} = \frac{1}{2}\left(\frac{\partial \overline{u}_i}{\partial x_j} + \frac{\partial \overline{u}_j}{\partial x_i}\right) \tag{4.1.11}$$

where S_{ij} is the strain rate tensor and ν_T is the eddy viscosity. There are many methods of calculating the eddy viscosity, and those models will be discussed in the next section.

There are several filters available for LES, such as the spectral cut-off filter, Gaussian filters, and top-hat filters. The top-hat filter has been chosen for all spatial directions in this work. After substitution, the momentum equation becomes the following:

$$\frac{\partial \overline{u}_i}{\partial t} + \frac{\partial}{\partial x_j}\left(\overline{u}_i \overline{u}_j\right) = -\frac{\partial \overline{P}}{\partial x_i} + \frac{\partial}{\partial x_j}\left[\left(\frac{1}{\mathrm{Re}_\tau} + \nu_T\right)\frac{\partial \overline{u}_i}{\partial x_j}\right] + \frac{\partial}{\partial x_j}\left(\nu_T \frac{\partial \overline{u}_j}{\partial x_i}\right) - \bar{f}_i + 4\delta_{i3} \tag{4.1.12}$$

The particle equation of motion is given in detail by Maxey and Riley (1983). The form used in this work may be expressed as follows:

$$m_p \frac{d\mathbf{u}_p}{dt} = m_p \frac{\left(\mathbf{u}(x_p) - \mathbf{u}_p\right)}{t_p} + \left(m_p - m_f\right)\mathbf{g} + 3.08 m_p \frac{\nu^{1/2}}{d_p \frac{?_p}{?_f}} \left(w - w_p\right) \left|\frac{\partial w}{\partial x}\right|^{1/2} \operatorname{sgn}\left(\frac{\partial w}{\partial x}\right) d_{i1}$$
$$+ 3.08 m_p \frac{\nu^{1/2}}{d_p \frac{?_p}{?_f}} \left(w - w_p\right) \left|\frac{\partial w}{\partial y}\right|^{1/2} \operatorname{sgn}\left(\frac{\partial w}{\partial y}\right) d_{i2} \qquad (4.1.13)$$

where $\mathbf{v}$ is the particle velocity vector, m_p is the particle mass, $\mathbf{g}$ is gravitational acceleration, and τ_p is the particle response time given by:

$$t_p = \frac{4 d_p ?_p}{3 C_d ? \left|\mathbf{u} - \mathbf{v}\right|} \qquad (4.1.14)$$

where d_p is the particle diameter, ρ_p is the particle density, ρ is the fluid density, and C_d is the drag coefficient given by:

$$C_d = \left(\frac{24}{Re_p}\right)\left(1 + 0.15 Re_p^{0.687}\right) \qquad (4.1.15)$$

where Re_p is the particle Reynolds number given by:

$$Re_p = \frac{? \left|\mathbf{u} - \mathbf{v}\right| d_p}{\mu} \qquad (4.1.16)$$

4.2 Numerical Procedure for the Large Eddy Simulations

The numerical method used to solve the equations involves a collocated finite-volume technique. To solve the equations, a fractional-step procedure is used to decouple the continuity and momentum equations. The discretized Navier-Stokes equation may be expressed as the following:

$$\frac{\overline{u}_i^{n+1} - \overline{u}_i^n}{? t} = \frac{3}{2} H_i^n - \frac{1}{2} H_i^{n-1} + \frac{1}{2} \frac{\partial}{\partial x_j} \left[\left(\frac{1}{Re_\tau} + \nu_T \right) \left(\frac{\partial \overline{u}_i^n}{\partial x_j} + \frac{\partial \overline{u}_i^{n+1}}{\partial x_j} \right) \right] - \frac{\partial \overline{P}^{n+1}}{\partial x_i} \qquad (4.2.1)$$

In the first step, an intermediate velocity field $\breve{u}$, which does not satisfy continuity, is calculated by neglecting the pressure gradient terms in the momentum equations. H_i is given by the following:

$$H_i = -\frac{\partial}{\partial x_j}\left(\overline{u}_i \overline{u}_j\right) + \frac{\partial}{\partial x_j}\left(\nu_T \frac{\partial \overline{u}_j}{\partial x_i}\right) + 4\delta_{i3} \qquad (4.2.2)$$

The intermediate velocity field can be found from the following equation:

$$\frac{\breve{u}_i^{n+1} - \overline{u}_i^n}{?t} = \frac{3}{2}H_i^n - \frac{1}{2}H_i^{n-1} + \frac{1}{2}\frac{\partial}{\partial x_j}\left[\left(\frac{1}{Re_\tau} + \nu_T\right)\left(\frac{\partial \overline{u}_i^n}{\partial x_j} + \frac{\partial \overline{u}_i^{n+1}}{\partial x_j}\right)\right] \tag{4.2.3}$$

In the next step, the intermediate velocity field is corrected by solving for the pressure field at the next time step. The correct velocity field $\overline{u}_i^{n+1}$ should satisfy the conservation of mass:

$$\frac{\partial \overline{u}_j^{n+1}}{\partial x_j} = 0 \tag{4.2.4}$$

Subtracting equations (4.2.3) from (4.2.1) gives the following expression:

$$\frac{\overline{u}_i^{n+1} - \breve{u}_i}{?t} = \frac{\partial}{\partial x_j}\left[\left(\frac{1}{Re} + ?_T\right)\frac{\partial \overline{u}_i^{n+1}}{\partial x_j}\right] - \frac{\partial \overline{P}^{n+1}}{\partial x_i} \tag{4.2.5}$$

If the right hand side of equation (4.2.5) is expressed in terms of the gradient of a single scalar quantity Φ:

$$\frac{\overline{u}_i^{n+1} - \breve{u}_i}{?t} = -\frac{\partial F^{n+1}}{\partial x_i} \tag{4.2.6}$$

A Poisson equation for Φ can be obtained by applying the divergence operator to equation (4.2.6) and using equation (4.2.4) to give:

$$\nabla^2 F^{n+1} = \frac{1}{?t}\frac{\partial \breve{u}_j}{\partial x_j} \tag{4.2.7}$$

$$\overline{P}^{n+1} = F - \frac{?t}{2}\left(\frac{1}{Re} + ?_T\right)\nabla^2 F \tag{4.2.8}$$

Equations (4.2.3) and (4.2.7) are solved along with (4.2.6) to obtain the velocity field at the next time step. A Gauss-Siedel iterative solver is used for the momentum equations.

The particle equation of motion is solved using a fourth-order Runge-Kutta scheme. Consider the first-order ODE

$$\frac{dy}{dx} = f(x, y) \tag{4.2.9}$$

The formula for 4th order Runge-Kutta approximation to the above ODE is

$$y_{n+1} = y_n + \frac{h}{6}\left(k_1 + 2\left(k_2 + k_3\right) + k_4\right) + O\left(h^5\right) \tag{4.2.10}$$

where

$$
\begin{aligned}
k_1 &= f(x_n, y_n) \\
k_2 &= f(x_n + \frac{h}{2}, y_n + h\frac{k_1}{2}) \\
k_3 &= f(x_n + \frac{h}{2}, y_n + h\frac{k_2}{2}) \\
k_4 &= f(x_n + h, y_n + hk_3)
\end{aligned}
\qquad (4.2.11)
$$

Collisions are examined first and then the particles are advanced using the Runge-Kutta scheme. Particle deposition is considered to occur when a particle makes contact with a wall. The particle logic has been implemented such that it is consistent with the unstructured domain and periodic directions have been accounted for in the transport logic.

4.3 Particle Collisions

A majority of the numerical simulations of dispersed two-phase flows have been limited to "dilute" suspensions, where interparticle collisions are neglected. The inclusion of interparticle collisions, however, becomes important when the volume fraction of the dispersed phase is $O(10^{-4})$ or greater (Sundaram and Collins 1999; Yamamoto et al. 2001). The particle collision algorithms available in the literature range from a simple yet fast "retroactive" method, that is prone to underestimating number of particle collisions, to an accurate yet computationally intensive "proactive" method (Sundaram and Collins 1996). In the present work, a new collision algorithmthat lies in between the purely retroactive and proactive methods while incorporating the advantages of both methods is developed. The proposed method is more accurate than the purely retroactive method but computationally less intensive compared to the proactive method.

The simplest method to incorporate particle-particle collisions is a purely retroactive method. The retroactive method checks for particle positions at the end of a time step, and if two particles are found to overlap in position, a collision is recorded and the velocities are updated based on the conservation of momentum for the two colliding particles. The advantage of this method is that it is the least computationally intensive of available methods. However, there are disadvantages. Collisions during a time step are missed if two particles collide and completely interpenetrate. It has been shown that such cases can be a significant fraction of the total number of collisions (Sundaram and Collins 1996). The retroactive method remains popular because of computational economy. However, if a significant fraction of collisions is being missed, then it would be necessary to incorporate other methods that can detect the missed collisions.

The most accurate method for detecting collisions is a fully proactive method (Sundaram and Collins 1996). In this method, collisions are detected as follows. An initial list of probable collisions is generated, which contains all colliding pairs based on their trajectories during a given time step. These pairs are then sorted in an ascending order of the time for collision. The earliest collision in the list is carried out, and its time, t_c, is recorded. All particles are then advanced to time t_c, and a new list of collision pairs is generated based upon the updated particle positions and velocities. The earliest collision in the new list is then carried out and a new time t_c is recorded to which the remaining particles are advanced. In this procedure, a colliding particle pair influences the subsequent collisions between other particles. Thus, new collisions which may not occur otherwise can take place and collisions already scheduled in the older list can be removed. This is because a new list is generated after each collision. This

approach is accurate from the viewpoint of purely geometric collisions but the hydrodynamic effects of approaching particles are ignored. The disadvantage of this procedure is that the computational cost can become prohibitive if there are a large number of collisions.

The collision algorithm proposed in this work lies in between the retroactive and proactive methods in terms of accuracy of collision-rate capture and computational work. In a sense, it combines and improves upon the methods adopted in previous works (Yamamoto et al. 2001; Sundaram and Collins 1996; Chen et al. 1998; Hopkins and Louge 1991). In the retroactive method proposed in Chen et al. (1998), the flow domain was divided into slices, but the maintenance of a list of colliding pairs of particles is dispensed with in the interest of computational efficiency. The disadvantages of this approach are that spurious collisions that would never occur in reality may be captured and also, multiple collisions of a single particle within the same time step may be recorded. In the proposed algorithm, both the partition of the flow domain and the maintenance of a particle list are retained. The particle list ensures the accurate order of collisions, which would not be possible otherwise. In addition, spurious multiple collisions of a single particle are also eliminated as the particles that undergo collisions within a time step are removed altogether from the collision list. The current algorithm is also more accurate than the retroactive method since collisions in which particles interpenetrate and crossover are captured. Compared to the proactive method, the current algorithm is computationally less expensive as the list of colliding particle pairs is generated only once and all the collisions in that list are carried out in the ascending order of their collision time with the exception of those that involve particles that have already undergone collisions in earlier pairs. Thus, we save considerable computational time when compared to the proactive method but attain improved accuracy with respect to the retroactive method. Next, the details of the algorithm are presented. For completeness, some of the details which are available in the above references will be repeated.

We consider only binary collisions in this work. Consider two particles as shown in Fig. 4.3.1. It is assumed that the particles have constant velocity during the time step, so the effect of collisions becomes a purely geometric consideration once the initial particle positions and velocities are known. Let us consider the reference frame, x'-y', whose origin is fixed on one of the two potentially colliding particles, P_2. The relative velocity and position vectors of the two particles, $\mathbf{w}_n$ and $\mathbf{r}_n$, are given as:

$$\mathbf{w}_n = \mathbf{V}_{1n} - \mathbf{V}_{2n} \tag{4.3.1}$$

$$\mathbf{r}_n = \mathbf{X}_{1n} - \mathbf{X}_{2n} \tag{4.3.2}$$

where $\mathbf{V}_{1n}$, $\mathbf{V}_{2n}$ and $\mathbf{X}_{1n}$, $\mathbf{X}_{2n}$ are the velocities and positions respectively of particles P_1 and P_2 in the laboratory reference frame at the end of the n^{th} time step. The vectors $\mathbf{w}_n$ and $\mathbf{r}_n$, whose magnitudes are denoted by w_n and r_n respectively, define the plane that the y'-axis lies in.

As shown in Fig. 4.3.1, the closest possible approach distance, s_m, between the centers of the two particles can be easily expressed as

$$s_m = r_n \sin\theta \tag{4.3.3}$$

where the angle θ can be found from:

$$? = p - \cos^{-1}\left(\frac{\mathbf{r}_n \cdot \mathbf{w}_n}{r_n w_n}\right) \qquad (4.3.4)^{\P}$$

The instance of closest approach, t_m, can be given by

$$t_m = t_n + \frac{r_n \cos ?}{w_n} \qquad (4.3.5)$$

where t_n is the time at the end of the n^{th} time step.

The time of closest approach does not necessarily fall within the current time step. One must check for two factors: first, that t_m falls within the current time step, and second, that the minimum distance s_m is such that the particles just touch. The first constraint, i.e. $t_m < t_n + \Delta t$, is strict only for point masses. For particles of finite diameter, t_m may exceed $(t_n + \Delta t)$, due to particle overlap, and they may still collide within the current time step. Hence, the distance constraint can be expressed as

$$s_m \le \frac{d_1 + d_2}{2} \qquad (4.3.6)$$

where d_1 and d_2 are the diameters of particles P_1 and P_2. The relative position vector as a function of time is given as

$$\mathbf{r}(t) = \mathbf{r}_n + (t - t_n)\mathbf{w}_n \qquad (4.3.7)$$

whose magnitude can be expressed as

$$r(t) = \sqrt{r_n^2 + 2(\mathbf{r}_n \cdot \mathbf{w}_n)(t - t_n) + w_n^2 (t - t_n)^2} \qquad (4.3.8)$$

To find the time at which the minimum distance occurs, we have

$$\frac{dr(t)}{dt} = 0 \quad \text{at } t = t_m \qquad (4.3.9)$$

This leads to the following equation

$$t_m = t_n - \frac{\mathbf{r}_n \cdot \mathbf{w}_n}{w_n^2} \qquad (4.3.10)$$

The minimum separation is then given as

$$s_m = r(t_m) \qquad (4.3.11)$$

The time of contact, t_c, needs to be found, since t_m can exceed t_c if the particles are overlapping. To find the time of contact, t_c, the following equation is used

$$r(t_c) - d_{12} = 0 \qquad (4.3.12)$$

where $d_{12} = (d_1 + d_2)/2$.

¶ Note that this equation is incorrectly stated in Chen et al. (1998) as $\theta = \cos^{-1}\left(\frac{\mathbf{r}_n \cdot \mathbf{w}_n}{r_n w_n}\right)$

This equation has two roots, given by

$$t_c = t_n - \frac{\mathbf{r}_n \cdot \mathbf{w}_n}{w_n^2}\left(1 \pm \sqrt{1 - K_n}\right) \tag{4.3.13}$$

where

$$K_n = \frac{r_n^2 w_n^2}{(\mathbf{r}_n \cdot \mathbf{w}_n)^2}\left(1 - \frac{d_{12}^2}{r_n^2}\right) \tag{4.3.14}$$

As mentioned in Chen et al. (1998), for colliding particles, both roots of equation (4.3.13) must be real which can be shown by considering the following equation

$$(\mathbf{r}_n \cdot \mathbf{w}_n)^2 - w_n^2 r_n^2 + w_n^2 d_{12}^2 = w_n^2 (d_{12}^2 - r_n^2 \sin^2 ?) \tag{4.3.15}$$

The right hand side of (4.3.15) must be positive for a collision to take place. Therefore, both roots of (4.3.13) must be real. It is obvious which root to choose when (4.3.13) is rewritten as the following

$$t_c = t_m \pm \frac{\mathbf{r}_n \cdot \mathbf{w}_n}{w_n^2}\sqrt{1 - K_n} \tag{4.3.16}$$

In general, $t_c < t_m$. The plus sign in (4.3.16) is chosen to account for this fact, since $\mathbf{r}_n \cdot \mathbf{w}_n \le 0$ necessarily for colliding particles. The particle positions are then updated using the following equation

$$\mathbf{X}_c = \mathbf{X}_n + (t_c - t_n)\mathbf{V}_n \tag{4.3.17}$$

The post collision properties can be computed by applying the law of conservation of momentum for the two colliding particles as follows:

$$m_1 \mathbf{V}_{1i} + m_2 \mathbf{V}_{2i} = m_1 \mathbf{V}_{1f} + m_2 \mathbf{V}_{2f} \tag{4.3.18}$$

where the subscripts “i” and “f” denote the velocities before and after the collision, respectively. Let **P** denote the impulse of collision exerted by particle 2 on particle 1:

$$\mathbf{P} = m(\mathbf{V}_{1f} - \mathbf{V}_{1i}) = -m(\mathbf{V}_{2f} - \mathbf{V}_{2i}) \tag{4.3.19}$$

It has been assumed that particles 1 and 2 have identical mass. If e is defined as the coefficient of restitution (perfectly elastic collisions, e = 1, are assumed in this work), **P** can be obtained by examining the incomplete restitution of the normal component of the relative velocity using the following equation at the instant of collision:

$$\mathbf{w}_{nf} \cdot \left(\frac{\mathbf{r}_n}{r_n}\right) = -e\mathbf{w}_{ni} \cdot \left(\frac{\mathbf{r}_n}{r_n}\right) \tag{4.3.20}$$

By using (4.3.19) and (4.3.20), along with the definition of the relative velocity, it follows that:

$$\mathbf{P} = -(m/2)(1+e)\left(\mathbf{w}_n \cdot \left(\frac{\mathbf{r}_n}{r_n}\right)\right)\left(\frac{\mathbf{r}_n}{r_n}\right) \tag{4.3.21}$$

The velocities of particles 1 and 2 are now calculated with (4.3.19).

The above method describes how to account for the collision of two particles. However, in a system with potentially multiple collisions, an algorithm is required to determine which collisions actually occur under the temporal and spatial constraints imposed by the problem. As mentioned before, there are several ways to do this. The simplest is to use a purely retroactive method (Yamamoto et al. 2001; Sundaram and Collins 1996) which saves CPU time but can underestimate the number of collisions by as much as twenty percent. A fully proactive method (Sundaram and Collins 1996) will accurately (from a geometric standpoint) capture all collisions, but is often computationally expensive since the collision algorithm is inherently an $O(N_p^2)$ operation, where N_p is the number of particles in the domain. The approach described in this work aims to capture the collisions missed by a purely retroactive method at a computational cost smaller than the proactive method and also to eliminate spurious multiple collisions of a particle in a given time step.

The current method is as follows. First, all the initial particle positions and velocities are determined. The flow domain is then partitioned into sections in which collisions will be considered. The size of the partitions is selected to be large enough to capture all likely collisions, yet small enough to reduce the search operation for colliding pairs. Chen et al. (1998) provide a criterion on the partition widths which says that they should be greater than twice the maximum distance two particles, in that partition, travel relative to each other over a given time step. In our calculations, the flow domain is partitioned into $16 \times 16 \times 16$ uniform sections. A partition includes several grid nodes in each direction and satisfies the above criterion. In a given partition, all collision pairs are identified using equations (4.3.1)-(4.3.16). Next, the pairs are ordered by their time of contact. The first collision in the ordered list (say, between particles p and q) for the partition is carried out by advancing the particles p and q to their point of impact by using the velocities at the n^{th} time step. The post collision properties are found as outlined above in equations (4.3.17)-(4.3.21), and then the particle pair is advanced for the remainder of the time step. The collision list is then modified as follows: any future collision pair that contains particles p or q is not allowed to occur in the current time step. By removing particles p and q from future collisions in the given time step, any erroneous multiple collisions of a particle within the same time step are eliminated. The next pair in the list is then allowed to collide, and they are then removed from future collisions within the current time step. This process is repeated until there are no more particles left in the collision list. The inclusion of this collision algorithm required approximately two and a half times more CPU time than a simulation without collisions. This approach in treating collisions represents an improvement over the purely retroactive method. For example, consider the manner in which the retroactive algorithm detects collisions. Typically, only particle overlap at the end of a time step is used as the criterion for collision. Thus, if three particles are overlapping, three collision pairs are identified and carried out without regard to which pair actually collided first. Clearly, this is not physical.

4.4 Validation of the Scheme

Validation of the scheme was accomplished through channel flow simulations. Periodic flow in a channel of dimensions $4\pi\delta$ x 2δ x $2\pi\delta$ in the streamwise, wall-normal and spanwise directions, respectively, was carried out for Re_τ = 180 and 590, based on friction velocity and channel half-height. The results were compared to the work of Kim, Moin, and Moser (1987) and Moser, Kim, and Mansour (1999), respectively. Several subgrid models were evaluated. The models used include the dynamic subgrid kinetic energy model (Kim and Menon 1997), the static

coefficient subgrid kinetic energy model (Horiuti 1985) with a wall-damping function, and the so-called "no model" LES whereby the simulation is functioning as a coarse grid DNS. The grid used was 100x100x50 in the streamwise, wall-normal and spanwise directions, respectively. The same grid was used for both Reynolds numbers. A 2.5% geometric progression stretch is applied to the grid in the wall-normal direction. Due to the difference between the formulations of the dynamic model and the static model, the grid spacing does not work out to be the same. In the dynamic model, a coarse grid is generated which has half the number of nodes in each direction when compared to the fine grid. The stretching is applied to the coarse grid. The fine grid is generated by dividing each coarse grid cell into 8 equal fine grid cells. Although the total number of nodes is the same for all channel flow simulations, the manner in which the dynamic model operates lends itself to a slightly different grid structure. Since no stretching is applied to the streamwise and spanwise directions, the spacing is the same in these directions regardless of the model. Only the wall-direction is altered. If one applies no grid stretching (as was done in some simulations reported in this code validation section), the dynamic model formulation used in this work will naturally lend itself to a uniform grid. See Fig. 4.4.1 for a two-dimensional schematic of the dynamic model grid logic.

4.4.1 Channel Flow, $Re_\tau = 180$ Results

The first simulations were done at $Re_\tau = 180$ and compared to Kim, Moin, and Moser (1987). The statistics are averaged in time and the homogeneous directions. As a general rule, statistics were averaged for 10 time units. Longer averaging times had little or no effect on changing the statistics. The mean velocity profiles are shown in Fig. 4.4.1.1. Four cases are compared to the DNS data: the no-model, the Horiuti model, the dynamic k model on a uniform grid, and the dynamic model on a stretched grid. In the near-wall region, all the cases compare well with the DNS data, with the Horiuti and no-model runs coming closest to matching the near-wall data. Near the channel centerline, all models over predict the DNS data. The Horiuti model is seen to overpredict the DNS by more than 10%, with the dynamic model on a stretched grid only overpredicting the DNS by less than 2%.

In reporting the rms predictions of the various models, two values are reported for each of the kinetic energy subgrid models. The resolved rms value is the value computed directly from the velocity fluctuations. The total rms reported adds the subgrid fluctuation isotropically to the resolved quantity. This equates to adding $\sqrt{\frac{2}{3}k_{sgs}}$ to each rms quantity. This gives a "true" measure of the total fluctuations since the resolved and subgrid scales are being taken into account and should represent the DNS data better. However, it will be seen that this is not necessarily the case.

The streamwise rms results are shown in Fig. 4.4.1.2. It is clear that the resolved urms predicted by the dynamic k model on a stretched grid best predicts the DNS data, followed closely by the no-model case. However, once the subgrid fluctuations are added, the models are overpredicting the DNS by as much as 30% at the peak of the profile. This means that the models are predicting excessive subgrid energy. It should be noted that all finite-volume top-hat filter LES results are grid dependent. One can easily improve the results by increasing the grid resolution and eventually one will approach the DNS solution. However, this is not practical and one must choose a grid resolution much coarser than the DNS simulation.

The wall-normal rms results show in Fig. 4.4.1.3 that the no-model case best predicts the DNS data. Both the resolved rms values from the k models underpredict the DNS data, as they should since it is the total rms value which should compare well with the DNS data. However, once the subgrid fluctuations are added, it is seen that the models overshoot the DNS by roughly 35% at the peak of the profile. The lack of smoothness in the total rms velocity predicted by the dynamic model is a result of its prediction of the sgs k, which is non-smooth near the wall. This is due to the method in which the grid is created, as two daughter cells of a coarse grid cell will have the same size, therefore no grid stretching between daughter cells, which decreases the resolution near the wall and thus decreases the performance of the model. Ideally, one would generate a stretch for the fine grid cells which perfectly coincides with the coarse grid. However, this is prohibitive especially for complex geometries.

The spanwise rms velocity is shown in Fig. 4.4.1.4. It is seen that both k models' resolved quantities underpredict the DNS data as they should. However, the total rms values overpredict the DNS data by roughly 33% near the peak of the profile. The no-model case also overpredicts the DNS, but to a lesser degree of approximately 20%.

The Reynold's stress term $u'v'$ is shown in Fig. 4.4.1.5. It is seen that the no-model case best predicts the DNS data, followed closely by the Horiuti model. The dynamic k model underpredicts the maximum magnitude of the term by roughly 28%.

The value of the subgrid kinetic energy predicted by each model is shown in Fig. 4.4.1.6. It is clear that the dynamic model predicts roughly twice as much sgs k as the Horiuti model. The non-smooth near wall behavior of the dynamic model's prediction for the sgs k has already been explained. The sgs k correctly goes to zero near the wall for both models.

The turbulent eddy viscosity predicted by the dynamic model on a stretched grid is shown in Fig. 4.4.1.7. The jagged nature of this viscosity is due to the nature of the grid used in the dynamic model formulation, as each daughter cell of a coarse grid cell are assigned the same constants for the production and dissipation terms, respectively. In reality, there is no physical reason why two daughter cells should have the same values for the constants since the flowfield is different at these different locations. However, this issue is once again argued by claiming that the difference is negligible as the grid is refined and the two daughter cells approach each other in space.

The value of the coefficient for the production term in the dynamic model is shown in Fig. 4.4.1.8. It is seen that the advantage of the dynamic model is that no wall model is needed to generate correct near-wall behavior of the coefficient. The model automatically damps the production term at the wall. This is a tremendous advantage when the square duct geometry is considered later, as the wall models are unknown for the square duct geometry, and poorly understood even for simple geometries like channels. Horiuti's model claims this coefficient is a constant 0.05, which is roughly the mean value given by the dynamic model. So it is clear that the dynamic model is behaving as expected. The coefficient for the dissipation term in the dynamic model is shown in Fig. 4.4.1.9. The constant coefficient models suggest a value of 1 to 1.5, which falls within the range given by the dynamic model.

4.4.2 Channel Flow, $Re_\tau = 590$ Results

The grid is held fixed and the Reynolds number is increased to 590 for the next comparisons. The DNS data by Moser, Kim, and Mansour (1999) is used as the baseline for comparison. When examining the mean velocity profile, shown in Fig. 4.4.2.1, it is clear that the Horituti model better predicts the DNS data. However, the qualitative trends, such as inflection points, in the DNS profile are not captured at this Reynolds number. The dynamic model captures the near wall region better than the Horituti model, yet near the centerline the dynamic model overpredicts the DNS data by roughly 20%.

The streamwise rms velocity profiles are shown in Fig. 4.4.2.2. It is seen that none of the simulations capture the location of the peak or the magnitude of urms accurately. Once the subgrid fluctuations are added, the dynamic model overpredicts the rms velocity by roughly 100%. The Reynolds number is clearly much too large to be simulated by only 0.5 million nodes in this LES.

The wall-normal rms velocity profiles are shown in Fig. 4.4.2.3. A more positive outcome may be seen in this plot. The k models correctly underpredict the DNS data when the resolved rms quantity is considered. By adding the subgrid fluctuation, the peak shifts closer to the location of the peak in the DNS data, however, the magnitude is then overpredicted by 30% and 80% for the Horiuti and dynamic k models, respectively.

The spanwise rms velocity profiles are shown in Fig. 4.4.2.4. The Horiuti model correctly underpredicts the DNS data when the resolved rms velocity is considered. All other forms of the rms velocity overpredict the DNS data, with the dynamic k model overpredicting the peak by roughly 100%.

The Reynold's stress term $\overline{u'v'}$ is shown in Fig. 4.4.2.5. The dynamic k model predicts the DNS data the closest. The Horiuti model underpredicts the maximum magnitude of the term as well as gives the peak farther from the wall compared to both the DNS and dynamic k model.

The value of the subgrid kinetic energy predicted by each model is shown in Fig. 4.4.2.6. It is clear that the dynamic model predicts roughly twice as much sgs k as the Horiuti model. The non-smooth near wall behavior of the dynamic model's prediction for the sgs k has already been explained. The sgs k correctly goes to zero near the wall for both models.

The turbulent eddy viscosity predicted by the dynamic model on a stretched grid is shown in Fig. 4.4.2.7. The jagged nature of this viscosity is due to the nature of the grid used in the dynamic model formulation, as explained before. However, as the grid is refined, this trend decreases. Also, the eddy viscosity in a mean sense never appears in the calculation. Only the instantaneous values enter into the momentum equation.

The value of the coefficient for the production term in the dynamic model is shown in Fig. 4.4.2.8. It is seen that the advantage of the dynamic model is that no wall model is needed to generate correct near-wall behavior of the coefficient. The model automatically damps the production term at the wall. This is an advantage when the square duct geometry is considered later, as the wall models are unknown for the square duct geometry, and poorly understood even for simple geometries like channels. Horiuti's model claims this coefficient to be a constant of 0.05, which is roughly the mean value given by the dynamic model. So it is clear that the dynamic model is behaving as expected. The coefficient for the dissipation term in the dynamic model is shown in Fig. 4.4.2.9. The constant coefficient models suggest a value of 1 to 1.5, which falls within the range given by the dynamic model. It is interesting to note that both constants have decreased in magnitude when compared to the $Re_\tau = 180$ case.

4.4.3 Summary of Code Validation

It has been shown that LES can be an accurate tool in turbulence simulations if careful consideration is given to the grid, the subgrid model, and the Reynolds number. Since particle transport will be a major part of this thesis, the added information of the subgrid energy will be valuable in predicting accurate particle trajectories which is why the dynamic k model is chosen over the so-called "no-model" LES. The Horiuti model is not considered an accurate choice for the square duct since it requires a wall-damping function, which not known precisely for the square duct.

Chapter 5. Preferential Concentration Results

The governing equations were solved on an 80×80×128 grid with 2.5 geometric progression grid stretching in the two wall directions. The flow domain was $\delta \times \delta \times 2\pi\delta$. The grid distributions in the x and y directions (the two wall directions) were identical. The simulation was performed at a Reynolds number of 360, based on average friction velocity and duct width. The minimum and maximum grid spacings in the wall directions were 3.5232 and 5.6324 wall units, respectively. The first node away from the wall was at 1.7616 wall units. The streamwise grid spacing was held fixed at 17.6714 wall units. See Table 5.1 for complete grid information in the cross-section. The grid is symmetric about the mid-plane. The dimensionless time step was 0.0001.

The choice of initial conditions does not influence the final solution, although it has an effect on the length of integration time needed to reach a stationary state. A restart file from a single phase square duct simulation was used as the initial conditions for this study. That restart file was generated after applying an initial divergence free perturbation to a parabolic velocity profile. The simulation utilized just under 1 GB of memory. The vast majority of CPU time on the fluid calculation was spent on the multigrid solver for the pressure Possion equation.

The fluid flow calculation was compared to the DNS data of Madabhushi (1993), who studied flow at Re_τ = 260, and to LES data of Madabhushi and Vanka (1991), who studied flow at Re_τ = 360. Good agreement is seen in Fig. 5.0.1 where the mean streamwise velocity at the wall bisector is compared to past studies. Mean fluid statistics were averaged for more than 60 time units. This unusually long averaging time was necessary to achieve symmetry in contours of fluid statistics since the square duct has only one homogeneous direction to average across.

In the cross-section of a square duct, one may identify different regions of flow patterns. We have chosen four such locations in this work, all identifiable from a time-mean sense (see Fig. 5.0.2). Due to the finite resolution of the grid, the nearest node to each desired location was chosen. The locations are as follows: the center of the duct where the secondary flows are minimal (x^+=177.2, y^+=177.2), the near-wall region (x^+=177.2, y^+=19.8), the center of the time-mean secondary flow vortices (x^+=76.7, y^+=31.2), and the saddle region between the secondary flow vortices (x^+=59.5, y^+=59.5). An area of 20.25 square wall units about each point was used to collect particle statistics. Note that these locations are only significant in a time-mean sense, and are used only for the preferential concentration portion of this dissertation. These locations are also arbitrary, no significant meaning is associated with the coordinates of any points other than convenience.

To obtain the PDFs, the fluid statistic is interpolated to the particle positions, then averaged in time and over the number of particles sampled in the thin tube in the streamwise direction for a given cross-sectional location. This gives a conditional PDF of the fluid statistic since the quantity is only sampled at particle positions in the thin streamwise tube. The fluid PDF is averaged over all grid points within the thin tube. Only three values of τ_p^+ are shown for clarity in the PDFs (τ_p^+ = 0.25, 1, and 8), along with the PDF of the (unladen) fluid statistic. The mean values of the statistics shown were obtained in a similar fashion. See Table 5.2 for the particle parameters studied for the preferential concentration simulations.

For each different response time, trajectories of 200,000 particles are computed. Elastic collisions with the wall are assumed. The particles are initially randomly positioned in the domain with initial velocities equal to the

local fluid velocity and are evolved for at least 10 particle response times (based on the largest τ_p) to allow the particles to lose any initial inertial effects. Statistics are then averaged for at least 19 particle response times (statistics were averaged over 604 particle response times for the smallest particles). Statistics were averaged in the homogeneous direction as well as in symmetric planes in the cross section when appropriate. Since it is only by chance that a particle is located at a fluid grid point, second order Lagrange polynomials were used to interpolate the fluid quantities to a particle position. This involved 27 fluid quantities (such as u, v, w and k_{sgs}) surrounding the particle.

In order to visually display the preferential concentration of particles, a different series of simulations were conducted where 100,000 particles per response time were distributed randomly in a thin volume defined by $7.05 \leq y^+ \leq 10.66$. The particle equation of motion was then integrated for 2.7 particle response times for $\tau_p^+ = 8$, and 86.4 particle response times for $\tau_p^+ = 0.25$, where τ_p^+ is the particle response time in wall units and is also a Stokes number. Scatter plots of instantaneous particle positions were then generated.

5.1 Visualization of Preferential Concentration in a Near-Wall Plane

In this section, we present the particle scatter plots along with near wall contours of fluid statistics to visually illustrate the preferential concentration phenomenon. Following this illustration, we present variation of $\langle\omega\rangle$, $\langle\lambda_i\rangle$, $\langle\sigma_u\rangle$, and $\langle\nabla\mathbf{u}:\nabla\mathbf{u}\rangle$, and their probability distribution functions with τ_p^+ and cross-sectional location. The notation "$\langle\rangle$" denotes averaging in the homogeneous direction, time and appropriate symmetric cross-sectional points.

For clarification, the meaning of the above statistics will be mentioned again in this section. The swirling strength, λ_i, which is the magnitude of the imaginary part of the complex conjugate eigenvalue pair of the fluid velocity gradient tensor, has been used to identify vortices (Zhou et al. 1998; Adrian, Balachandar, and Liu 2001). The swirling strength is zero at locations where the eigenvalues of $\nabla\mathbf{u}$ are all real. A positive value of λ_i corresponds to a local dominance of rotation-rate over strain-rate (Adrian et al. 2001). Vorticity can arise from either swirling or shear. However, it is the swirl that has a greater centrifugal effect on particles than shear and hence swirling strength is a better choice than vorticity for preferential concentration studies. The maximum strain, σ_u, is the minimal eigenvalue of the strain-rate tensor. To fully appreciate the meaning of $\nabla\mathbf{u}:\nabla\mathbf{u}$, one must examine its derivation. Consider an Eulerian formulation of the particle velocity field. To first order, if one neglects body forces, the particle velocity field, $\mathbf{u}_p$, may be expressed as a function of the fluid velocity field, $\mathbf{u}$, and particle response time, t_p, as follows

$$\mathbf{u}_p = \mathbf{u} - t_p\left(\frac{\partial \mathbf{u}}{\partial t} + \mathbf{u}\cdot\nabla\mathbf{u}\right) \tag{5.1.1}$$

Maxey (1987) has shown that this particle velocity field is not divergence free. Taking the divergence of (5.1.1) gives

$$\nabla\cdot\mathbf{u}_p = -t_p\frac{\partial u_j}{\partial x_i}\frac{\partial u_i}{\partial x_j} = -t_p\nabla\mathbf{u}:\nabla\mathbf{u} \tag{5.1.2}$$

It is clear from (5.1.2) that particles will accumulate where $\nabla\mathbf{u}:\nabla\mathbf{u}$ is positive.

To study preferential concentration in experiments, typically one would take a snapshot of particle positions and overlay the velocity vector plots obtained from, say, particle image velocimetry (PIV). One can do similar studies using computations, although doing so in the cross-section of the square duct provides little information unless very high volume fractions are studied so that one may clearly identify patterns in the scatter plots. For one-way coupling studies, typically the volume fraction is low, so taking a cross-sectional snapshot reveals little information due to the small sample size of particles in a given cross-section. Another approach is to place a large number of particles in a selected region and evolve the particles for a few particle response times, and observe their locations with respect to local fluid statistics. By placing particles in a plane parallel to the wall, the number of particles in the plane will remain relatively constant over a few response times, allowing more definite conclusions to be made on preferential concentration at near-wall turbulent structures. This approach was used for three particle Stokes numbers in this work ($\tau_p^+ = 0.25$, 1, and 8). Since this is the first work on particle transport in a square duct, the results of the simulations in this section are intended to first give the reader an understanding of the nature of particle dispersion in a square duct before moving on to more sophisticated methods of measuring the preferential concentration.

To visually demonstrate the preferential concentration of particles in a square duct, scatter plots of particle positions along with instantaneous contours of streamwise velocity, vorticity magnitude, swirling strength, strain-rate, and $\nabla\mathbf{u}:\nabla\mathbf{u}$ are shown in Figs. 5.1.1-5.1.8. Although only qualitative, clear trends may be observed by comparing the contour plots of the above statistics to the particle scatter plots. The particle scatter plots for a square duct are seen to be more complex than what other researchers have shown for channel flow (Zhang and Ahmadi 2000). The secondary flows, especially those near the corners, attenuate the streaky chains of particles reported in the case of a channel flow. In a square duct, patches of particles along with chains are formed and aligned preferentially with the surrounding fluid statistics.

Low speed streaks are known to contain locally high concentrations of particles (Wang and Squires 1996b). By comparing Fig. 5.1.4 to the scatter plots, we see that there is strong correlation between the low speed streaks and particle positions. Uniquely shaped "holes" in the particle scatter plots align remarkably well with the patches of high speed streamwise flow. The trend is most obvious for $\tau_p^+ = 1$, which will be shown later to be near the Stokes number which obtains maximum preferential concentration. When examining the contours of vorticity magnitude, ω, shown in Fig. 5.1.5, it is clear that there is a correlation between vorticity and particle location. The contours of swirling strength, shown in Fig. 5.1.6, are more difficult to correlate to the scatter plots with visual inspection alone. The same can be said of the contours of s_u and $\nabla\mathbf{u}:\nabla\mathbf{u}$, shown in Figs. 5.1.7 and 5.1.8, respectively. Statistical methods are clearly required to obtain any conclusions about preferential concentration trends using the above fluid statistics. However, it is beneficial to see the complex nature of these structures before moving on to statistical analysis of these quantities.

Being the first study to display statistics such as λ_i, s_u, and $\nabla\mathbf{u}:\nabla\mathbf{u}$ in a square duct, it is insightful to display contours of these statistics in several near wall planes to qualify how these statistics behave throughout the

duct. Instantaneous contours are presented for y^+ = 1.76, 35.09, and 177.18, in Figs. 5.1.9-5.1.11 for λ_i, s_u, and $\nabla\mathbf{u}:\nabla\mathbf{u}$, respectively. The cross-sectional contours of the same statistics are shown in Figs. 5.1.12-5.1.14.

5.2 Effect of vorticity magnitude

It has been shown by previous researchers that particles accumulate in regions of low vorticity (Squires and Eaton 1991b). Typically, when it is stated that particles collect in low vorticity regions, the conclusion is drawn upon evidence from simulations of flows with little or no time-mean shear, such as isotropic turbulence. However, vorticity can arise from either rotation or shear. Consider laminar plane Couette flow. This flow has no rotational aspect, yet exhibits vorticity due to the shear stress at the walls. It is typically thought that only the rotational aspect of vorticity lends itself to the preferential concentration of particles. Near walls, where vorticity is high due to shear, it is not likely that vorticity remains a strong measure of preferential concentration. Enstrophy, which is the square of the vorticity, would be similarly misinterpreted near a wall. It is for this reason that the swirling strength, $\langle\lambda_i\rangle$, is a good measure of preferential concentration rather than vorticity. To corroborate this statement, the vorticity magnitude will now be examined to demonstrate that near a wall, the vorticity (and hence enstrophy) is not a good measure of preferential concentration of particles in flows with high shear.

Due to the large variation of vorticity magnitude in the duct cross-section, it is necessary to use a separate plot for each location to clearly see the trends. In the near wall region (Fig. 5.2.1) small particles align themselves closely with the low vorticity regions, which are located between vortical structures near the wall. As τ_p^+ increases, the value of $\langle\omega\rangle$ at the particle positions also increases at this location. Note that in the near wall region, the levels of vorticity are highest when compared with other locations. The vortex center region, shown in Fig. 5.2.2, also indicates that small particles align themselves most closely with low vorticity regions. Again, as τ_p^+ increases, the value of $\langle\omega\rangle$ at the particle positions is seen to increase. This indicates that large particles accumulate in regions of high vorticity also for the vortex center location. Upon examining the saddle region in Fig. 5.2.3, we see that particles with τ_p^+= 1 experience the lowest local vorticity. Note however, the total variation in $\langle\omega\rangle$ in the saddle region is roughly an order of magnitude smaller than the value closer to the wall. At the duct center region, the variation in vorticity is small, hence the trend is not clear (Fig. 5.2.4). This is expected since the duct center is a region of low vorticity and vortical structures are not dominant here.

Upon examining the PDF of vorticity magnitude at the near wall location, shown in Fig. 5.2.5, it is seen that, in contrast to observations in isotropic turbulence, larger particles do indeed collect in regions of high vorticity. The PDFs of the smaller particles are shifted to values of lower vorticity than the fluid PDF, indicating that the small particles are accumulating preferentially in low vorticity regions. At the vortex center region, shown in Fig. 5.2.6, it is again seen that large particles are able to accumulate in locations of high $\langle\omega\rangle$. Smaller particles are again found to align themselves with low vorticity regions at this location. In the saddle region in Fig. 5.2.7, we see that all particles are collecting in regions of low vorticity regardless of Stokes number. This is also true in the duct center region, seen in Fig. 5.2.8. The duct center will behave more like isotropic turbulence due to the relatively large distance from the walls compared to other locations, and hence at the duct center we see the trends confirming what others have found in isotropic turbulence – that particles collect in regions of low vorticity. However, this statement

clearly does not hold true near a wall. Therefore, for regions of flow which experience strong shear, vorticity is not an appropriate measure of preferential concentration of particles. This was clearly shown by examining the PDFs of the vorticity for large particles in the near wall region.

5.3 Effect of swirling strength

Since the swirling strength is a measure of vorticity, it is expected that particles will accumulate in regions of low swirling strength. Ferry and Balachandar (2001) have verified this in channel flow. Unlike $\langle\omega\rangle$, $\langle\lambda_{ci}\rangle$ accounts only for regions of vorticity which have the nature of a core (Adrian et al. 2001). Therefore, it is expected that $\langle\lambda_{ci}\rangle$ be a more appropriate measure of preferential concentration in areas of flow which contain distributed shear. It is of interest to know how preferential concentration varies with swirling strength in the cross-section of a square duct. Shown in Fig. 5.3.1 is the variation of $\langle\lambda_{ci}\rangle$ with τ_p^+ and the cross-sectional location. It is seen that for the near wall and vortex center locations, as τ_p^+ increases particles accumulate in regions of decreasing $\langle\lambda_{ci}\rangle$ before passing through a minimum, after which the trend is reversed. This minimum occurs at $\tau_p^+ = 4$. These trends in the mean values agree with the trends found in channel flow by Ferry and Balachandar (2001). Due to the coherent vortical structures found in the near wall region where turbulence is generated, it is seen that this area contains particles experiencing the highest levels of swirling strength. As the distance from the wall increases, the swirling strength becomes small. For the saddle region, it is seen that the trend in $\langle\lambda_{ci}\rangle$ with τ_p^+ is less apparent. At the duct center, we see little variation in the swirling strength with τ_p^+.

By examining the PDFs of swirling strength for the various locations, we can expand upon the trends seen in the plots of the mean values. In the near wall region, we can see in Fig. 5.3.2 that particles indeed accumulate in regions of low swirling strength, with the trend more pronounced for large particles. As in the previous PDFs, only three particle Stokes numbers are shown for clarity. Unlike the PDFs of vorticity near the wall in the previous section, we see particles aligning themselves with low $\langle\lambda_{ci}\rangle$ for all particle Stokes numbers. This trend confirms earlier statements that the swirling strength, not vorticity, is the more appropriate measure of preferential concentration when considering rotational aspects of the fluid. At the vortex center location, shown in Fig. 5.3.3, particles are clearly seen to accumulate in regions of low $\langle\lambda_{ci}\rangle$, with identical trends as shown in Fig. 5.3.2 at the near wall location. As the distance from the wall increases, the saddle region, shown in Fig. 5.3.4, still displays the same trend of particles accumulating in regions of low $\langle\lambda_{ci}\rangle$, but to a lesser degree. Also, as the location is moved further from the wall to the saddle region, the influence of τ_p^+ on the PDFs is relatively weak. In the center of the duct, shown in Fig. 5.3.5, the particles tend to more closely match the fluid PDF with only slight preferential concentration of large particles. This suggests that the distance from the wall has a significant influence on the degree of preferential concentration of particles. Due to the consistent trends seen in the PDFs of λ_{ci}, we can state that λ_{ci} is a more appropriate choice than vorticity for studies of preferential concentration.

5.4 Effect of strain-rate

It has been shown by previous researchers that particle collect in regions of high strain-rate (Squires and Eaton 1991b). Ferry and Balachandar (2001) have shown that σ_u is a good measure of preferential concentration in channel flow. Shown in Fig. 5.4.1 is the variation of $\langle\sigma_u\rangle$ with τ_p^+ and the cross-sectional location. It is seen that

for the near-wall, vortex center and saddle locations, as τ_p^+ increases particles accumulate in regions of increasingly negative $\langle \sigma_u \rangle$ (which indicates compressional strain) before passing through a maximum compressional strain, after which this trend is reversed. This maximum occurs within the range $2 \le \tau_p^+ \le 4$. From the mean values, it can be seen that particles in the vortex center region accumulate in areas of fluid with the highest strain-rate of the locations sampled. The particle Stokes number in the vortex center region which aligns itself with the highest magnitude of $\langle \sigma_u \rangle$ is $\tau_p^+ = 4$. However, in the near wall region, which experiences the least strain of the locations sampled, the particle Stokes number which experiences the highest local strain-rate is $\tau_p^+ = 2$. The saddle region also indicates that particles with $\tau_p^+ = 2$ align themselves with the highest magnitude of local strain-rate. This suggests that the preferential concentration is not only a function of distance from the wall, but also a function of τ_p^+. In the duct center, no clear trend can be seen.

By examining the PDFs of $\langle \sigma_u \rangle$, it can be seen that particles tend to collect in regions of higher compressional strain (negative strain) when compared to the fluid PDF. For the near wall region, shown in Fig. 5.4.2, particles clearly align themselves along areas of higher compressional strain. This trend is more apparent for larger Stokes numbers. This is also the case in the vortex center region, shown in Fig. 5.4.3. Particles with small Stokes numbers are seen to exhibit less departure from the fluid PDF, indicating that small particles are dispersed more than large particles. However, for the saddle region, shown in Fig. 5.4.4, this trend is less apparent. Particles are still seen to move towards areas of high compressional strain, but to a lesser degree. In the duct center, displayed in Fig. 5.4.5, the trend is much less pronounced and no definite conclusion may be made for this location.

5.5 Effect of $\tilde{N}\mathbf{u}:\tilde{N}\mathbf{u}$

The final quantity we examine is $\nabla\mathbf{u}:\nabla\mathbf{u}$, which can also be expressed as $|\mathbf{S}|^2 - |\mathbf{O}|^2$, where $\mathbf{S}$ and $\mathbf{O}$ are the strain-rate and rotational components of the velocity gradient tensor, respectively. As mentioned earlier, positive values of $\nabla\mathbf{u}:\nabla\mathbf{u}$ indicate an accumulation of particles at a location. Shown in Fig. 5.5.1 is the variation of $\langle \nabla\mathbf{u}:\nabla\mathbf{u} \rangle$ with τ_p^+ and the cross-sectional location. It is seen that for the near-wall and vortex center locations, as τ_p^+ increases particles accumulate in regions of increasing $\langle \nabla\mathbf{u}:\nabla\mathbf{u} \rangle$ before passing through a maximum, after which this trend is reversed. This maximum occurs within the range $2 \le \tau_p^+ \le 4$. In the near wall region, particles tend to have the maximum preferential concentration indicated by the largest values of $\langle \nabla\mathbf{u}:\nabla\mathbf{u} \rangle$. Maxey (1987) has shown that heavy particles accumulate in regions of high $\nabla\mathbf{u}:\nabla\mathbf{u}$. As expected, the duct center shows little variation in $\langle \nabla\mathbf{u}:\nabla\mathbf{u} \rangle$ with particle Stokes number. This is because there are relatively low fluid gradients in this region. It is the proximity to the wall that has greater effect on the level of preferential concentration than the time-mean flow pattern. For example, the vortex center region is the second closest to the wall among the locations examined in this work, and accordingly exhibits the second highest level of preferential concentration. In theory, for very large or very small particles, the mean value of $\nabla\mathbf{u}:\nabla\mathbf{u}$ at particle positions should be equal to the mean fluid value of $\nabla\mathbf{u}:\nabla\mathbf{u}$, which goes to zero. However, particles of intermediate size tend to accumulate in areas of high $\nabla\mathbf{u}:\nabla\mathbf{u}$. This can be seen more clearly in the PDFs at the various locations.

Figure 5.5.2 displays the PDFs of $\langle \nabla \mathbf{u} : \nabla \mathbf{u} \rangle$ in the near wall region for three particle Stokes numbers along with the fluid PDF. It is clear that the PDF of $\langle \nabla \mathbf{u} : \nabla \mathbf{u} \rangle$ at particle locations is shifted towards more positive values of $\langle \nabla \mathbf{u} : \nabla \mathbf{u} \rangle$, with a greater shift for larger particles. In Figs. 5.5.3 and 5.5.4, similar trends are seen for $\langle \nabla \mathbf{u} : \nabla \mathbf{u} \rangle$ at the vortex center and saddle regions, respectively. However, in Fig. 5.5.5, which is the PDF of $\langle \nabla \mathbf{u} : \nabla \mathbf{u} \rangle$ for the center of the duct, we see the least preferential concentration indicated by very slight departure of the particle PDFs from the fluid PDF. This was evident in Fig. 5.5.1 as well. This confirms that the preferential concentration of particles is dependent upon the distance from the wall. As we move away from the wall, the streaky turbulent structures of $\nabla \mathbf{u} : \nabla \mathbf{u}$, along which particles tend to accumulate, become weaker, if present at all. This argument holds true for the statistics shown in the previous sections, as the center of the duct is found to have relatively weak preferential accumulation of particles based on all statistics used in this work.

Chapter 6. Deposition Results

A parametric study of the effects of varying particle response time, τ_p^+, on wall-deposition has been performed. In addition to the one-way coupled simulations (no particle feedback effects on the fluid), the effects of two-way coupling (the inclusion of particle feedback effects) and particle collisions on deposition have been investigated. Particle volume fractions as high as 10^{-3} were chosen to study the effects of two-way coupling and particle collisions on deposition. The probability distribution functions (PDFs) of the particle deposition location, the average streamwise and wall-normal deposition velocities, and deposition rates as a function of τ_p^+ are presented. The mean fluid statistics are averaged for more than 60 dimensionless time units. Further, the deposition statistics are averaged in time (34 time units for the $\tau_p^+ = 0.072$ particles and 8 time units for the $\tau_p^+ = 256.32$ particles), in the homogeneous streamwise direction, and over the four duct walls (due to a $\pi/2$ rotation symmetry about the duct axis in the cross-sectional plane). Due to the higher deposition rates for large particles, less averaging time was needed to achieve smooth PDFs for large particles compared to small particles. One-way coupling results will be presented first, followed by a discussion of the effects of two-way and four-way coupling. The current computed deposition rates are also compared to previous experimental data in a circular pipe.

See Table 6.1 for particle parameters studied in the deposition simulations. The fluid simulation parameters are the same as in Chapter 5, except the time step has been increased to 0.0005. Particles are assumed to deposit when they are within one radius from a wall. The particles are initially randomly positioned in the domain with initial velocities equal to the local fluid velocity.

6.1 One-way coupling

6.1.1 Wall-Normal Deposition Velocity

The deposition velocities in the wall-normal and the streamwise directions are of interest in studying the erosion of the duct walls. In a channel or a pipe flow, the deposition velocity is a constant over the wall due to the spatial averaging in the two homogeneous directions parallel to the wall. However, in a square duct, due to the inhomogeneous nature of the cross-sectional plane, the deposition velocities will vary over the duct walls, with a $\pi/2$ rotational symmetry about the duct axis in the cross-sectional plane. In this section we discuss the particle deposition velocities as a function of particle Stokes number, τ_p^+. Two-way coupling effects and interparticle collisions are not considered in this section.

Results have been presented for ten values of τ_p^+, corresponding to two values of particle to fluid density ratios ($\rho_p/\rho_f = 1000$ and 8900) and five diameters for each density ratio. The various parameters correspond to simulations 1-10 in Table 6.1. Presented in Fig. 6.1.1.1 are the wall-normal deposition velocities for the various τ_p^+ corresponding to $\rho_p/\rho_f = 1000$. Here, we see several interesting trends in the wall-normal deposition velocities as a function of deposition location. First, as the Stokes number is increased from 0.072 to 1.8, the wall normal deposition velocity does not change significantly. However, further increase in τ_p^+ from 1.8 to 28.8 leads to a substantial increase in the wall normal deposition velocity across the duct width. Also, we clearly see that the deposition velocity varies across the duct width. We see the lowest deposition velocity at the corners of the duct (deposition location = 0 and 1 in Fig. 6.1.1.1), and it increases progressively as we move away from the corners.

The term "deposition location" is analogous to either x/δ or y/δ due to the $\pi/2$ rotational symmetry in the cross-sectional plane about the duct axis. For $\tau_p^+ = 28.8$, we also see secondary peaks in the deposition velocity at roughly 10% to 15% of the duct width from the corner. For all particle response times, we see the maximum deposition velocity at the center of the duct wall. This is due to the relatively large streamwise velocity gradients in the wall-normal direction at this location compared to the corners (which can be seen in Fig. 1.1 from the contours of streamwise velocity). This causes a larger lift force (directed towards the wall) and thus, an increased wall-normal deposition velocity. The wall-normal deposition velocities for the τ_p^+ corresponding to $\rho_p/\rho_f = 8900$ are shown in Fig. 6.1.1.2. The wall-normal deposition velocity is seen to increase with τ_p^+ for the range of response times examined. The two cases with the smallest τ_p^+ have nearly identical wall-normal deposition velocities. The non-uniform velocity profile across the duct width is again apparent.

6.1.2 Streamwise Deposition Velocity

The streamwise deposition velocity is a good measure of the slip between the particles and the fluid in the near wall region since the fluid velocity goes to zero there. We can see in Figs. 6.1.2.1 and 6.1.2.2 that the less inertial particles deposit on the wall with lower streamwise velocities. This is because they respond better than the more inertial particles to fluid deceleration as we approach the wall. In Fig. 6.1.2.1, for a higher $\tau_p^+ = 7.2$, we see that the particles tend to noticeably retain streamwise momentum after passing through the near-wall shear layer. Further, the non-uniform pro files demonstrate the effect of secondary flows. The streamwise velocity contours, shown in Fig. 1.1, bulge towards the corners indicating higher fluid momentum due to secondary flows in these regions. Thus, the particles in the bulges can acquire higher streamwise momentum when compared to other cross-sectional locations. As a result, the deposition velocity is seen to exhibit a wavy pattern with a maximum at the center of the duct wall (where the streamwise velocity is highest for a given y^+ compared to other locations), and two secondary peaks. For $\rho_p/\rho_f = 8900$, shown in Fig. 8, we see similar trends. In Fig. 6.1.2.2, as τ_p^+ is increased to 256.32, we see a progressive increase in the streamwise deposition velocities. Also, it is clear that as τ_p^+ increases, particles are less responsive to the near wall fluid no-slip condition resulting in higher deposition velocities.

6.1.3 Deposition Location

The particle deposition location is not an issue of concern for pipes and channels due to the homogeneous nature of the two directions parallel to the walls in these geometries. For a square duct, due to the additional inhomogeneous wall-normal direction, the deposition pattern is more complex. By examining the PDFs of the deposition location for $\rho_p/\rho_f = 1000$ and the corresponding values of τ_p^+, shown in Fig. 6.1.3.1, we can identify several trends. First, deposition is always seen to be more likely near the center of the duct wall for all particle Stokes numbers examined. For the particles with $\tau_p^+ = 0.072$ and 0.45, we see a very small fraction of particles depositing near the duct corners. As τ_p^+ is increased, deposition near the corners is higher and the particles tend to deposit more uniformly across the duct width. For $\rho_p/\rho_f = 8900$, the pdf's of the deposition location show similar trends (Fig. 6.1.3.2). The increasing uniformity in particle deposition across the duct width with particle response time can be clearly observed in Fig. 6.1.3.2. However, even for the largest particles, deposition is still least likely in the corners. The maximum deposition near the center of the duct walls can be explained by examining the

secondary flow patterns in Fig. 1.2. Near the duct corners, the secondary flows are aligned such that they will sweep particles in this region towards the center of the duct walls, where the particles remain and deposit.

6.1.4 Deposition Rates

Deposition rates are important in applications such as droplet impingement on a heat exchanger surface, dust deposition on surfaces in clean rooms, etc. Deposition rates will be higher for a square duct than for channel flow. This is because of the alignment of the secondary flow structures that are more likely to transport particles to a wall. In Figs. 6.1.4.1 and 6.1.4.2, we plot the number of deposited particles, N_d, normalized by the number of initial particles, N_i, as a function of time for the one-way coupled simulations for $\rho_p/\rho_f = 1000$ and 8900, respectively. It is clear that the larger τ_p^+ particles travel to the wall at a faster rate. This trend agrees with what other researchers have found for pipe and channel flow (Wang and Squires 1996a; McCoy and Hanratty 1977).

The particle deposition rate can be expressed as the following (Wang and Squires 1996a):

$$V_d = \frac{N_{dt}/A/t}{N/V} \qquad (6.1.4.1)$$

where N_{dt} is the number of deposited particles during time t, A is the area of deposition, N is the number of particles at the beginning of the deposition sampling time, and V is the volume of the domain. The deposition rate can also be calculated from the slope of the linear portion of the curves in Figs. 6.1.4.1 and 6.1.4.2. In Fig. 6.1.4.3, we plot the deposition rates normalized by the average friction velocity and compare them with the empirical correlations developed by McCoy and Hanratty (1977) for pipe flow. The trends are similar to those seen in pipe flow. However, for $\tau_p^+ = 0.072$ particles, the deposition rates in a square duct are seen to be up to two orders of magnitude higher than in a pipe flow. It is interesting to note that for large particles, the correlation of McCoy and Hanratty (1977) agrees well with the square duct deposition rates. This is because the largest particles are not as sensitive to the secondary flows and thus more closely match pipe flow results.

6.2 Effects of Two-Way Coupling and Particle Collisions

6.2.1 Low volume fraction ($\phi_v \leq 10^{-4}$)

At low particle volume fractions, ϕ_v, as for the present simulations with $\phi_v \leq 10^{-4}$, it is expected that particle feedback effects or collisions will not play a major role. However, the locally high volume fraction of particles due to preferential concentration may warrant the inclusion of the above effects. Hence, four-way coupled (two-way coupling plus collisions) simulations were also carried out for three particle representative Stokes numbers ($\tau_p^+ =$ 1.8, 28.8, and 256.32).

By examining the wall-normal deposition velocity, shown in Fig. 6.2.1.1, we see that four-way coupling does not appreciably change the deposition velocities for $\tau_p^+ = 1.8$. This is expected since the volume fraction for this case is very low ($\phi_v = 1.4\times10^{-6}$). For the $\tau_p^+ = 28.8$ particles, even at higher ϕ_v (6.67×10^{-5}), we again see little difference in the wall-normal deposition velocity when four-way coupling is considered. However, for the $\tau_p^+ =$ 256.32 particles, we see a significant increase in the wall-normal deposition velocity when four-way coupling is considered. As will be shown later, this effect is largely attributed to the inclusion of particle collisions.

The streamwise deposition velocities are shown in Fig. 6.2.1.2 for both one-way and four-way coupled cases. For all particle Stokes numbers reported, there is no significant difference in the one-way and four-way coupling cases for the volume fractions considered ($\phi_v \leq 6.67\times10^{-5}$). For $\tau_p^+ = 1.8$, the one-way and four-way plots are nearly indistinguishable.

In Fig. 6.2.1.3, we examine the effects of four-way coupling on the deposition location for $\phi_v \leq 6.67\times10^{-5}$. No significant difference can be seen for any of the Stokes numbers examined. This indicates that neither collisions nor particle feedback effects alter the deposition location of particles for volume fractions of the order of 6.67×10^{-5} or less.

Shown in Fig. 6.2.1.4 is the number of deposited particles (normalized by the number of initial particles) as a function of time. In all the cases examined at $\phi_v \leq 6.67\times10^{-5}$, four-way coupling increased the deposition rates. Similar trends are seen in Fig. 6.1.4.3. Although the difference is not drastic between one-way and four-way coupled results, the trend of increased deposition rates as a result of four-way coupling is apparent.

Thus, the results obtained with inclusion of two-way coupling and collisions for cases with $\phi_v \leq 6.67\times10^{-5}$ show that the one-way coupling results were accurate and that it was reasonable to neglect collisions and particle feedback effects. Due to the small differences in the results for one-way and four-way coupled cases (for most quantities examined), we feel that the one-way coupling approach is sufficient for square duct studies involving volume fractions less than 6.67×10^{-5}.

6.2.2 Higher volume fractions ($\phi_v = 10^{-3}$)

To better understand the effects of particle feedback and collisions, one must increase the volume fraction to a level where they are likely to be dominant. Therefore, one set of simulations with both two-way and four-way coupling was done for $\tau_p^+ = 256.32$ with an initial volume fraction of 10^{-3}, which corresponds to 1.5 million particles. In this set of simulations, any significant difference between the two-way and four-way coupling results can be attributed to particle-particle collisions.

The wall-normal deposition velocity is shown in Fig. 6.2.2.1. Previous one-way and four-way coupled results with 100,000 initial particles ($\phi_v = 6.67\times10^{-5}$) are included for comparison. When the volume fraction is increased to 10^{-3} and only two-way coupling is considered, we see slightly higher wall-normal deposition velocities when compared with results at $\phi_v = 6.67\times10^{-5}$. This indicates that the particle feedback effect leads to a marginal increase in wall-normal deposition velocities. However, when four-way coupling at $\phi_v = 10^{-3}$ is examined, we see striking differences in the results. It is observed that the maximum wall-normal deposition velocity now occurs near the corners. The deposition velocity is increased by a factor greater than two due to collisions. This clearly indicates that the inclusion of particle-particle collisions can significantly alter the results of wall-normal deposition velocities at relatively high volume fractions.

The streamwise deposition velocity is shown in Fig. 6.2.2.2. With two-way coupling, the increase in volume fraction is clearly seen to decrease the streamwise deposition velocities. For $\phi_v = 10^{-3}$, inclusion of particle collisions is seen to decrease the deposition velocity even further. Higher volume fractions are also seen to increase the non-uniformity across the duct walls for the streamwise deposition velocities.

The PDFs of the deposition location are shown in Fig. 6.2.2.3. Two-way coupling is seen to marginally augment the non-uniform deposition pattern when compared to the one-way coupled results at $\phi_v = 6.67\times10^{-5}$. The effects of collisions on deposition location, which can be seen by comparing two-way and four-way coupling results for $\phi_v = 10^{-3}$, are not significant. We can conclude that collisions do not alter the deposition location significantly even for volume fractions up to 10^{-3}.

Shown in Fig. 6.2.2.4 is the time history of the deposition. The number of deposited particles is normalized by the number of initial particles so that results may be directly compared to results in the earlier sections of this work. It is seen that collisions increase deposition rates. The deposition rates for $\phi_v = 10^{-3}$, normalized by the average friction velocity, are plotted in Fig. 6.1.4.3 along with the low volume fraction results. The same trends as for the low volume fraction cases are observed.

Chapter 7. Conclusions and Recommendations

7.1 Conclusions

Turbulent particle-laden flow in a straight duct of square cross-section has been examined using the Large Eddy Simulation (LES) technique. The unsteady, three-dimensional Navier-Stokes equations for an incompressible flow of constant viscosity have been solved numerically in conjunction with the Lagrangian particle equation of motion. Time-dependent numerical simulation of square duct flow is a challenging task due to the presence of only one homogeneous direction. The simulations are more computationally expensive since statistics are two-dimensional, not one-dimensional as in periodic pipe or channel flow. Also, the integration time for a square duct must be longer due to the reduced sample size for statistical averaging. Thus, only low Reynolds number cases were considered for this research effort.

In the LES simulation, the filtered Navier-Stokes equations have been solved using finite volume methods on a collocated grid. A fractional step method has been used to decouple the pressure from the momentum equations. Top-hat filtering, implemented through implicit grid filtering, has been used. The subgrid scale stresses have been modeled using a dynamic kinetic energy model as proposed by Kim and Menon (1997). The governing equations were discretized in space using second-order central differencing. The convective terms were treated using the Adams-Bashforth scheme, and the diffusion terms were handled with the Crank-Nicolson scheme. The pressure-Poisson equation, resulting from the Harlow-Welch fractional step method, was solved using an algebraic multigrid method. The simulations were performed at a Reynolds number of 360 based on duct width and average friction velocity. The grid used was $80\times80\times128$ in the two wall-normal and streamwise directions, respectively.

The code has been verified in turbulent periodic channel flow at $Re_\tau = 180$ and 590, based on the channel half-height and friction velocity. Better agreement is seen at $Re_\tau = 180$ than $Re_\tau = 590$. The grid was held fixed at $100\times100\times50$ in the streamwise, wall-normal, and spanwise directions, respectively. For $Re_\tau = 180$, four cases are compared to the DNS data: the no-model, the Horiuti model, the dynamic k model on a uniform grid, and the dynamic model on a stretched grid. In the near-wall region, all the cases compare well with the DNS data, with the Horiuti and no-model runs coming closest to matching the near-wall data. Near the channel centerline, all models over predict the DNS data. The Horiuti model is seen to overpredict the DNS by more than 10%, with the dynamic model on a stretched grid only overpredicting the DNS by less than 2%. The resolved streamwise rms velocity predicted by the dynamic k model on a stretched grid best predicts the DNS data, followed closely by the no-model case. However, once the subgrid fluctuations are added, the models are overpredicting the DNS by as much as 30% at the peak of the profile. This means that the models are predicting excessive subgrid energy. It should be noted that all finite-volume top-hat filter LES results are grid dependent. One can improve the results by increasing the grid resolution and eventually one will approach the DNS solution. However, this is not practical and one must choose a grid resolution much coarser than the DNS simulation. The wall-normal rms velocity results show that the no-model case best predicts the DNS data. Both the resolved rms values from the k models underpredict the DNS data, as they should since it is the total rms value which should compare well with the DNS data. However, once the subgrid fluctuations are added, it is seen that the models overshoot the DNS by roughly 35% at the peak of the profile. The lack of smoothness in the total rms velocity predicted by the dynamic model is a result of its prediction

of the sgs k, which is non-smooth near the wall. This is due to the method in which the grid is created, as two daughter cells of a coarse grid cell will have the same size, therefore no grid stretching between daughter cells, which decreases the resolution near the wall and thus decreases the performance of the model. Ideally, one would generate a stretch for the fine grid cells which perfectly coincides with the coarse grid. However, this is prohibitive especially for complex geometries. It is seen that both k models' resolved spanwise rms velocities under-predict the DNS data as they should. However, the total spanwise rms values over-predict the DNS data by roughly 33% near the peak of the profile. The no-model case also overpredicts the DNS, but to a lesser degree of approximately 20%. The Reynolds stress term $u'v'$ is seen to be best predicted by the no-model LES, followed closely by the Horiuti model. The dynamic k model underpredicts the maximum magnitude of the term by roughly 28%. The dynamic model predicts roughly twice as much sgs k as the Horiuti model. The sgs k correctly goes to zero near the wall for both models. It is seen that the advantage of the dynamic model is that no wall model is needed to generate correct near-wall behavior of the model coefficients. The model automatically damps the production term at the wall. This is a tremendous advantage when the square duct geometry is considered, as the wall models are unknown for the square duct geometry, and poorly understood even for simple geometries like channels.

The grid is held fixed and the Reynolds number is increased to 590 for the next comparisons. The DNS data by Moser, Kim, and Mansour (1999) is used as the baseline for comparison. The Horituti model better predicts the mean velocity DNS data. However, the qualitative trends, such as inflection points, in the DNS profile are not captured at this Reynolds number. The dynamic model captures the near wall region better than the Horituti model, yet near the centerline the dynamic model overpredicts the DNS data by roughly 20%. It is seen that none of the simulations capture the location of the peak or the magnitude of urms accurately. Once the subgrid fluctuations are added, the dynamic model overpredicts the rms velocity by roughly 100%. The Reynolds number is clearly much too large to be simulated by only 0.5 million nodes in this LES. A more positive outcome may be seen in the vrms results. The k models correctly underpredict the vrms DNS data when the resolved rms quantity is considered. By adding the subgrid fluctuation, the peak shifts closer to the location of the peak in the DNS data, however, the magnitude is then overpredicted by 30% and 80% for the Horiuti and dynamic k models, respectively. The Horiuti model correctly underpredicts the wrms DNS data when the resolved rms velocity is considered. All other forms of the rms velocity overpredict the DNS data, with the dynamic k model overpredicting the peak by roughly 100%.

The preferential concentration of heavy particles in turbulent square duct flow was studied using large eddy simulations. Six particle classes (τ_p^+ = 0.25, 0.5, 1, 2, 4, and 8) and four locations in the cross-section were examined. Particles are seen to accumulate in regions of high $\nabla\mathbf{u}:\nabla\mathbf{u}$ and compressional strain and regions of low swirling strength. The trends are more pronounced for large particles with Stokes numbers of 2 and 4. Of the four locations studied, the location that exhibited the most pronounced preferential accumulation was the near wall region (x^+=182.8, y^+=19.8). The vortex center region, which was the second closest to the walls of the locations examined, exhibited the second highest level of preferential concentration of particles. The duct center, being the further location from the walls, showed relatively weak preferential accumulation of particles. From this it is clear that preferential accumulation of particles is predominantly a near wall effect for internal flows in complex geometries.

The vorticity magnitude displays several trends worth noting. Near the wall and in the vortex center regions, large particles are seen to accumulate in regions of high vorticity whereas small particles are seen to accumulate in regions of low vorticity. In the saddle region and duct center, all particles are seen to accumulate in regions of low vorticity. This is due to the vorticity being corrupted by the strong shear near the walls, which causes the vorticity to become a less sensitive measure of the preferential concentration. Therefore, swirling strength, not vorticity, is a more appropriate measure of preferential concentration of particles in regions which contain high shear.

Contours of near wall statistics along with near wall particle position scatter plots confirm the trends seen in the PDFs. Particles are seen to accumulate in low speed streaks near the wall, which is similar to what has been seen by previous researchers in channel flow, for example, see Zhang and Ahmadi (2000). Particle scatter plots reveal that the particles form concentration patterns near the wall which are more complex than what is seen in simpler geometries such as channel flow.

The deposition of heavy solid particles in a fully developed turbulent square duct flow was studied using large eddy simulations. Ten particle Stokes numbers, corresponding to two density ratios (ρ_p/ρ_f = 1000 and 8900) and five particle diameters ($d_p/\delta \times 10^6$ = 100, 250, 500, 1000 and 2000), were studied. Two particle number densities were examined, corresponding to 10^5 and 1.5×10^6 particles initially in the domain. In addition to one-way coupling, two-way, and four-way coupling effects were also considered.

In general, the wall-normal deposition velocity is seen to increase with Stokes number. For one-way coupling, the maximum wall-normal deposition velocity occurs near the center of the duct wall. However, collisions cause the maximum wall-normal deposition velocity to occur near the corners.

The streamwise deposition velocity is seen to increase with τ_p^+. Secondary flows are found to cause a non-uniform pattern in the velocity profile across the duct width. The streamwise deposition velocity is seen to be highest near the center of the duct wall for all particle response times examined. Two-way coupling and collision effects decrease the streamwise deposition velocity.

Deposition is seen to be least likely in the duct corners, and most likely in the duct center. As the Stokes number is increased, the deposition pattern becomes more uniform across the duct width. Two-way coupling effects tend to cause an augmentation of the wavy deposition pattern. At low volume fractions, inclusion of two-way coupling and particle collisions did not significantly alter the deposition trends. As a result, the one-way coupled approach is sufficient for volume fractions less than 10^{-4}.

Deposition rates are computed and compared to experimental data in pipe flow. The same qualitative trends as for pipe flow are seen. However, the square duct exhibits up to two orders of magnitude higher deposition rates for small particles. Large particles are seen to more closely match the pipe flow data. Two-way and four-way coupling enhance the deposition rates.

7.2 Recommendations for Future Work

Some suggestions for future work are as follows. Direct Numerical Simulations could be performed for the same problem to verify the LES results obtained in this work. The method used by Madabhushi (1993) would be the natural choice to use for DNS as it is pseudo-spectral and would outperform the finite-volume method used in this

thesis. A comparison of subgrid models in a square duct would also be of interest for LES modeling of wall-bounded flows. With parallel processing becoming more accessible, higher Reynolds numbers could be examined if one implemented a parallel algebraic multigrid solver to solve the pressure-Poisson equation arising from the fractional step method used in this work. Such solvers are currently available from Lawrence Livermore National Labs – Center for Applied Scientific Computing (LLNL-CASC). Their solver, called Boomer AMG, has successfully solved linear problems on over 1,000 processors. Such a solver could greatly enhance the code used in this dissertation. Additionally, several recent advancements in cache optimization of AMG solvers has been performed by numerous authors. Even on single processors, speedup factors greater than 5 have been observed, which would again greatly enhance the performance of the code used in this work. It is also interesting to study the particle statistics such as mean and RMS particle velocities and compare them with a future experiment. Horizontal square duct flow would also represent a future study with many practical applications, as gravity would now cause preferential deposition on the walls normal to the gravitational acceleration vector. This directly leads to studying particle transport in a square duct at an arbitrary angle of inclination. This author plans to study preferential concentration of bubbles in a square duct in the very near future as an extension of this work. Eulerian methods could be used to study higher volume fractions of particles, and also compared to experiments. Many engineering applications involve flow in non-circular ducts of trapezoidal cross-section, as in machined grooves in MEMS devices. An LES study could reveal the shape of secondary flows in such ducts, which has not been examined to the author's knowledge. Particle transport in these ducts would also be of importance.

Tables

Table 2.2.1: PDPA Parameters

Laser Wavelength (nm)	632.8
Diameter of Laser Beam (mm)	0.68
Transmitter Focal Length (mm)	495
Receiver Focal Length (mm)	495
Receiver Aperture (microns)	100
Location of Receiver	30° off-axis, forward scatter
Sampling Rate of Processor	50,000 Hz maximum
Beam Separation (mm)	34
Fringe Spacing (microns)	9.21
Number of Fringes	63
Probe Area (cm^2)	0.00062 to 0.0024
Index of Refraction of Liquid Refrigerant	1.23
Accuracy of Size Measurements	± 5%
Accuracy of Velocity Measurements	± 1%

Table 2.2.2: Experimental Conditions

Pressure Before Nozzle (kPa)	748 to 1213 ± 6
Temperature Before Nozzle (K)	298.4 to 320.1 ± 0.05
Pressure In Header (kPa)	728 to 774 ± 6
Mass Flow Rate (g/s)	1 to 3 ± 0.05
Quality In Header	0 to 0.15 ± 0.005

Table 5.1: Grid Spacing in Cross Section of Square Duct

y	y^+	Δy	Δy^+
4.8934E-03	1.7616E+00	9.7868E-03	3.5232E+00
1.4680E-02	5.2849E+00	9.7868E-03	3.5232E+00
2.4589E-02	8.8521E+00	1.0031E-02	3.6113E+00
3.4621E-02	1.2463E+01	1.0031E-02	3.6113E+00
4.4778E-02	1.6120E+01	1.0282E-02	3.7016E+00
5.5060E-02	1.9822E+01	1.0282E-02	3.7016E+00
6.5471E-02	2.3569E+01	1.0539E-02	3.7941E+00
7.6010E-02	2.7364E+01	1.0539E-02	3.7941E+00
8.6681E-02	3.1205E+01	1.0803E-02	3.8890E+00
9.7484E-02	3.5094E+01	1.0803E-02	3.8890E+00
1.0842E-01	3.9032E+01	1.1073E-02	3.9862E+00
1.1949E-01	4.3018E+01	1.1073E-02	3.9862E+00
1.3071E-01	4.7054E+01	1.1350E-02	4.0859E+00
1.4206E-01	5.1140E+01	1.1350E-02	4.0859E+00
1.5355E-01	5.5277E+01	1.1633E-02	4.1880E+00
1.6518E-01	5.9465E+01	1.1633E-02	4.1880E+00
1.7696E-01	6.3705E+01	1.1924E-02	4.2927E+00
1.8888E-01	6.7998E+01	1.1924E-02	4.2927E+00
2.0096E-01	7.2344E+01	1.2222E-02	4.4000E+00
2.1318E-01	7.6744E+01	1.2222E-02	4.4000E+00
2.2555E-01	8.1199E+01	1.2528E-02	4.5100E+00
2.3808E-01	8.5710E+01	1.2528E-02	4.5100E+00
2.5077E-01	9.0276E+01	1.2841E-02	4.6228E+00
2.6361E-01	9.4899E+01	1.2841E-02	4.6228E+00
2.7661E-01	9.9579E+01	1.3162E-02	4.7384E+00
2.8977E-01	1.0432E+02	1.3162E-02	4.7384E+00
3.0310E-01	1.0912E+02	1.3491E-02	4.8568E+00
3.1659E-01	1.1397E+02	1.3491E-02	4.8568E+00
3.3025E-01	1.1889E+02	1.3828E-02	4.9782E+00
3.4408E-01	1.2387E+02	1.3828E-02	4.9782E+00
3.5808E-01	1.2891E+02	1.4174E-02	5.1027E+00
3.7225E-01	1.3401E+02	1.4174E-02	5.1027E+00
3.8660E-01	1.3918E+02	1.4529E-02	5.2303E+00
4.0113E-01	1.4441E+02	1.4529E-02	5.2303E+00
4.1584E-01	1.4970E+02	1.4892E-02	5.3610E+00
4.3073E-01	1.5506E+02	1.4892E-02	5.3610E+00
4.4581E-01	1.6049E+02	1.5264E-02	5.4951E+00
4.6108E-01	1.6599E+02	1.5264E-02	5.4951E+00
4.7653E-01	1.7155E+02	1.5646E-02	5.6324E+00
4.9218E-01	1.7718E+02	1.5646E-02	5.6324E+00

Table 5.2: Particle Properties for Preferential Concentration Studies

t_p^+	$t_p/(d/u_t)$ x 10^4	d_p/d x 10^6	r_p/r_f
0.25	6.9444	117.85	2500
0.5	13.889	166.67	2500
1	27.778	235.70	2500
2	55.556	333.33	2500
4	111.11	471.40	2500
8	222.22	666.67	2500

Table 6.1: Particle Properties for Deposition Simulations

Simulation	r_p/r_f	d_p/d	d^+	$t_p/(d/u_t)$	t_p^+	f_v	Coupling type
1	1000	0.0001	0.036	0.0002	0.072	8.33×10^{-9}	One-way
2	1000	0.00025	0.09	0.0013	0.45	1.30×10^{-7}	One-way
3	1000	0.0005	0.18	0.005	1.8	1.04×10^{-6}	One-way
4	1000	0.001	0.36	0.02	7.2	8.33×10^{-6}	One-way
5	1000	0.002	0.72	0.08	28.8	6.67×10^{-5}	One-way
6	8900	0.0001	0.036	0.0018	0.6408	8.33×10^{-9}	One-way
7	8900	0.00025	0.09	0.0111	4.005	1.30×10^{-7}	One-way
8	8900	0.0005	0.18	0.0445	16.02	1.04×10^{-6}	One-way
9	8900	0.001	0.36	0.178	64.08	8.33×10^{-6}	One-way
10	8900	0.002	0.72	0.712	256.32	6.67×10^{-5}	One-way
11	1000	0.0005	0.18	0.005	1.8	1.04×10^{-6}	Four-way
12	1000	0.002	0.72	0.08	28.8	6.67×10^{-5}	Four-way
13	8900	0.002	0.72	0.712	256.32	6.67×10^{-5}	Four-way
14	8900	0.002	0.72	0.712	256.32	10^{-3}	Two-way
15	8900	0.002	0.72	0.712	256.32	10^{-3}	Four-way

Figures

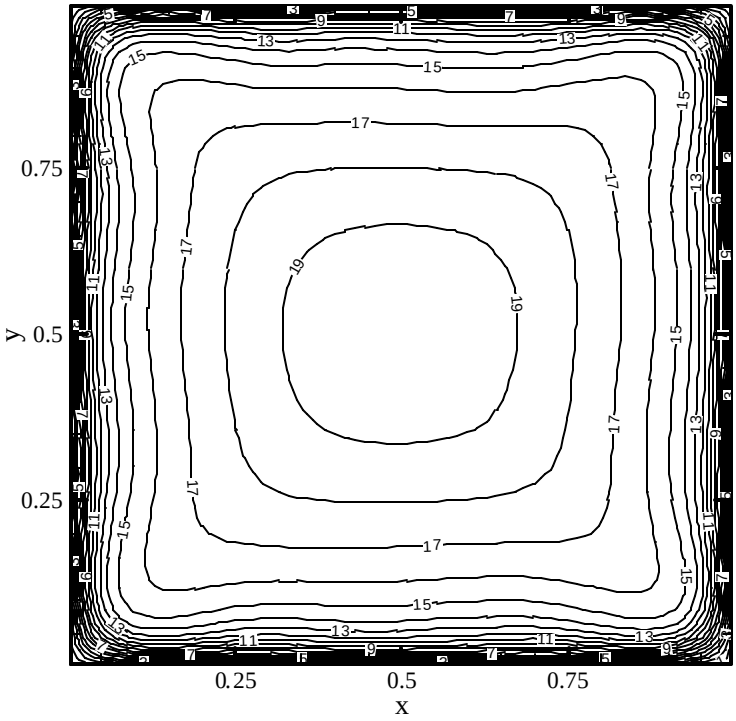

Figure 1.1: Contours of Mean Streamwise Velocity

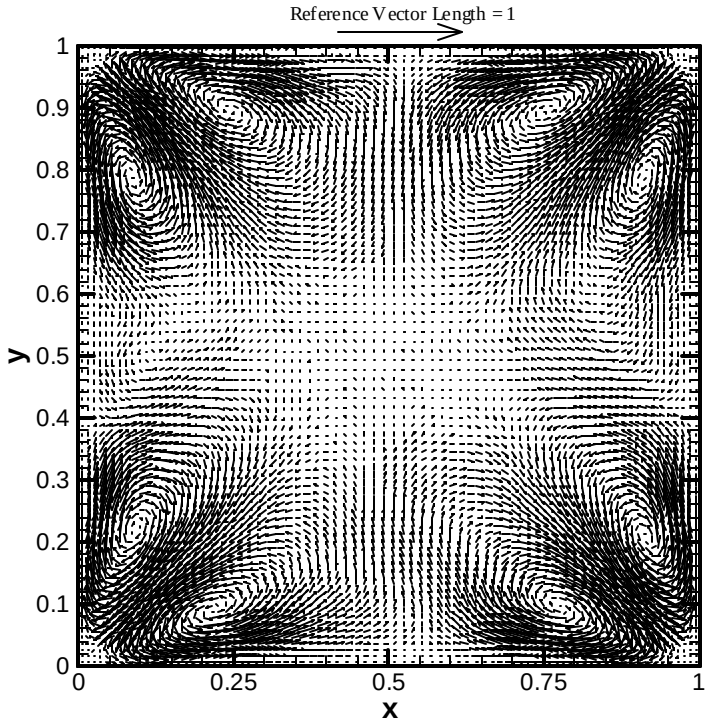

Figure 1.2: Mean Secondary Flows in a Square Duct

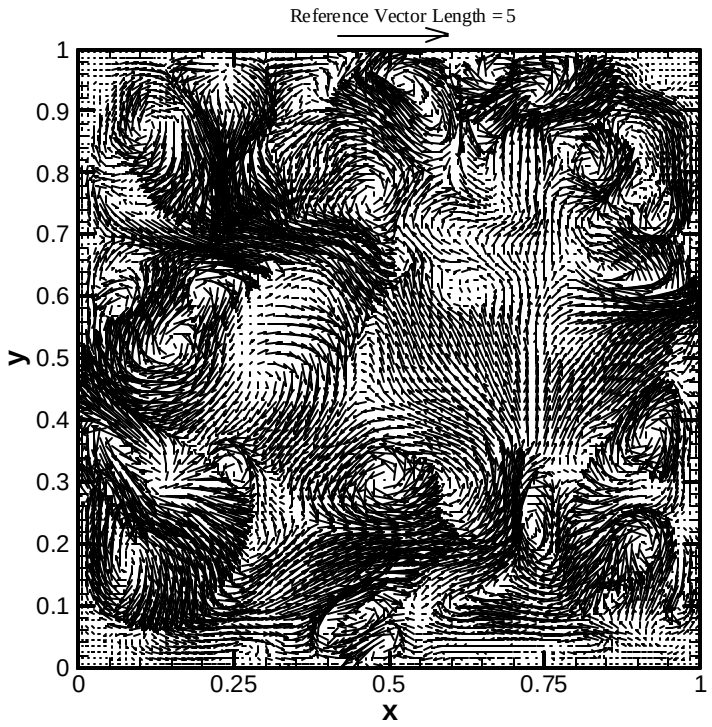

Figure 1.3: Instantaneous Secondary Flows in a Square Duct

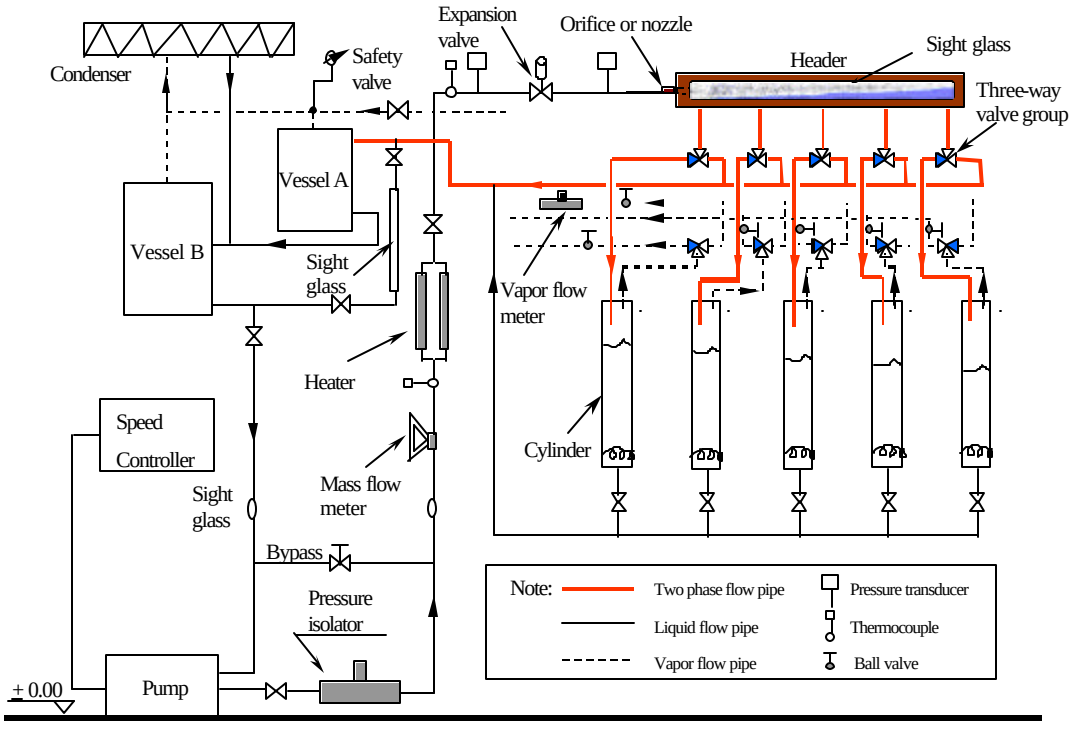

Figure 2.2.1: Experimental Setup

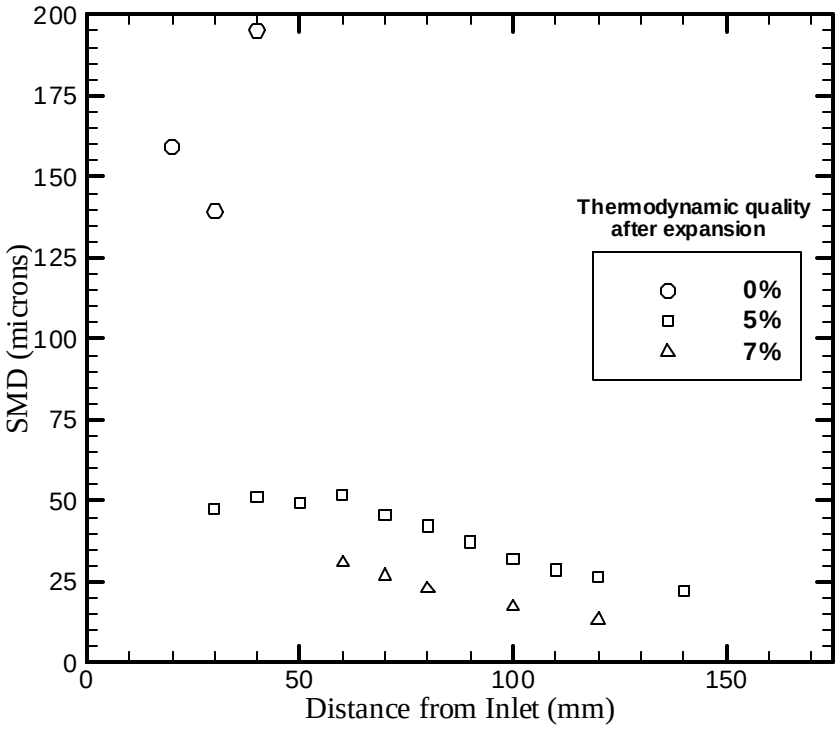

Figure 2.3.1: Centerline Droplet Measurements for 1 g/s

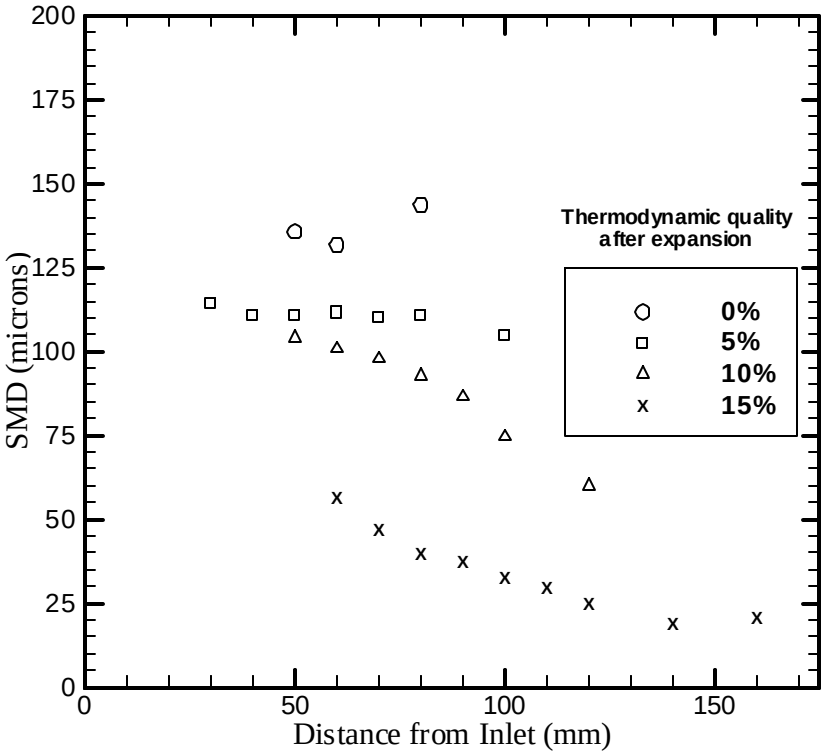

Figure 2.3.2: Centerline Droplet Measurements for 2 g/s

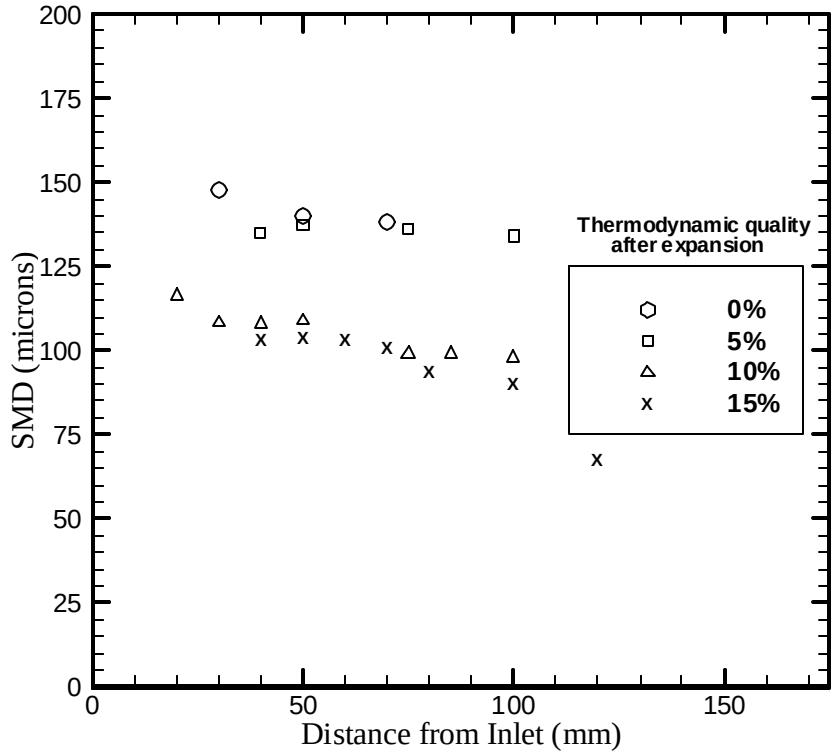

Figure 2.3.3: Centerline Droplet Measurements for 3 g/s

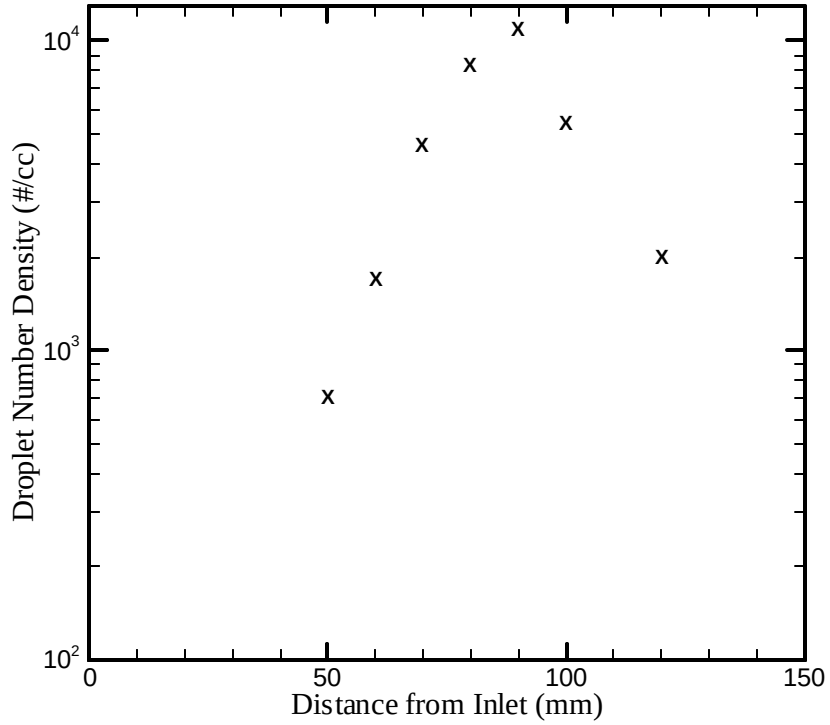

Figure 2.3.4: Centerline Number Density Measurements for 2 g/s, 10% Quality

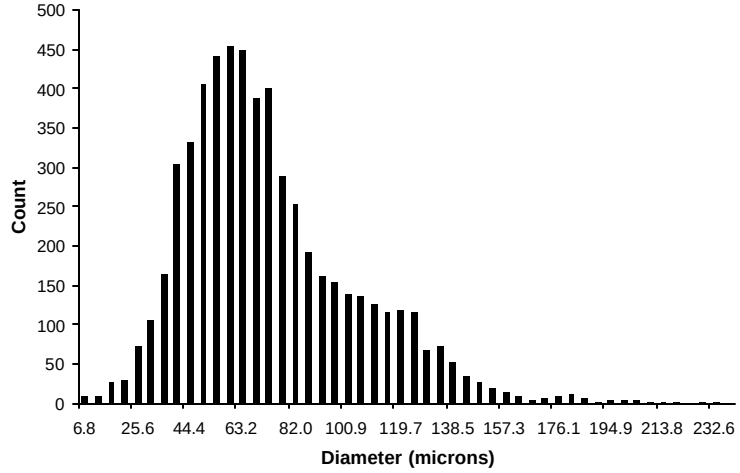

(a)

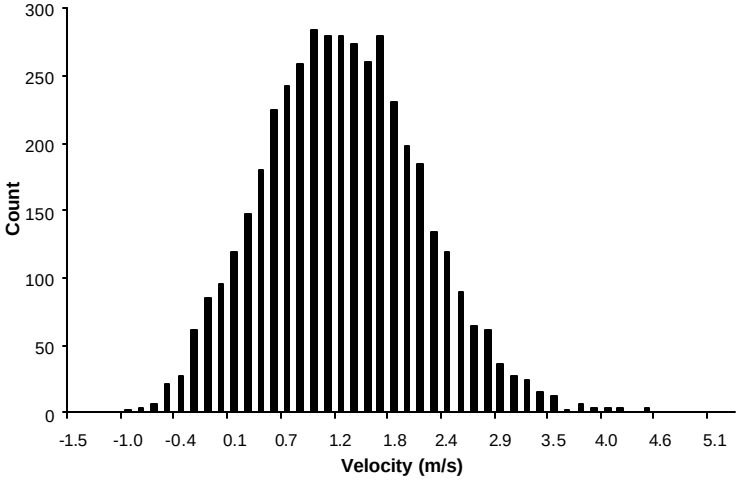

(b)

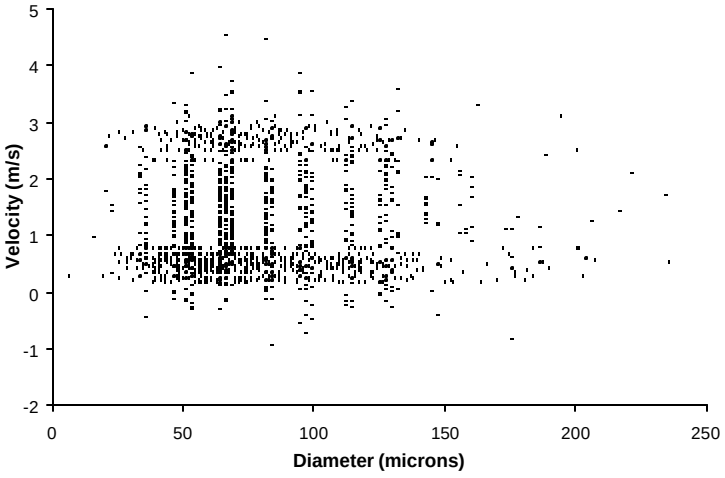

(c)

Figure 2.3.5: Size and Velocity Distributions at 60 mm Downstream, 2 g/s, 10% Quality

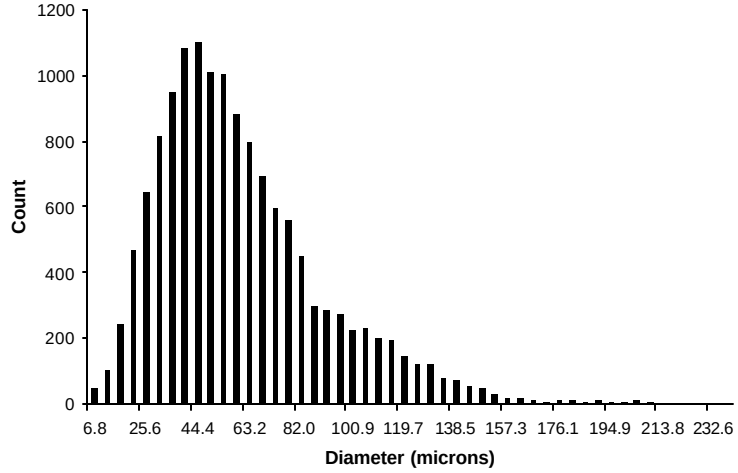

(a)

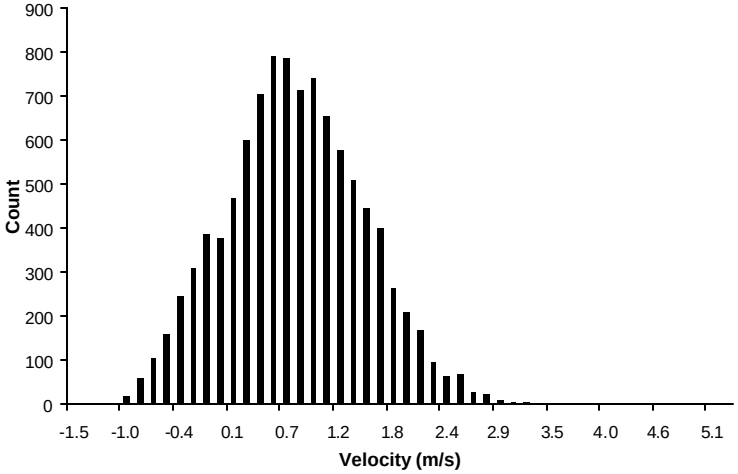

(b)

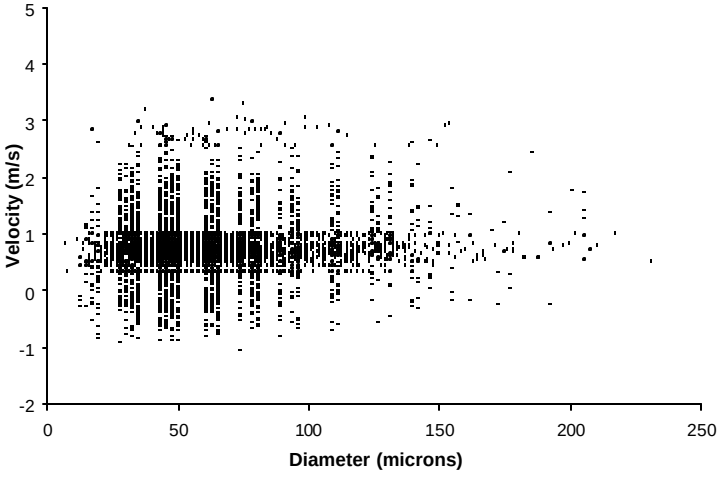

(c)

Figure 2.3.6: Size and Velocity Distributions at 80 mm Downstream, 2 g/s, 10% Quality

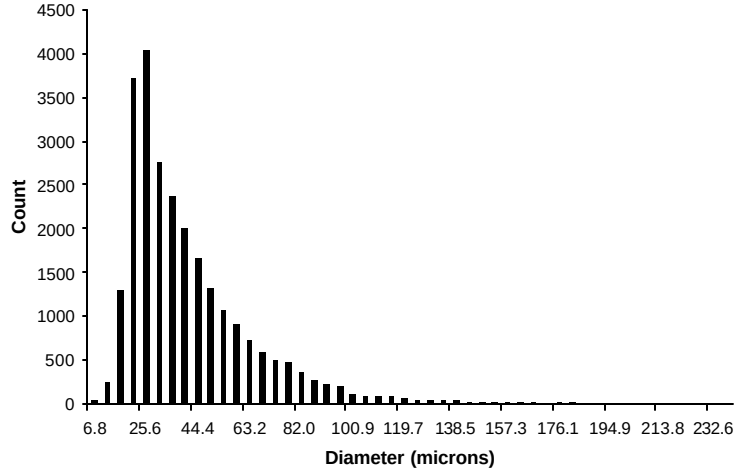

(a)

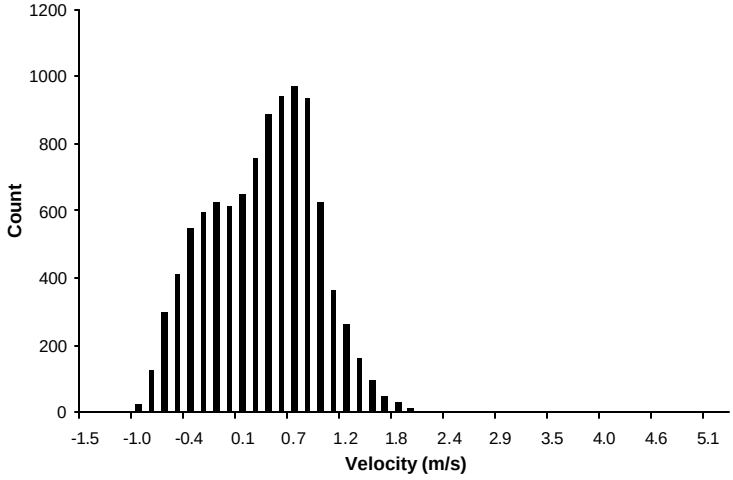

(b)

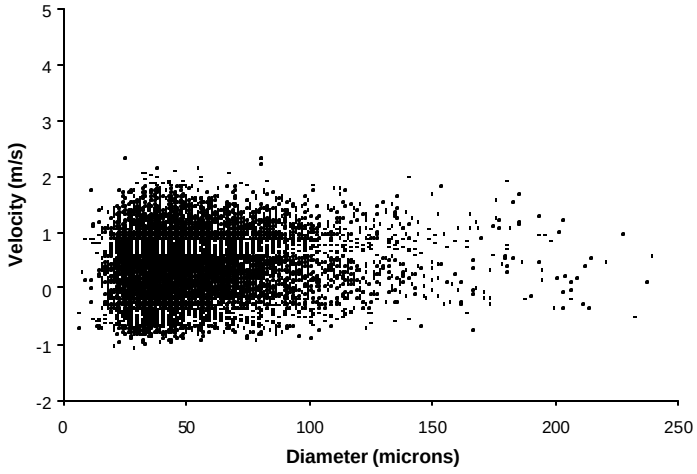

(c)

Figure 2.3.7: Size and Velocity Distributions at 100 mm Downstream, 2 g/s, 10% Quality

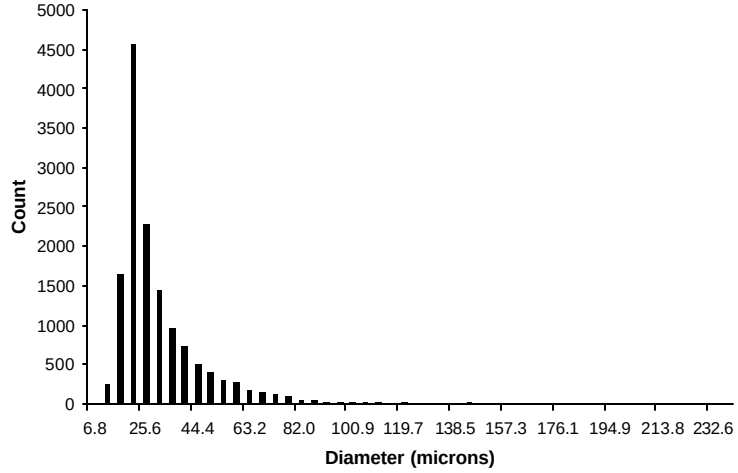

(a)

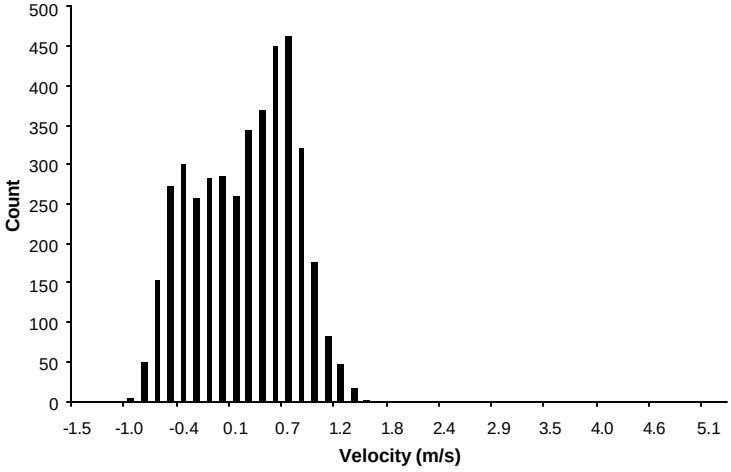

(b)

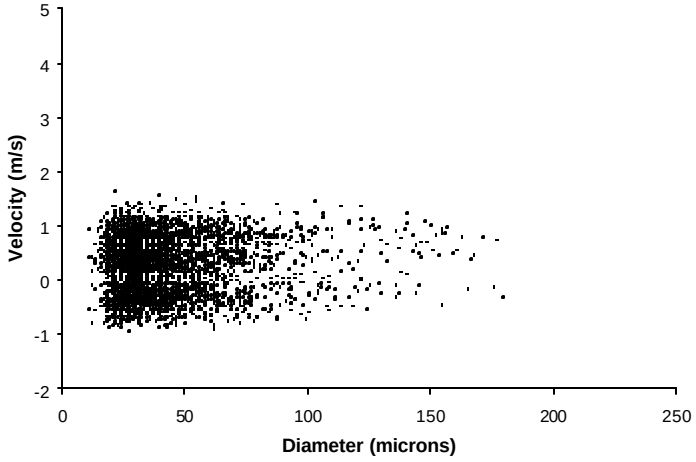

(c)

Figure 2.3.8: Size and Velocity Distributions at 120 mm Downstream, 2 g/s, 10% Quality

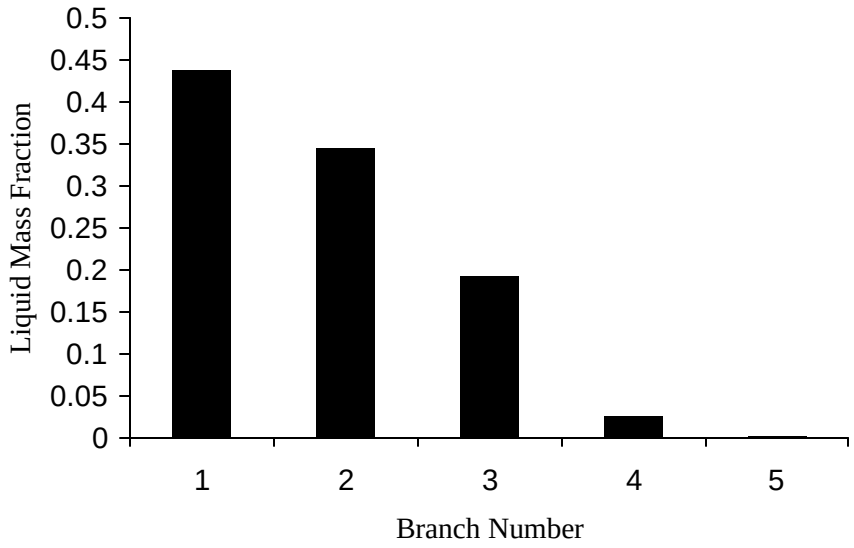

Figure 2.3.9: Distribution Results for 15 g/s, 10% Quality with 3/8" Pipe Inlet

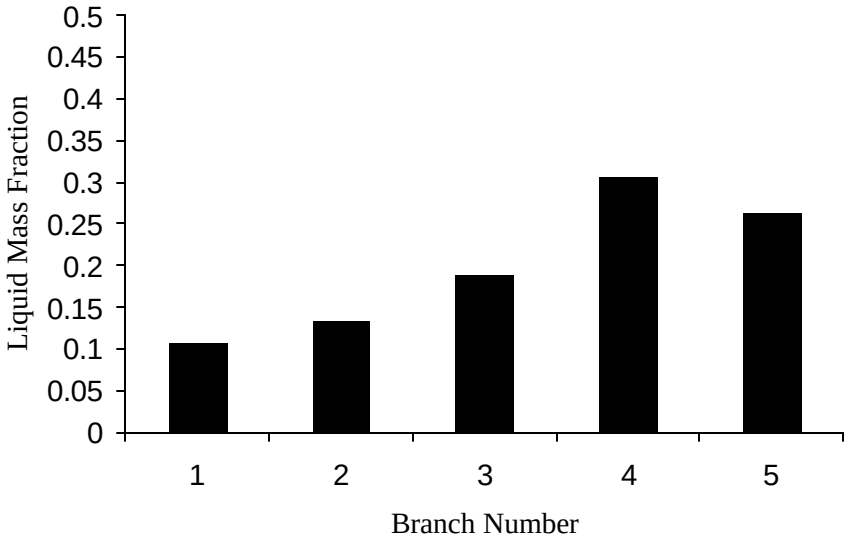

Figure 2.3.10: Distribution Results for 15 g/s, 10% Quality with Atomizer Inlet

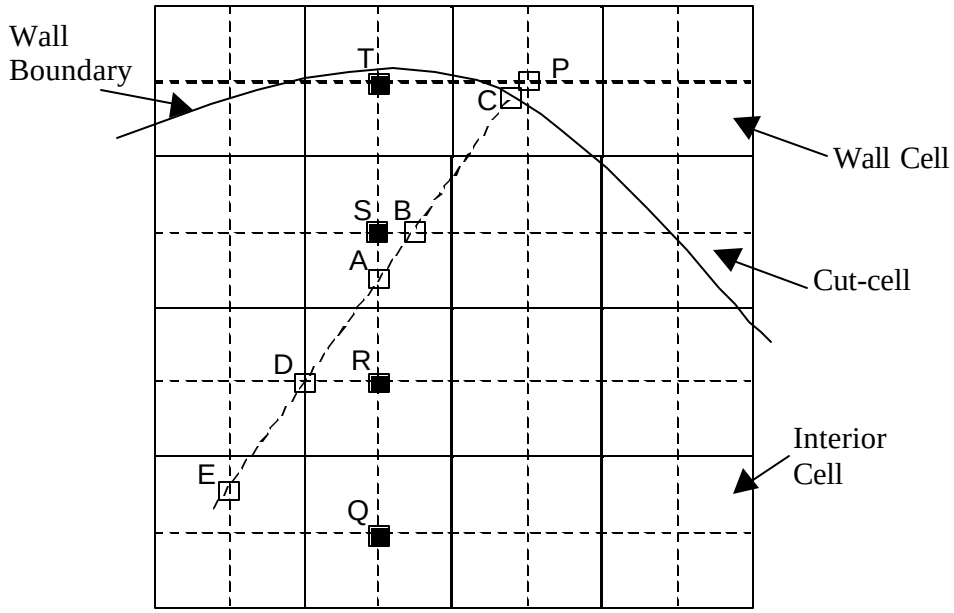

Figure 3.3.1: Example of Wall Boundary in Cut-Cell Logic

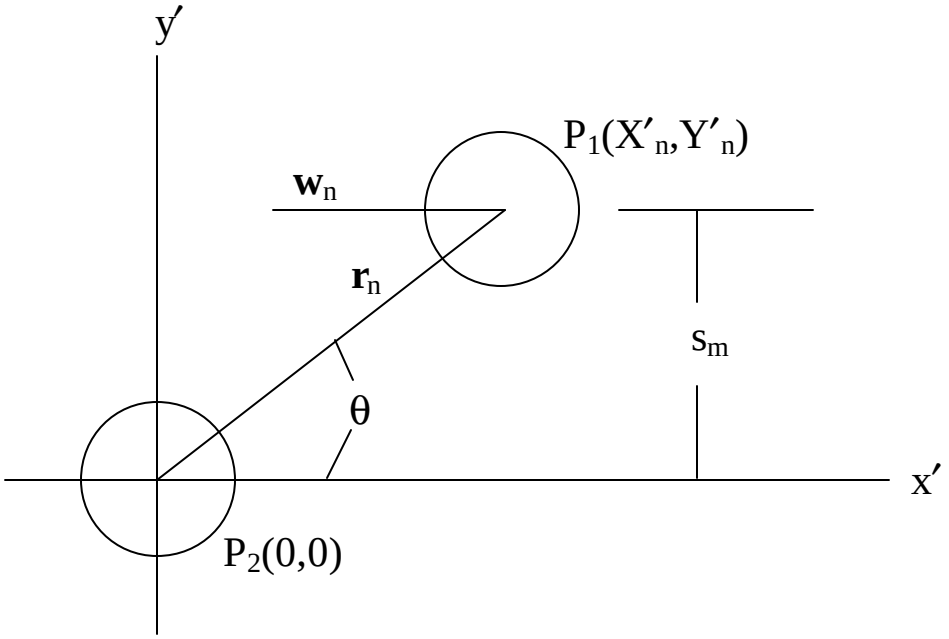

Figure 4.3.1: Schematic of Colliding Particles

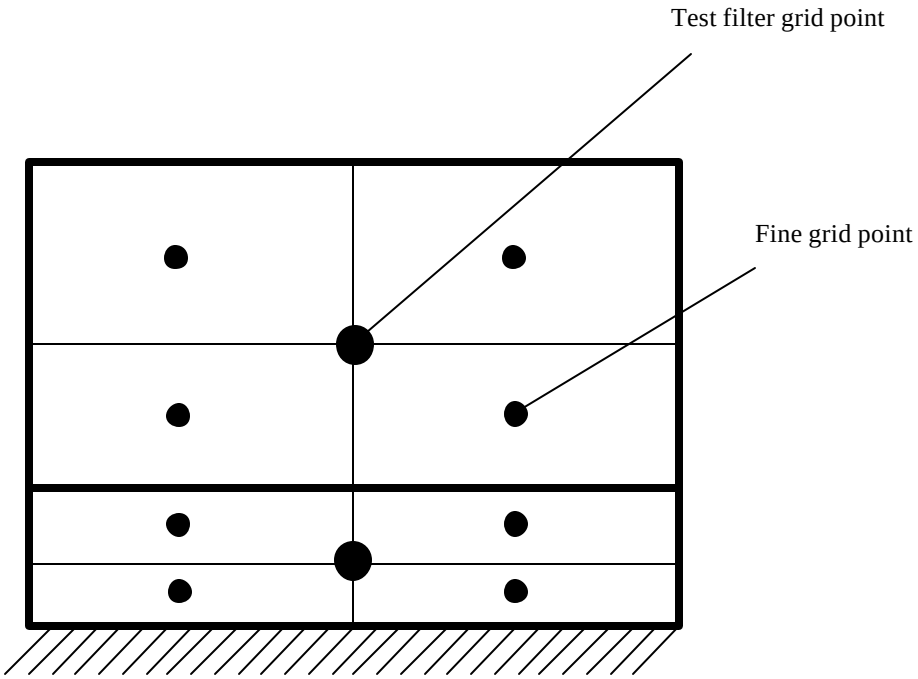

Figure 4.4.1: Dynamic Model Grid Logic, 2-Dimensional

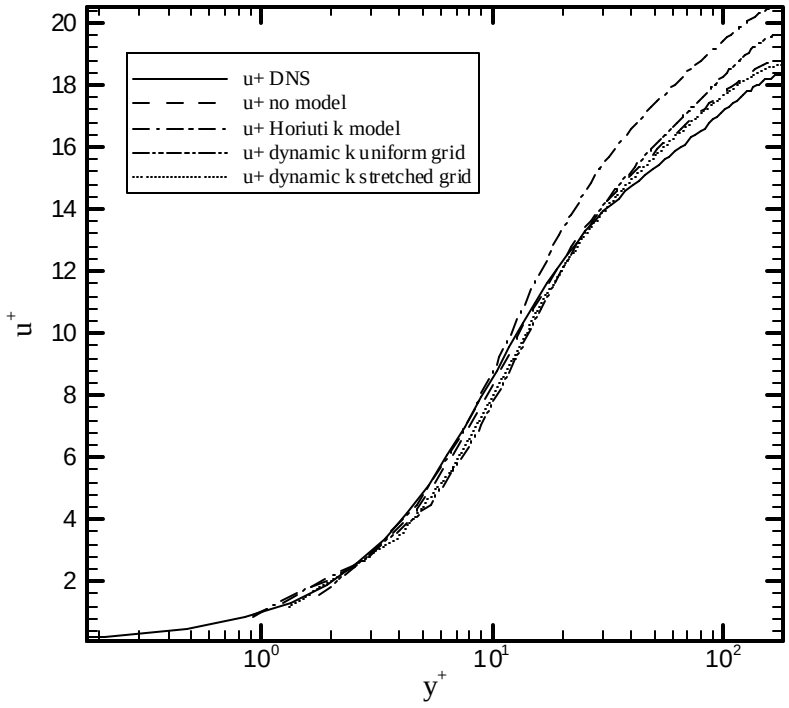

Figure 4.4.1.1: Mean Velocity Profiles, Channel Flow, $Re_\tau = 180$

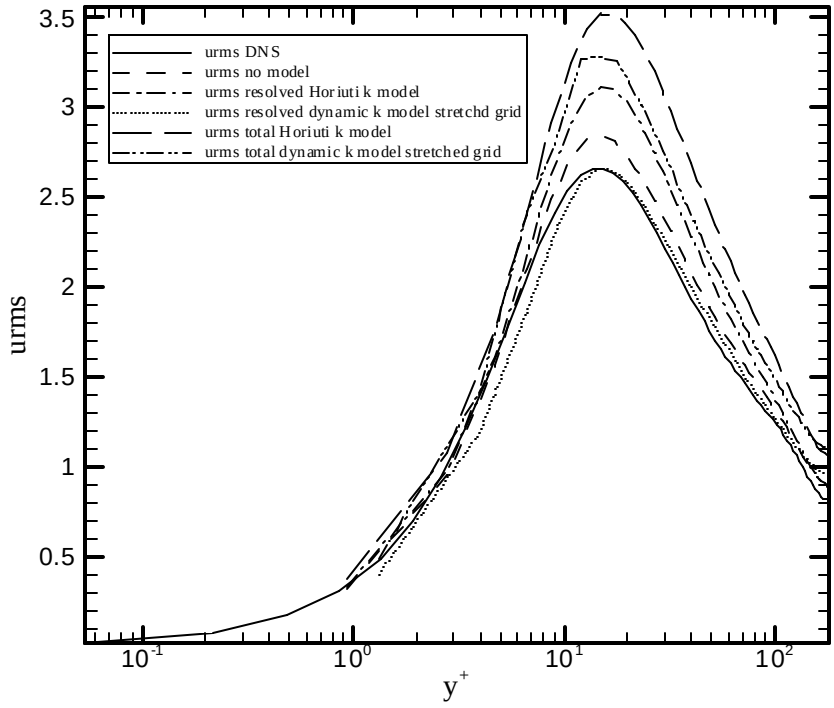

Figure 4.4.1.2: urms, Channel Flow, Re_τ=180

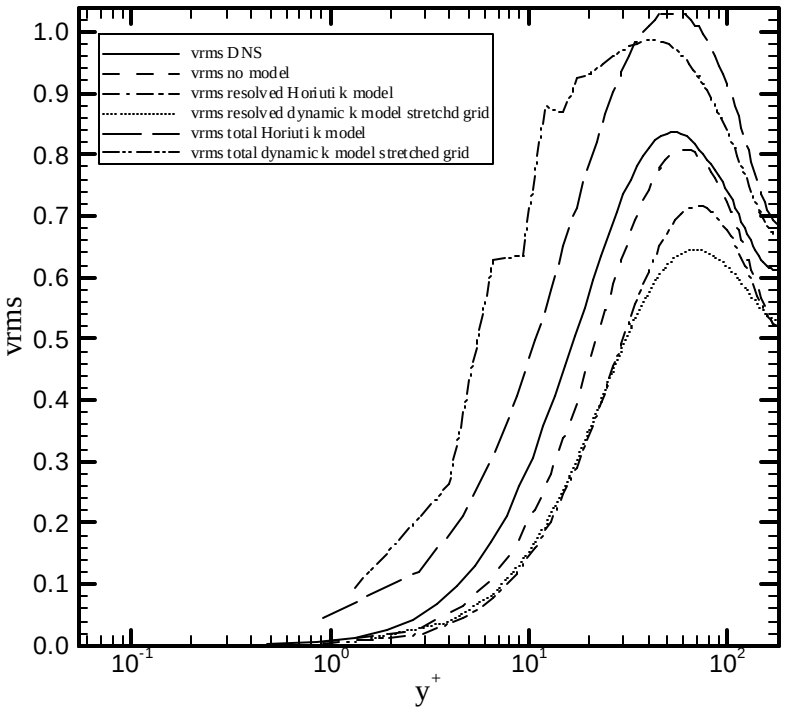

Figure 4.4.1.3: vrms, Channel Flow, Re_τ=180

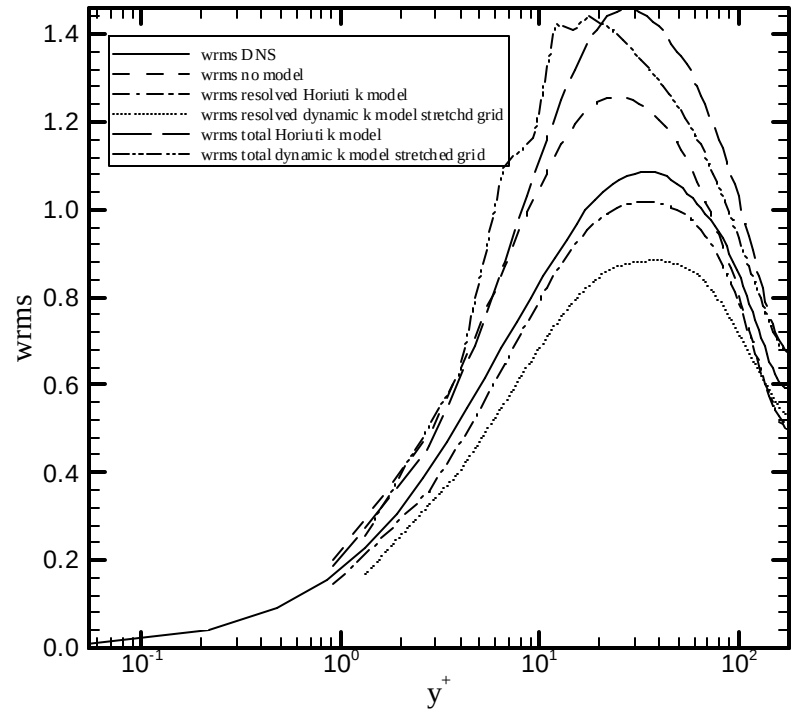

Figure 4.4.1.4: wrms, Channel Flow, Re_τ=180

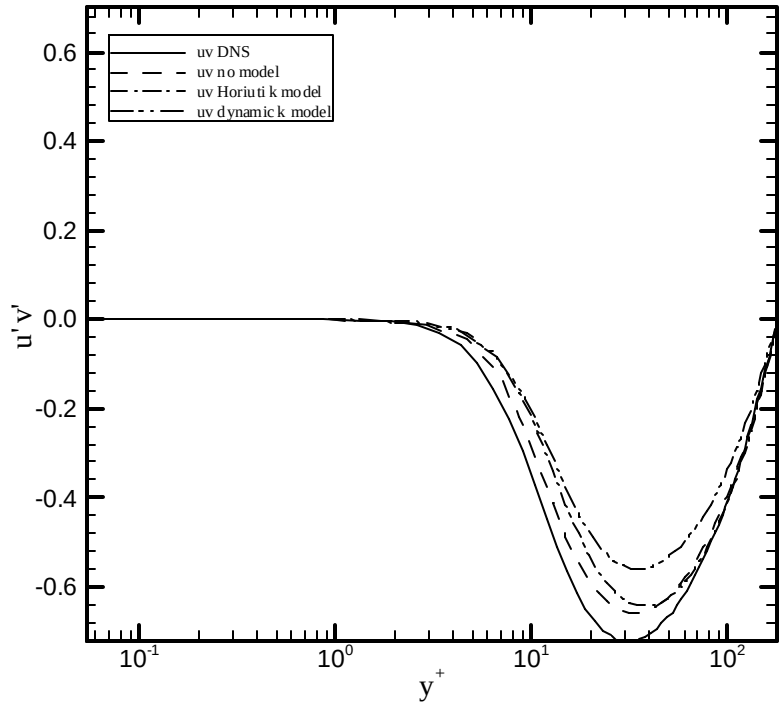

Figure 4.4.1.5: u′v′, Channel Flow, Re_τ=180

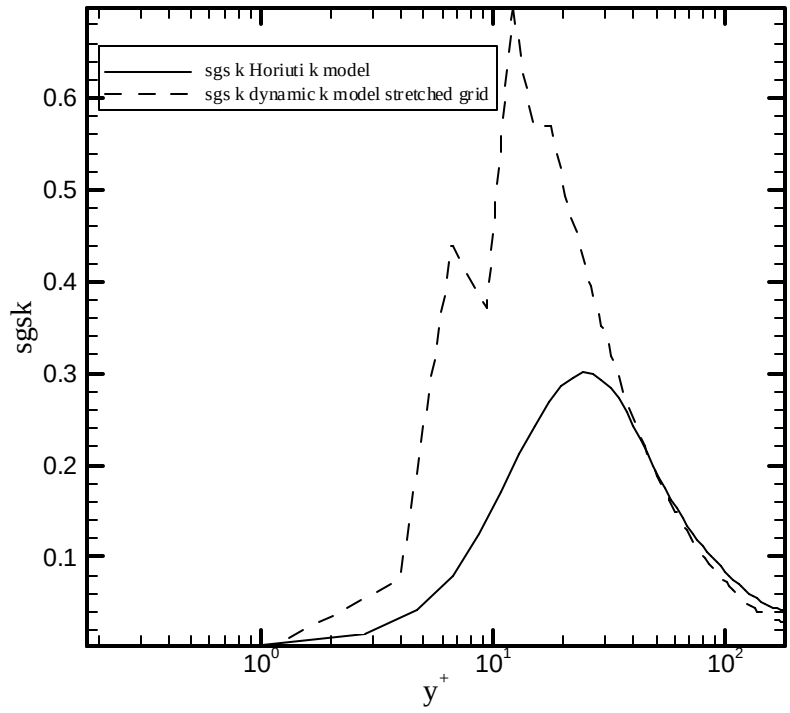

Figure 4.4.1.6: Mean sgs k, Channel Flow, Re_τ=180

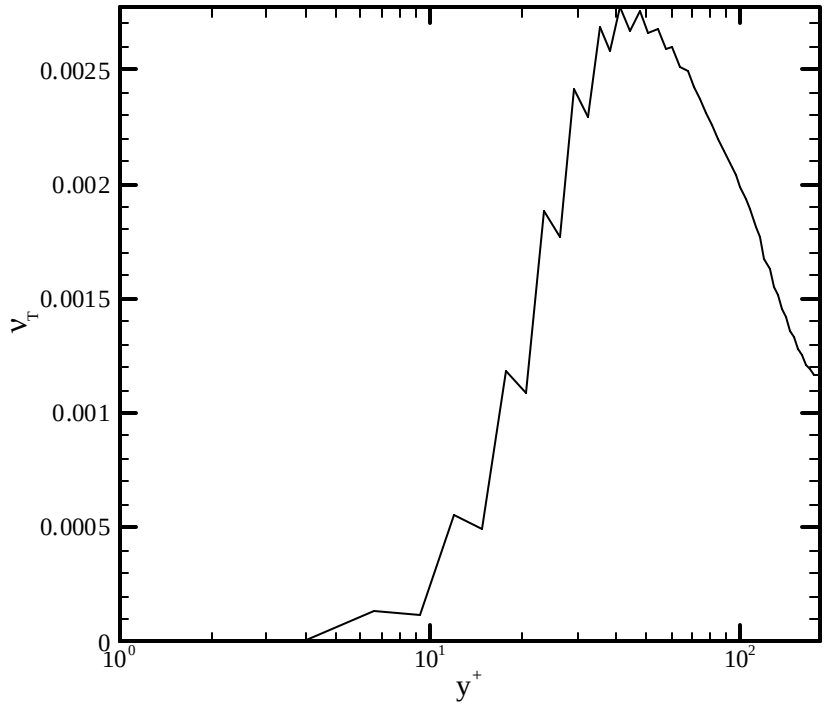

Figure 4.4.1.7: Mean ν_T, Channel Flow, Re_τ=180

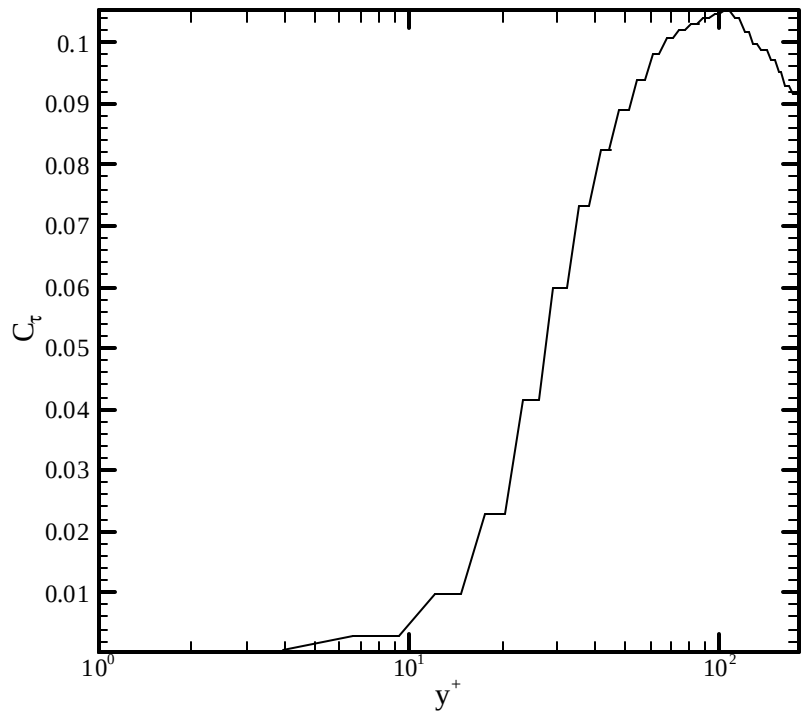

Figure 4.4.1.8: Mean C_τ, Channel Flow, Re_τ=180

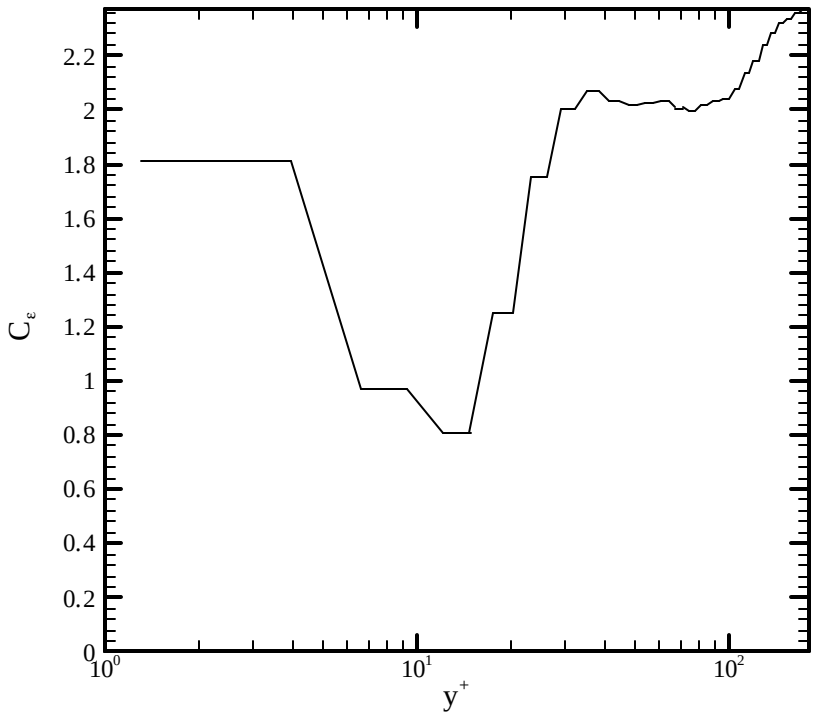

Figure 4.4.1.9: Mean C_ε, Channel Flow, Re_τ=180

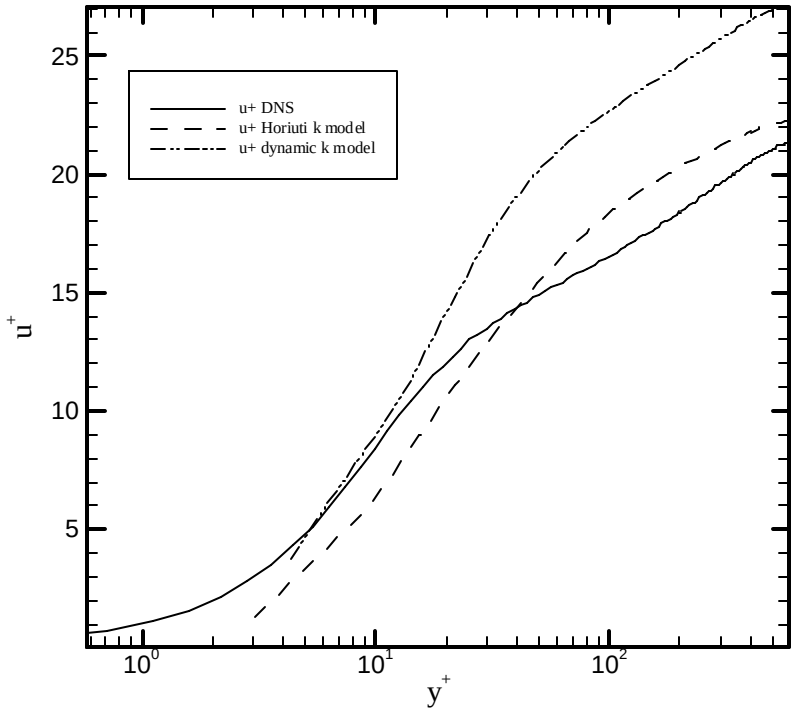

Figure 4.4.2.1: Mean Velocity Profiles, Channel Flow, $Re_\tau = 590$

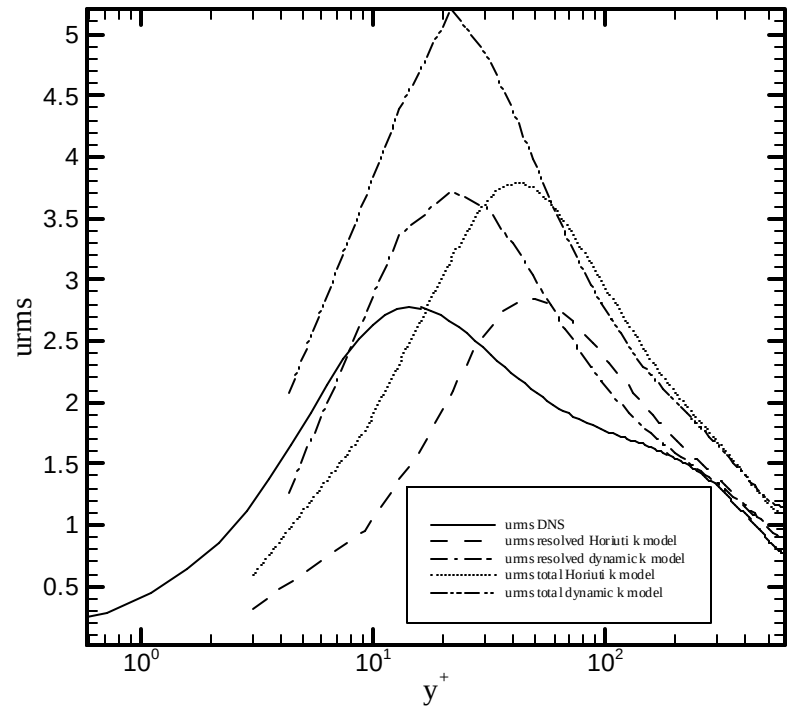

Figure 4.4.2.2: urms, Channel Flow, $Re_\tau = 590$

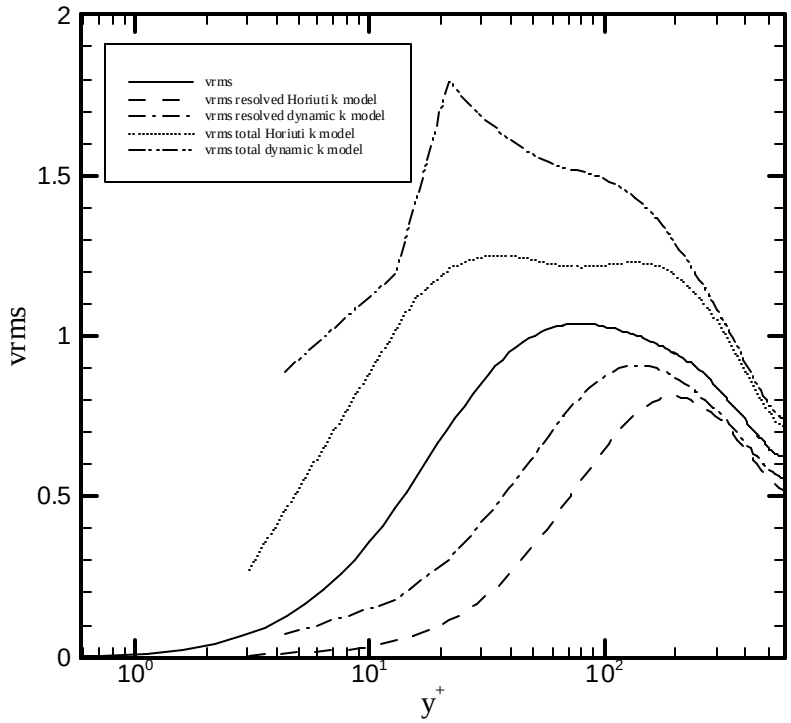

Figure 4.4.2.3: vrms, Channel Flow, $Re_\tau = 590$

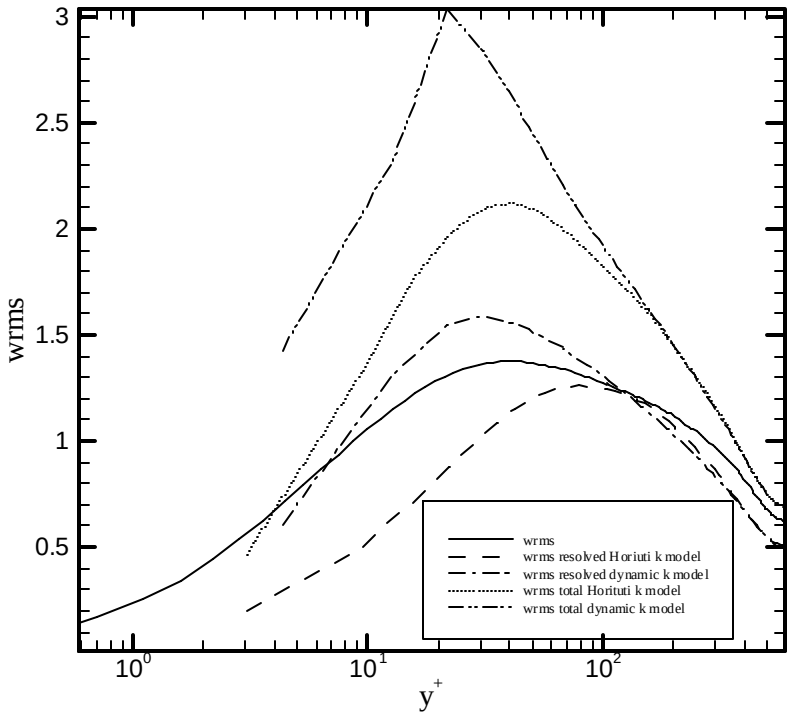

Figure 4.4.2.4: wrms, Channel Flow, $Re_\tau = 590$

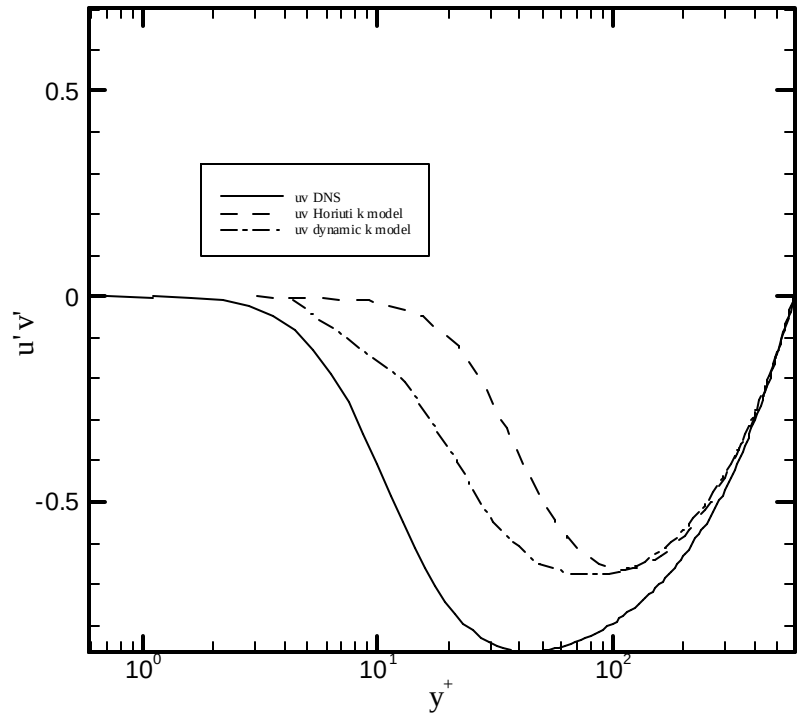

Figure 4.4.2.5: u′v′, Channel Flow, Re_τ=590

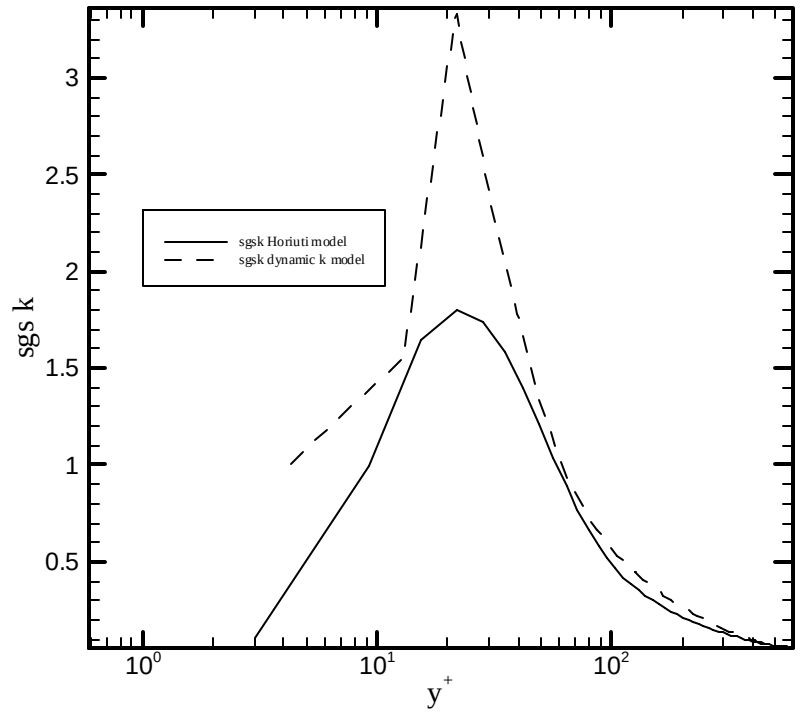

Figure 4.4.2.6: sgsk, Channel Flow, Re_τ=590

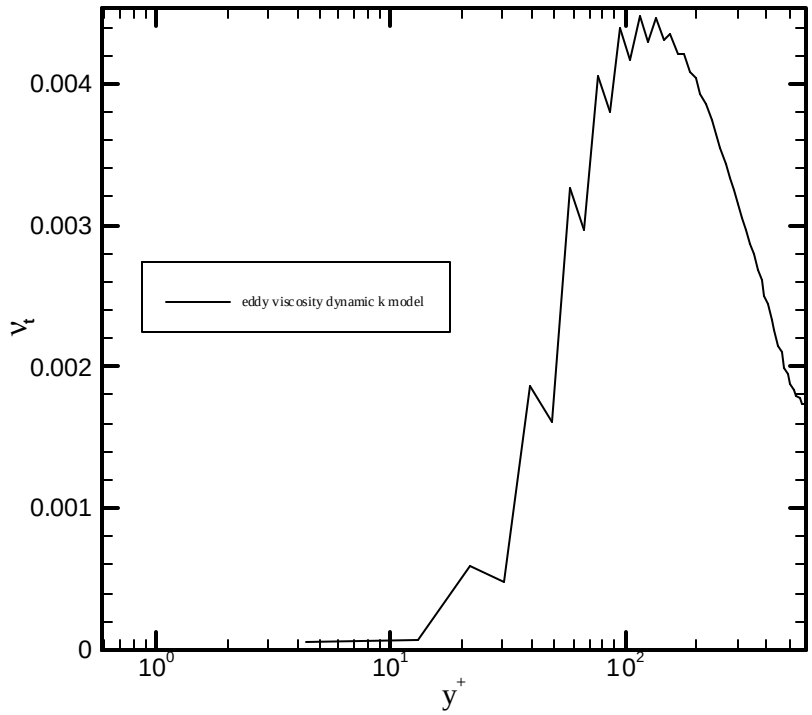

Figure 4.4.2.7: Mean ν_T, Channel Flow, Re_τ=590

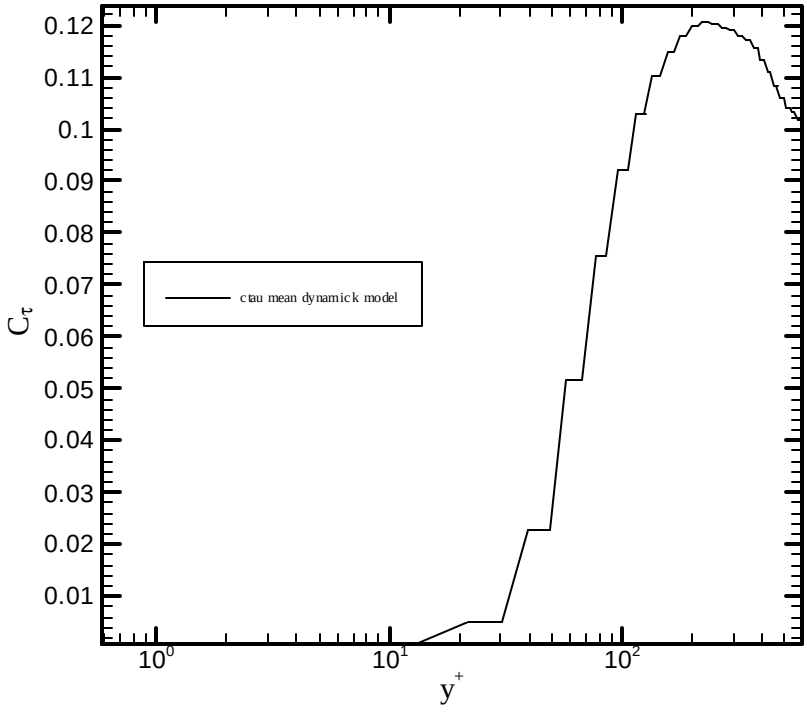

Figure 4.4.2.8: Mean C_τ, Channel Flow, Re_τ=590

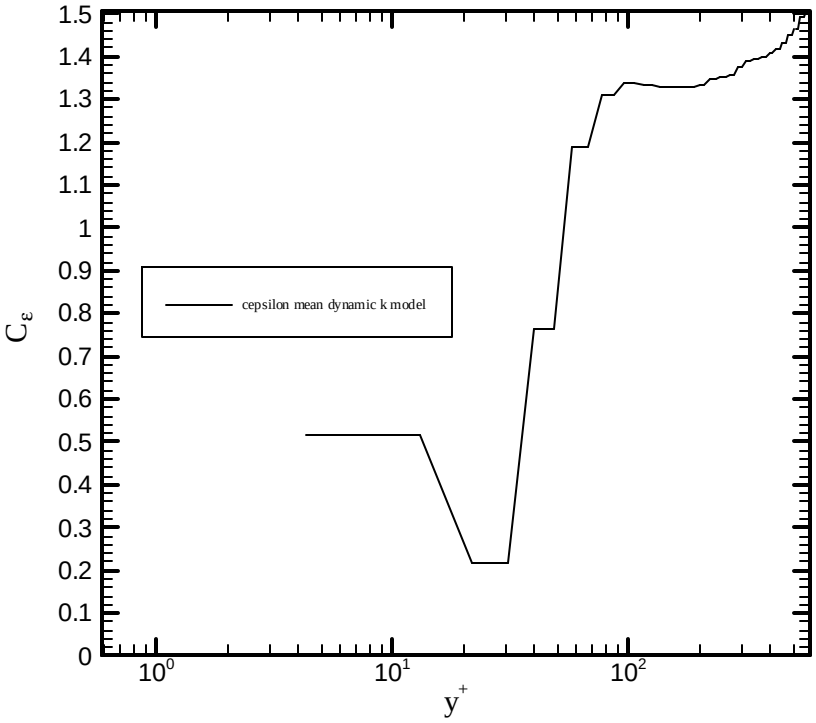

Figure 4.4.2.9: Mean C_ε, Channel Flow, Re_τ=590

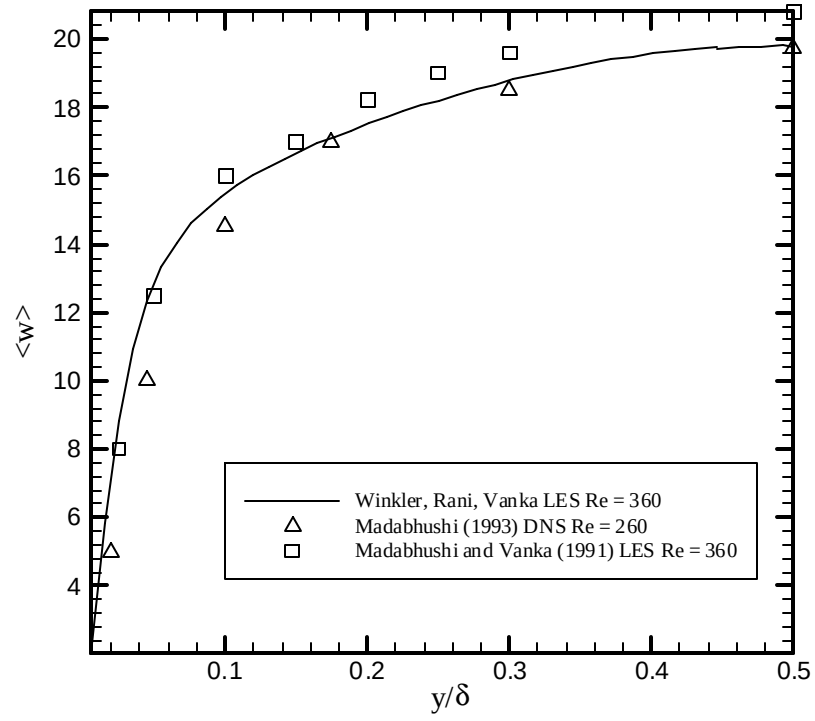

Figure 5.0.1: Comparison of Mean Streamwise Velocity at x = 0.5

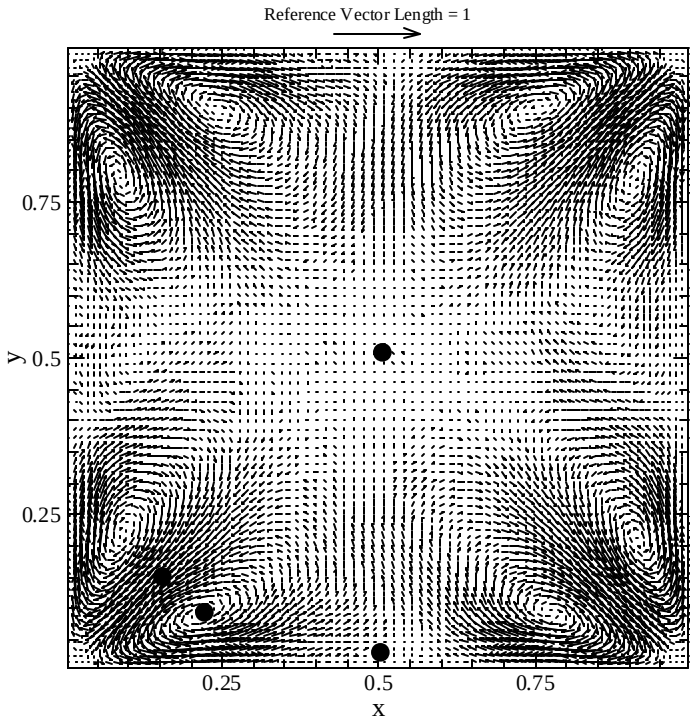

Figure 5.0.2: Sampling Positions in Square Duct Cross-Section

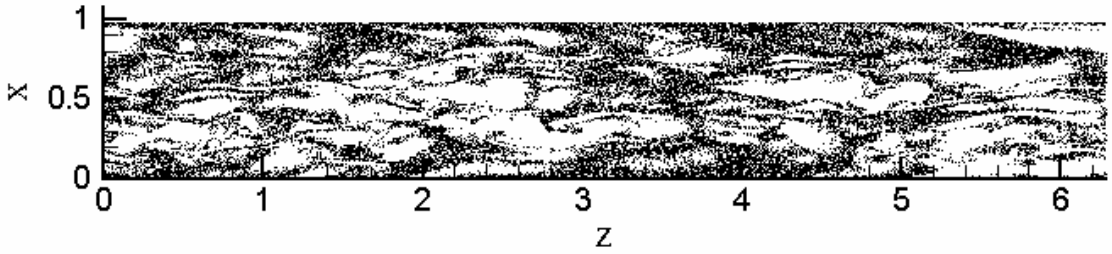

Figure 5.1.1: Instantaneous Scatter Plot of Particle Positions for $\tau_p^+ = 0.25$, $7.05 \leq y^+ \leq 10.66$

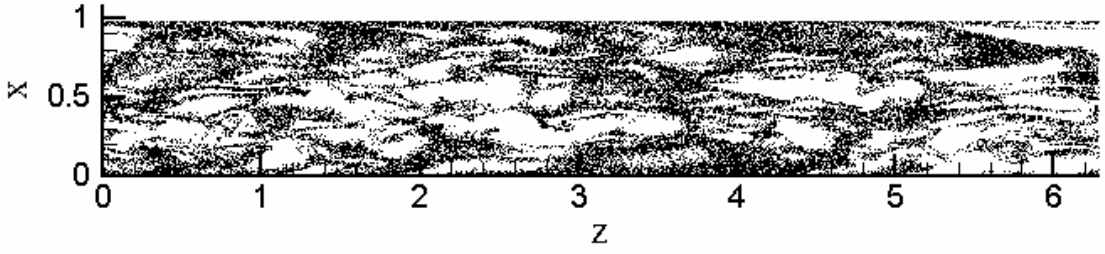

Figure 5.1.2: Instantaneous Scatter Plot of Particle Positions for $\tau_p^+ = 1.0$, $7.05 \leq y^+ \leq 10.66$

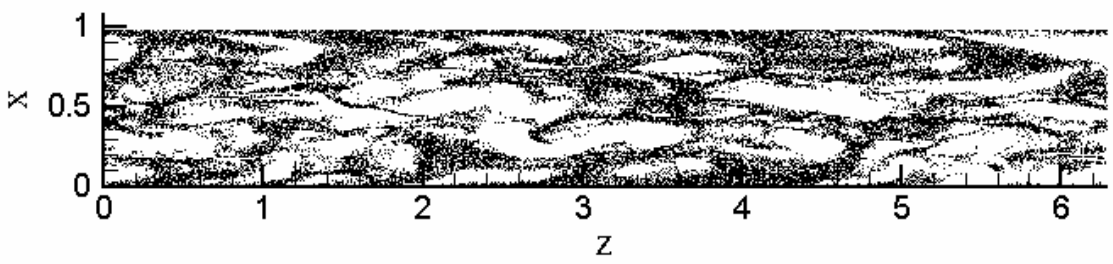

Figure 5.1.3: Instantaneous Scatter Plot of Particle Positions for $\tau_p^+ = 8.0$, $7.05 \le y^+ \le 10.66$

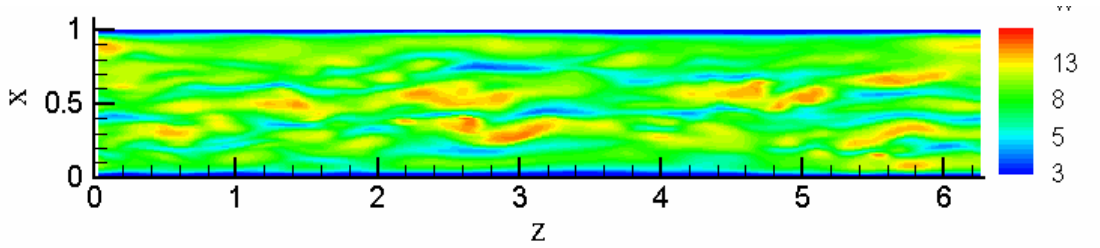

Figure 5.1.4: Instantaneous Contours of Streamwise Velocity at $y^+=8.85$

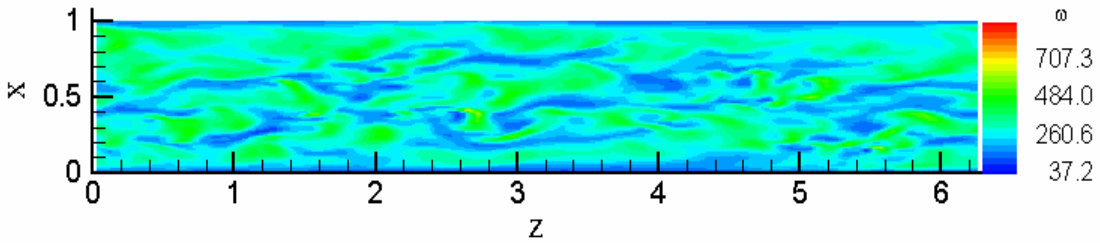

Figure 5.1.5: Instantaneous Contours of ? at $y^+=8.85$

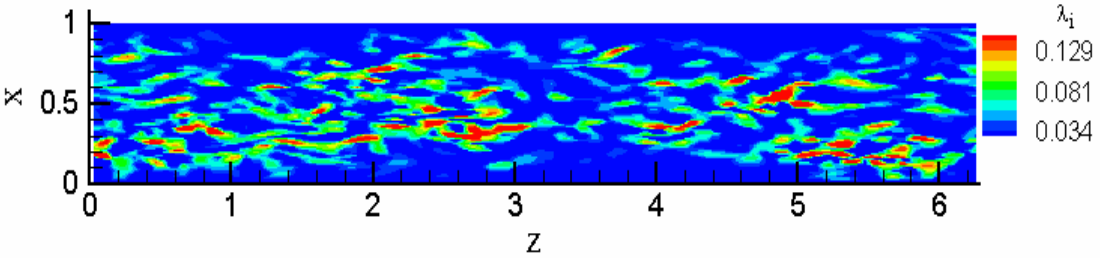

Figure 5.1.6: Instantaneous Contours of λ_i at $y^+=8.85$

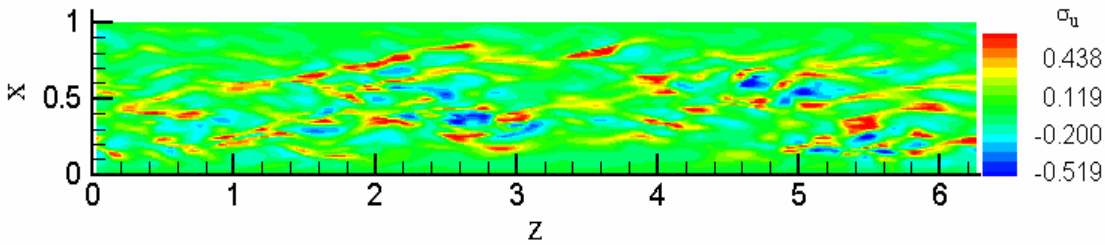

Figure 5.1.7: Instantaneous Contours of σ_u at $y^+=8.85$

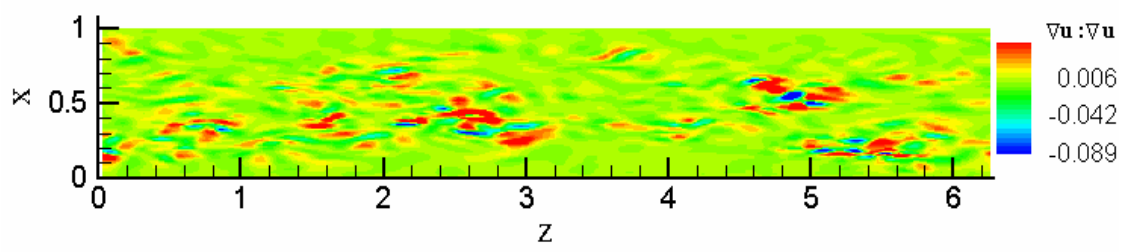

Figure 5.1.8: Instantaneous Contours of $\nabla\mathbf{u}:\nabla\mathbf{u}$ at $y^+=8.85$

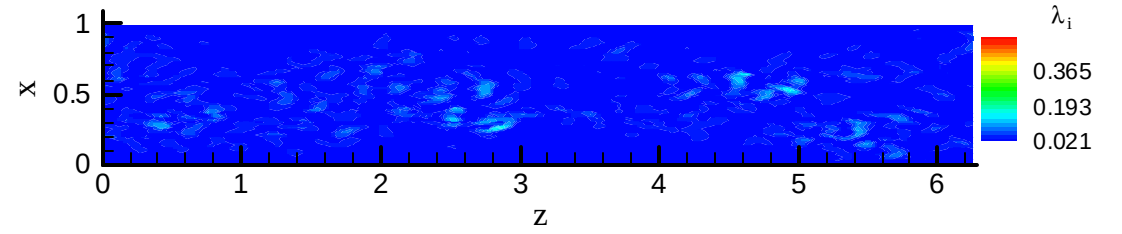

(a)

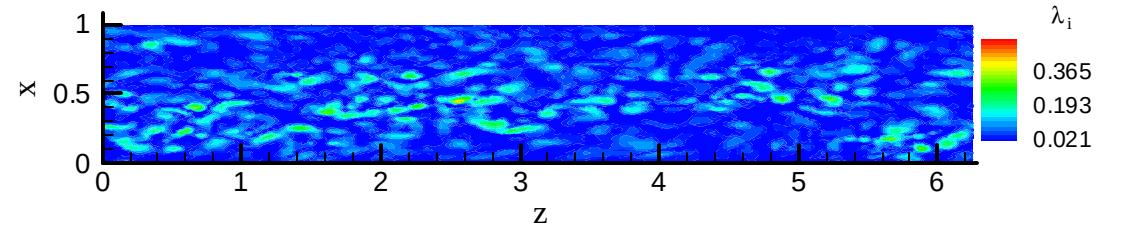

(b)

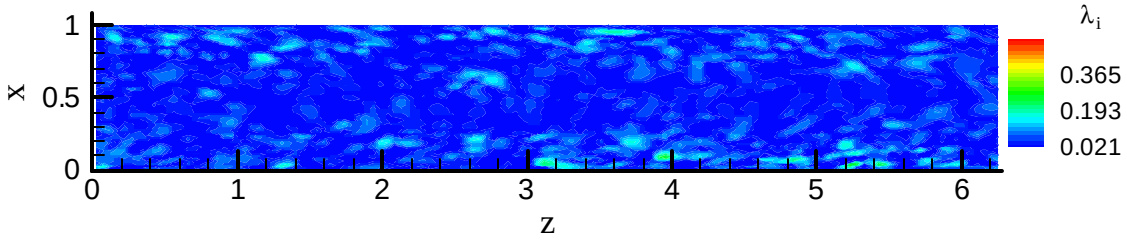

(c)

Figure 5.1.9: Contours of λ_i at y^+ = (a) 1.76, (b) 35.09, (c) 177.18

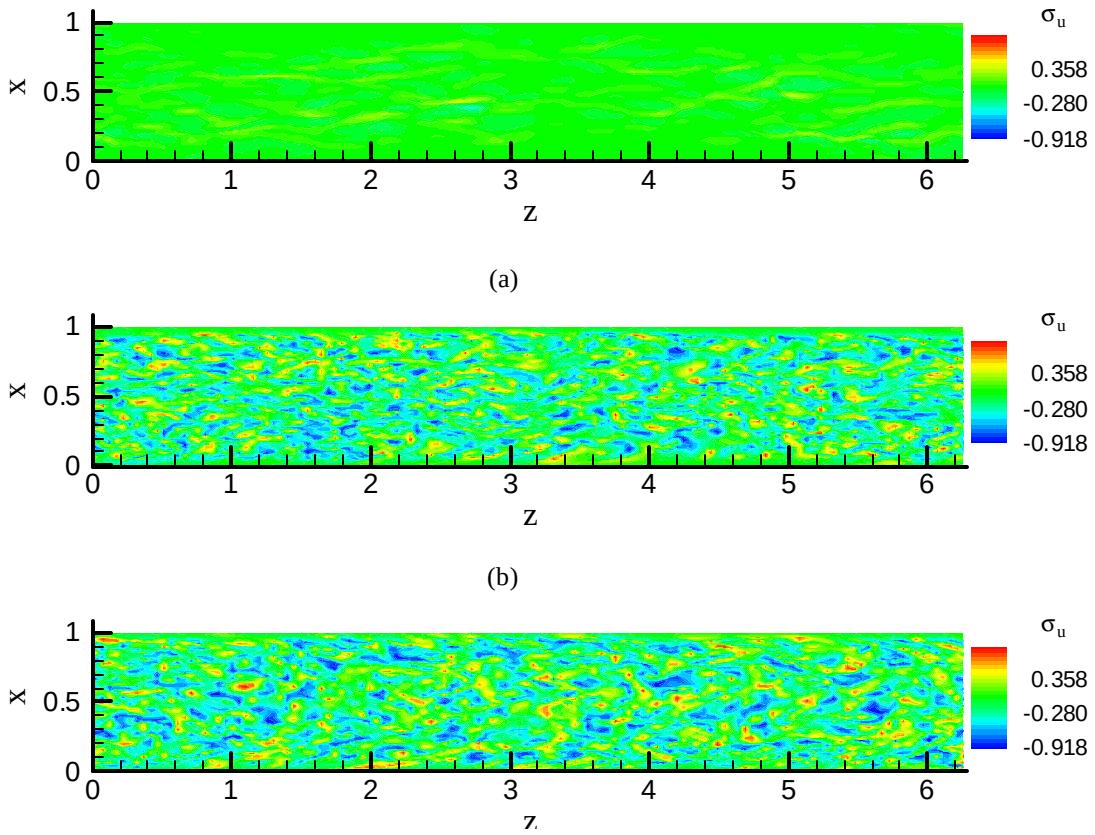

Figure 5.1.10: Contours of σ_u at y^+ = (a) 1.76, (b) 35.09, (c) 177.18

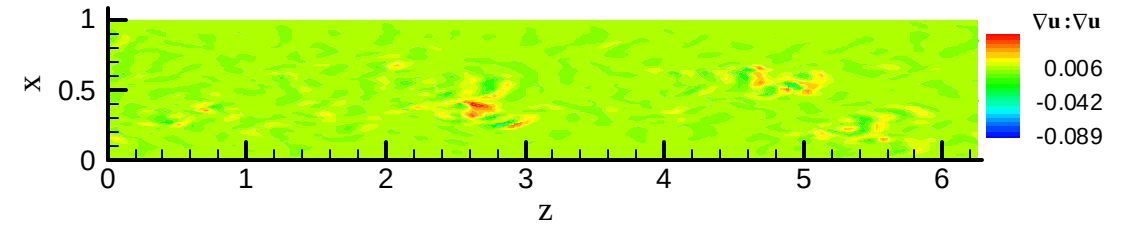

(a)

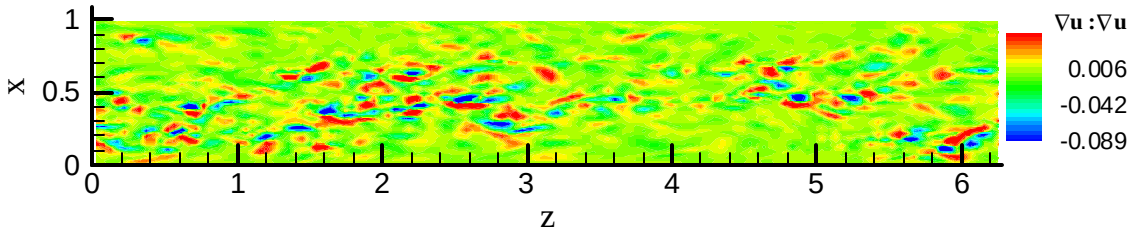

(b)

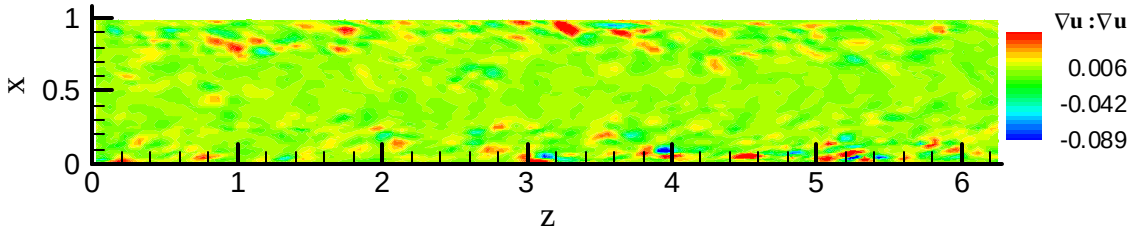

(c)

Figure 5.1.11: Contours of $\nabla\mathbf{u}:\nabla\mathbf{u}$ at y^+ = (a) 1.76, (b) 35.09, (c) 177.18

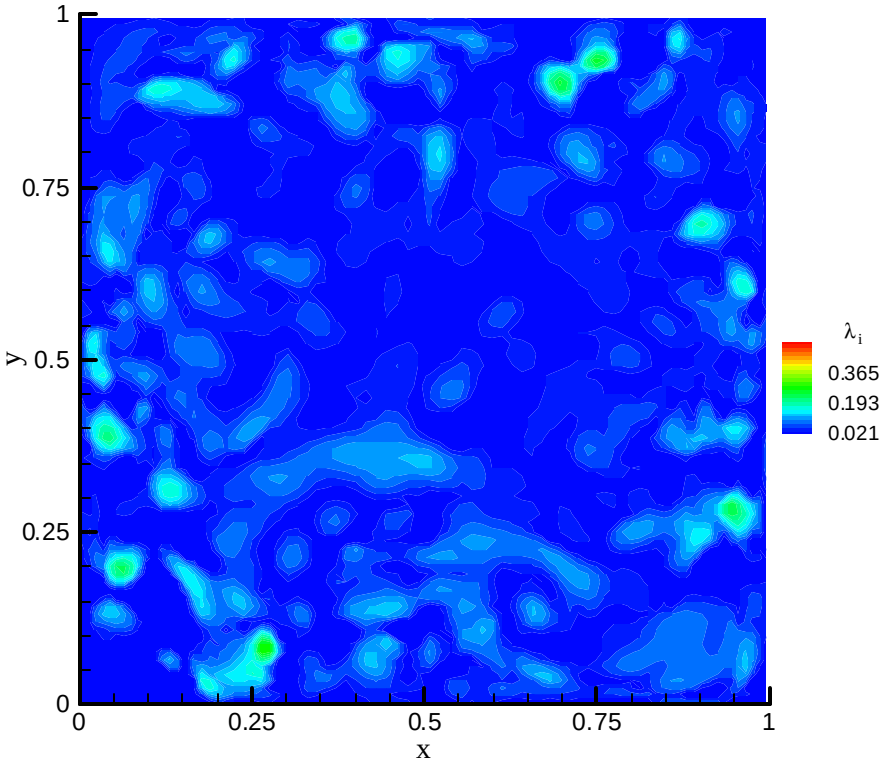

Figure 5.1.12: Instantaneous Cross-Sectional Contours of λ_i

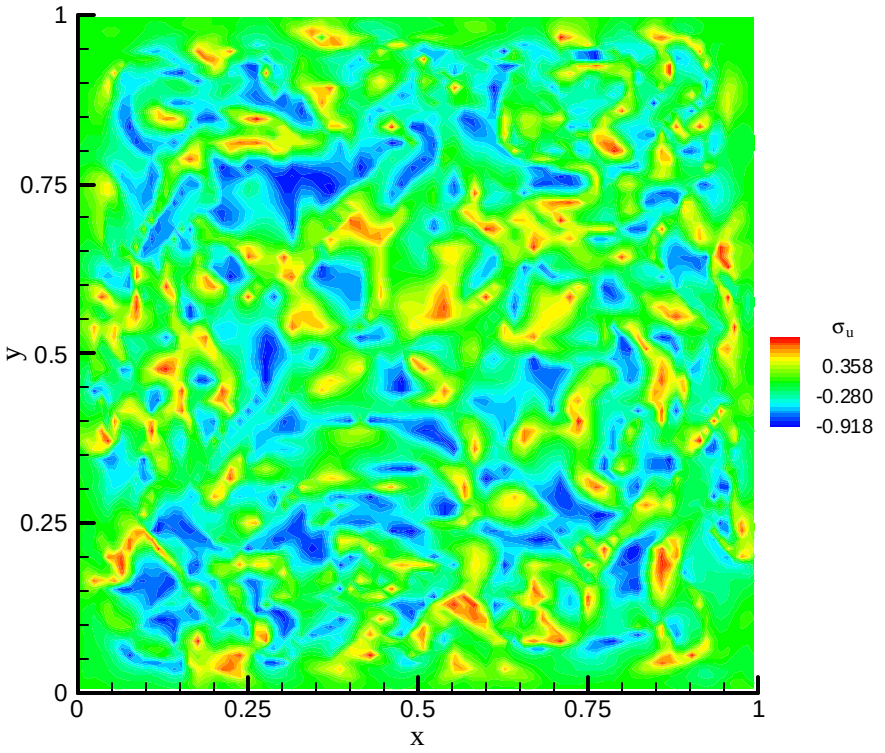

Figure 5.1.13: Instantaneous Cross-Sectional Contours of σ_u

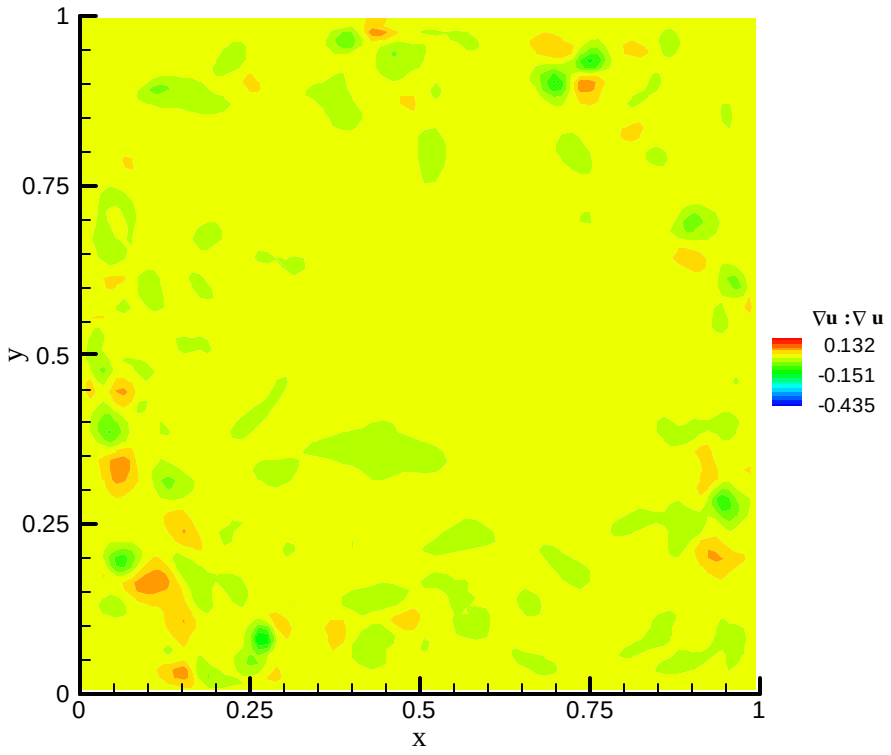

Figure 5.1.14: Instantaneous Cross-Sectional Contours of $\nabla \mathbf{u} : \nabla \mathbf{u}$

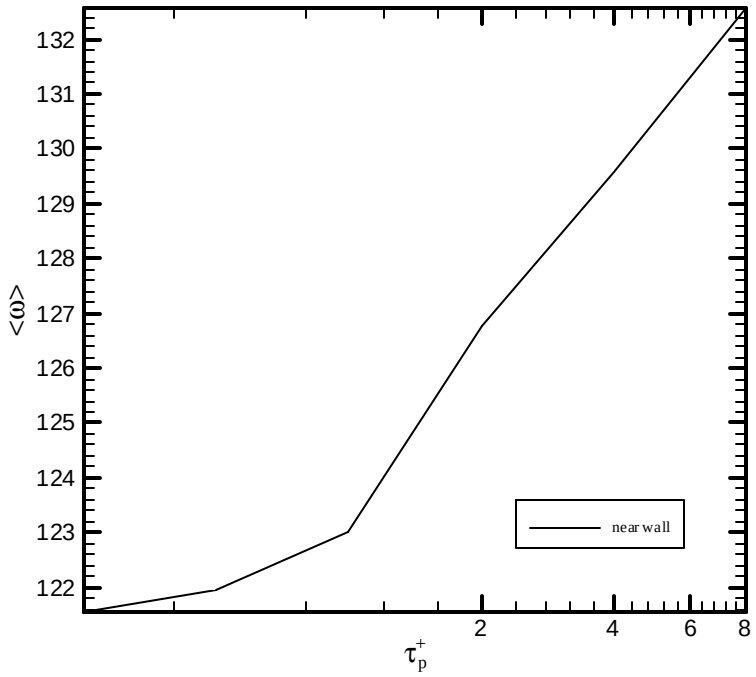

Figure 5.2.1: Mean Values of ω in the Near Wall Region (x^+=177.2, y^+=19.8)

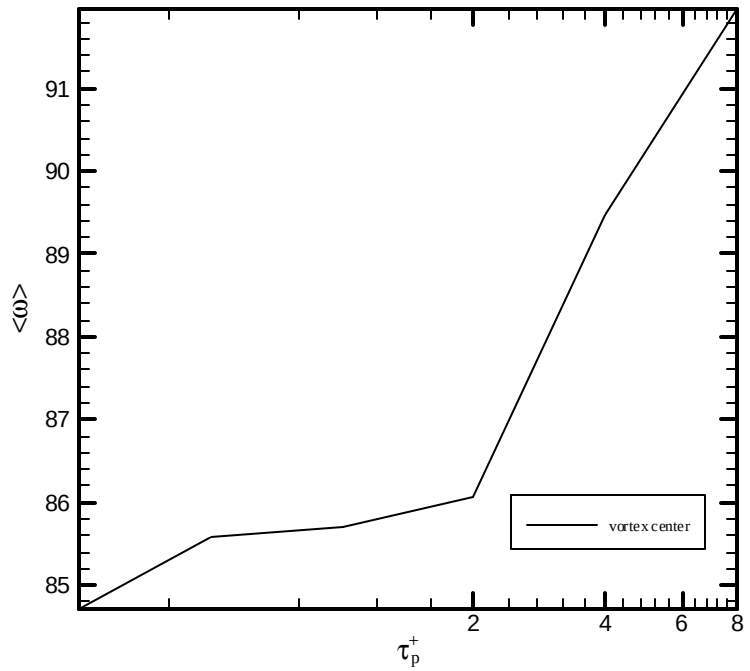

Figure 5.2.2: Mean Values of ω in the Vortex Center Region (x^+=76.7, y^+=31.2)

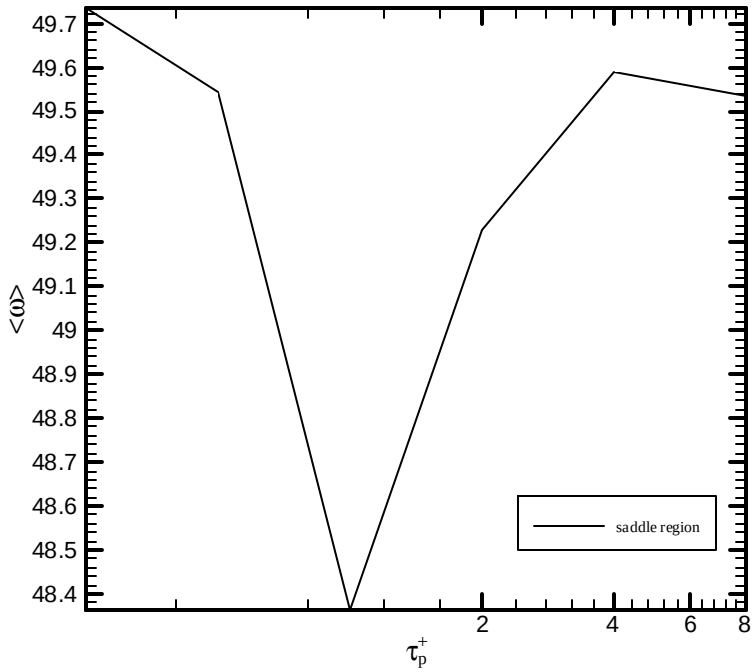

Figure 5.2.3: Mean Values of ω in the Saddle Region (x^+=59.5, y^+=59.5)

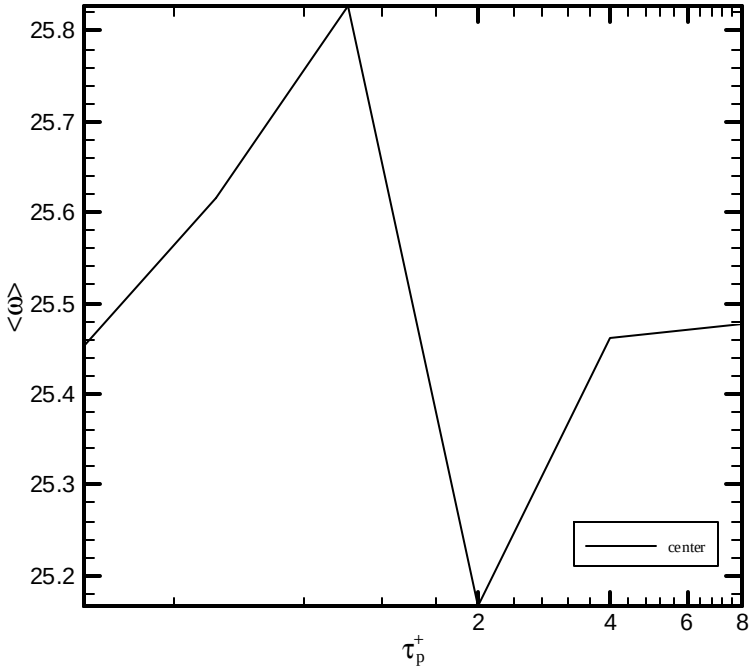

Figure 5.2.4: Mean Values of ω in the Duct Center Region (x^+=177.2, y^+=177.2)

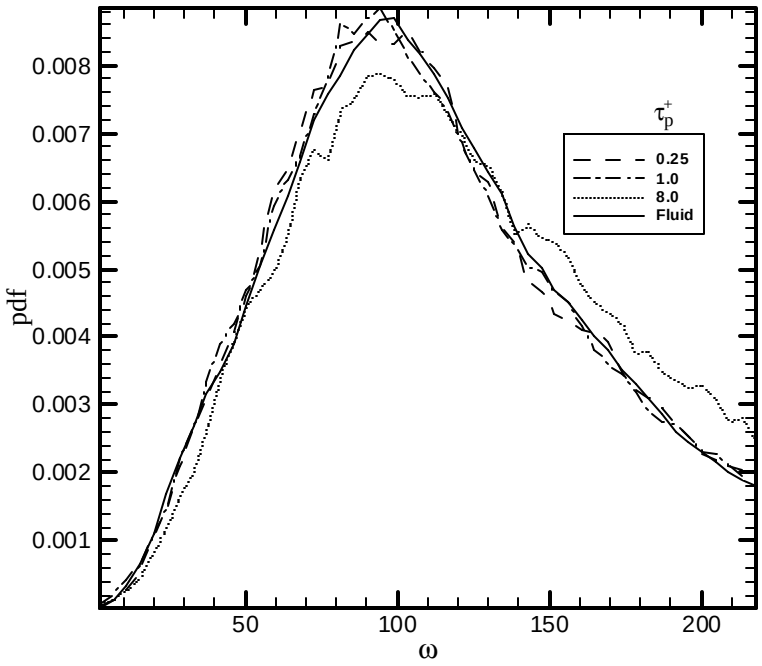

Figure 5.2.5: PDFs of ω in the Near Wall Region (x^+=177.2, y^+=19.8)

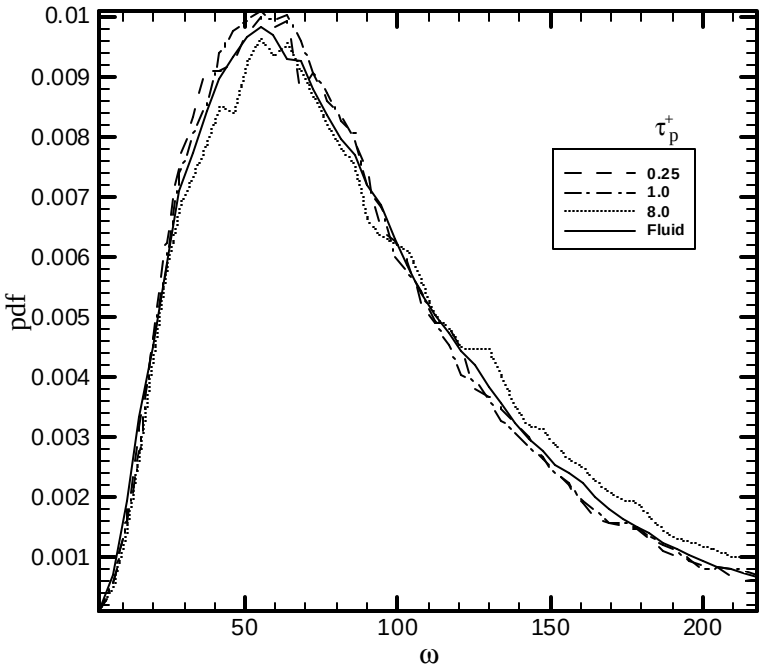

Figure 5.2.6: PDFs of ω in the Vortex Center Region (x^+=76.7, y^+=31.2)

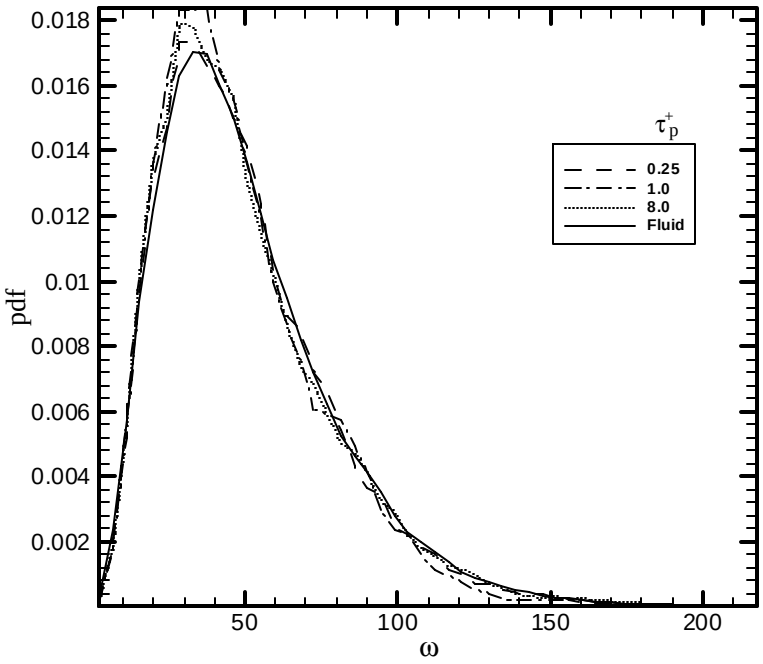

Figure 5.2.7: PDFs of ω in the Saddle Region (x^+=59.5, y^+=59.5)

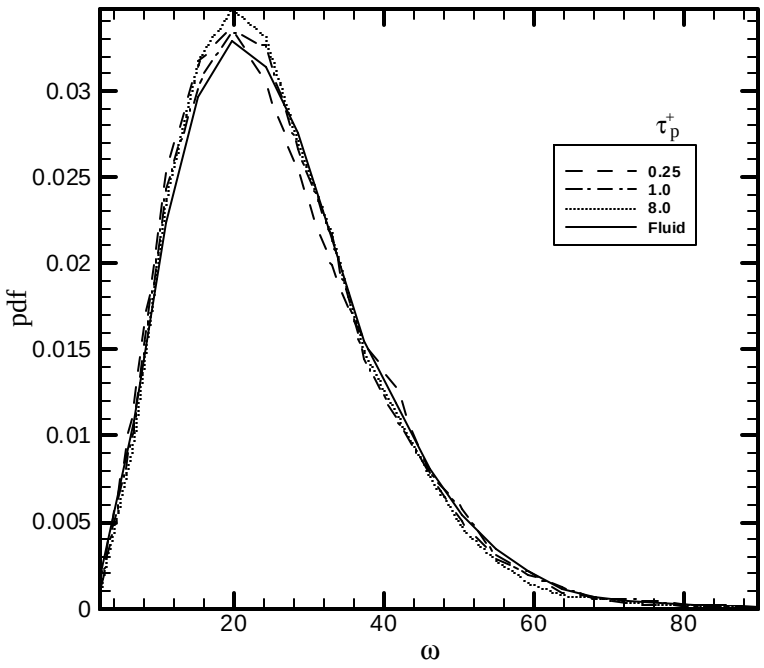

Figure 5.2.8: PDFs of ω in the Duct Center Region (x^+=177.2, y^+=177.2)

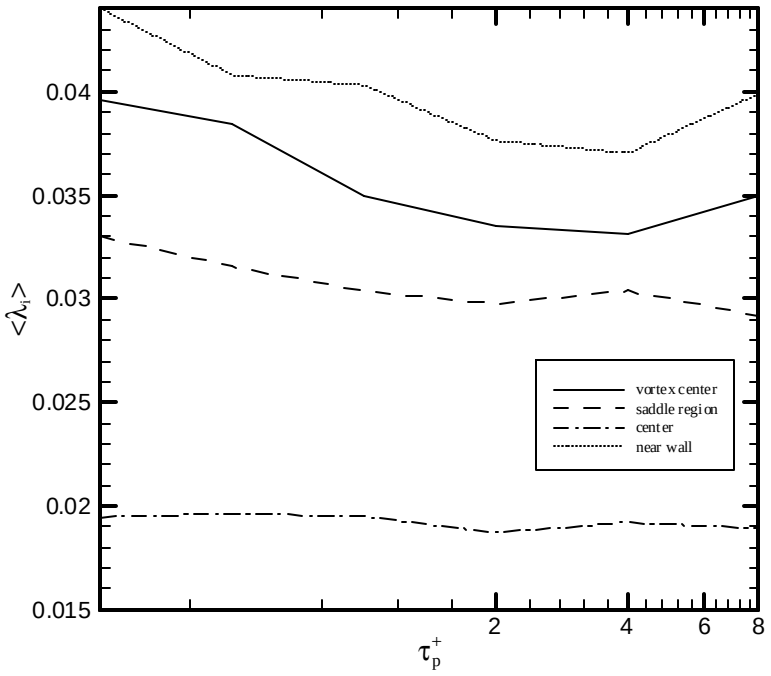

Figure 5.3.1: Mean Values of λ_i

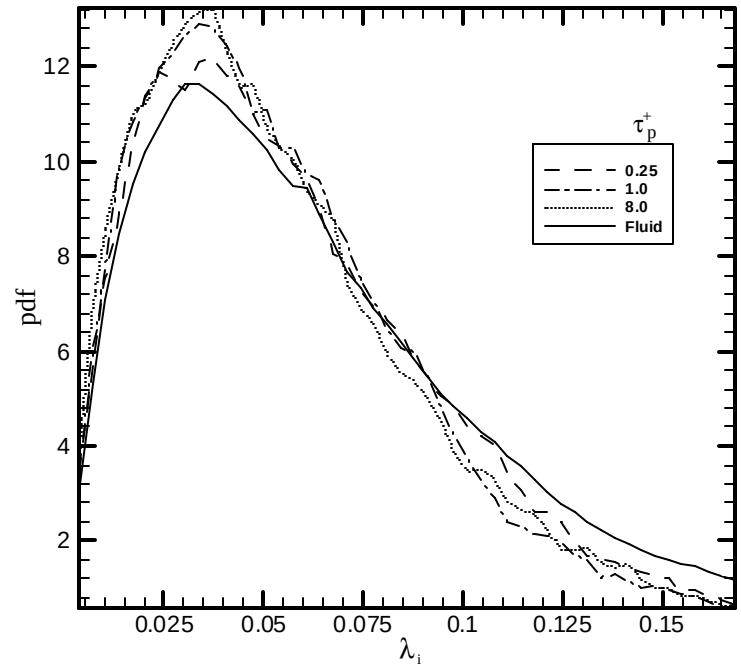

Figure 5.3.2: PDFs of λ_i in the Near Wall Region (x^+=177.2, y^+=19.8)

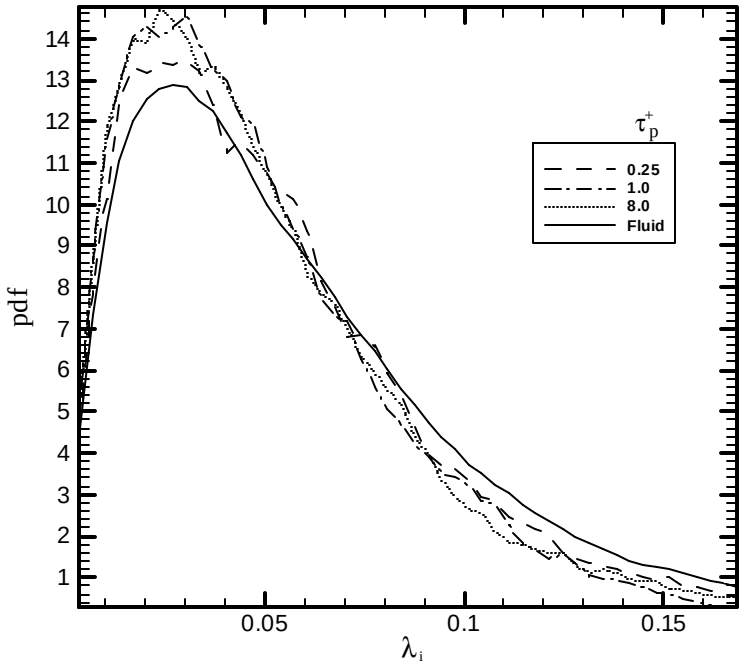

Figure 5.3.3: PDFs of λ_i in the Vortex Center Region (x^+=76.7, y^+=31.2)

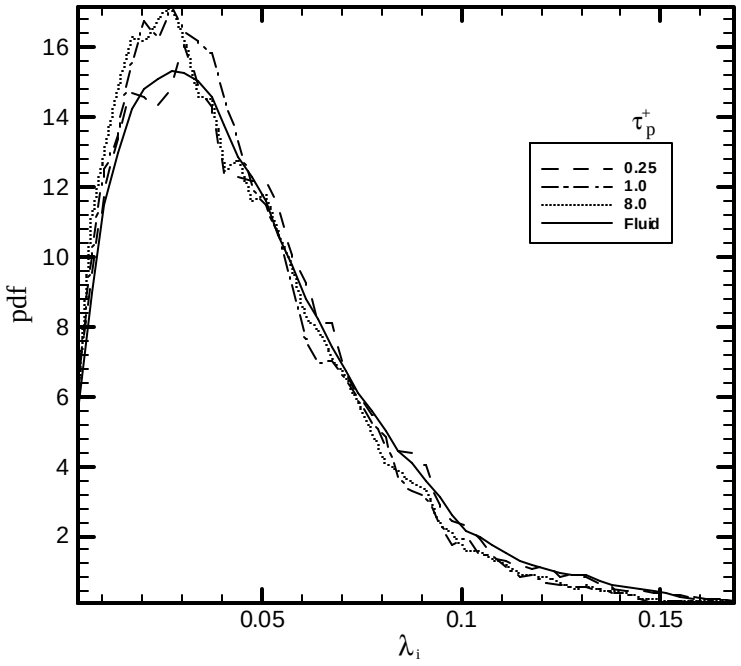

Figure 5.3.4: PDFs of λ_i in the Saddle Region (x^+=59.5, y^+=59.5)

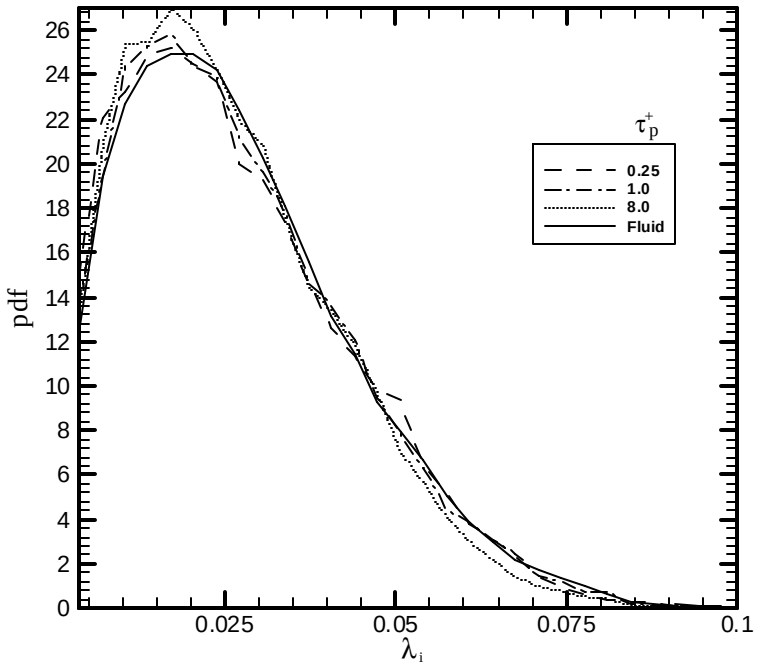

Figure 5.3.5: PDFs of λ_i in the Duct Center Region (x^+=177.2, y^+=177.2)

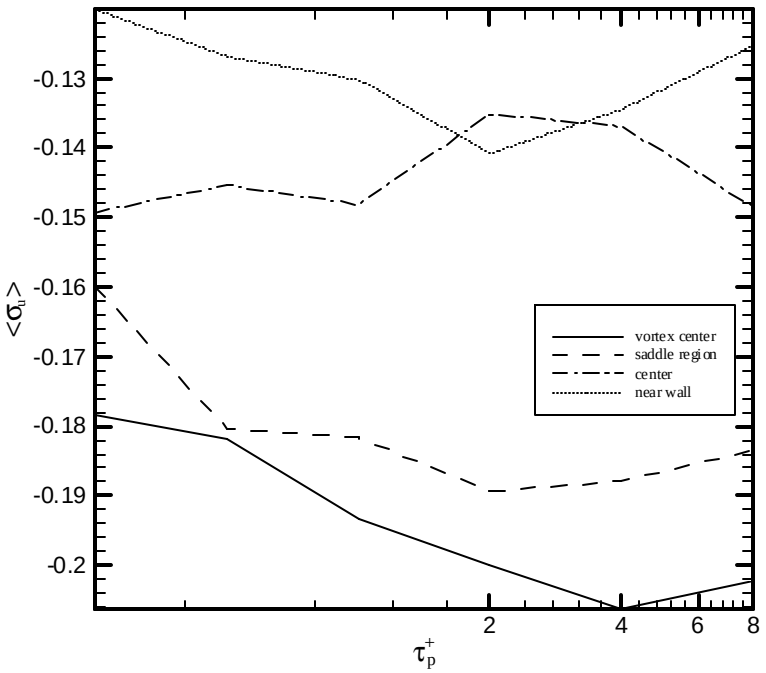

Figure 5.4.1: Mean Values of σ_u

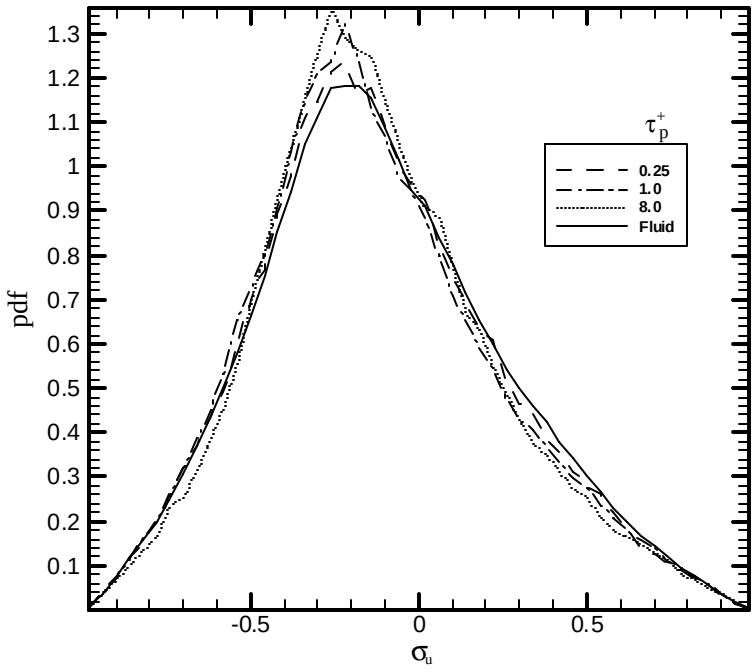

Figure 5.4.2: PDFs of σ_u in the Near Wall Region (x^+=177.2, y^+=19.8)

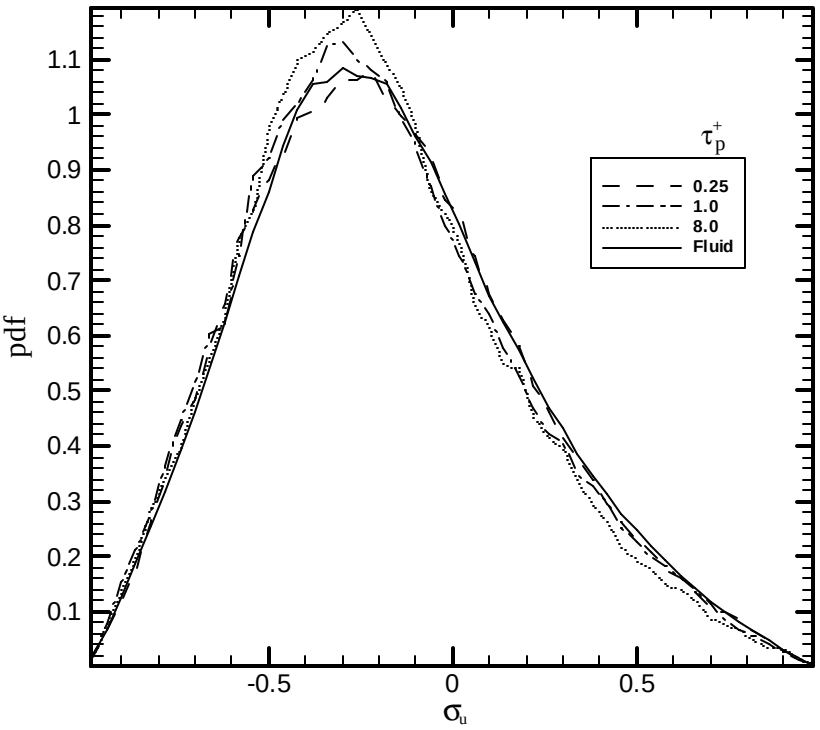

Figure 5.4.3: PDFs of σ_u in the Vortex Center Region (x^+=76.7, y^+=31.2)

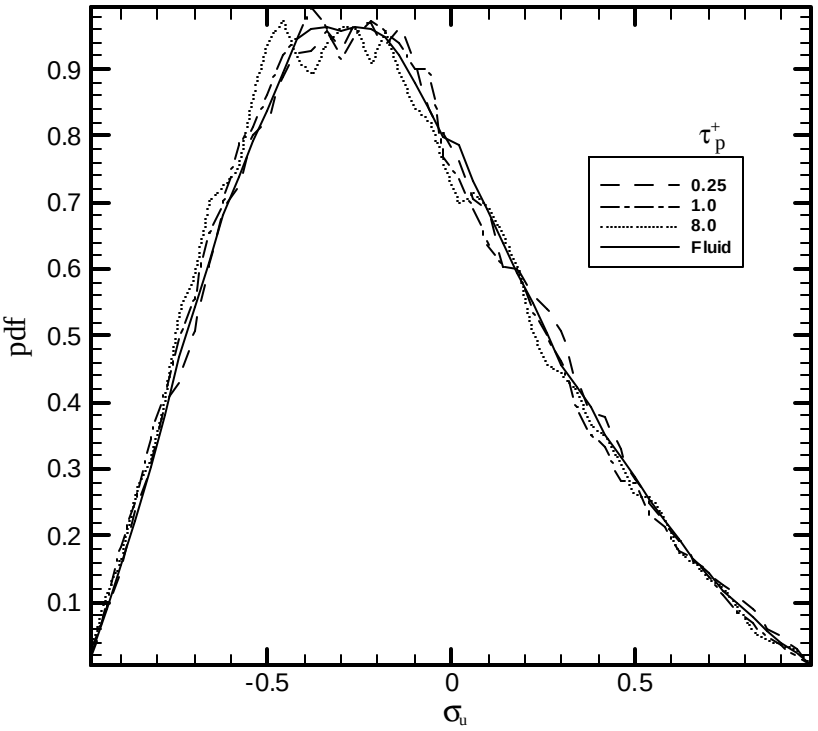

Figure 5.4.4: PDFs of σ_u in the Saddle Region (x^+=59.5, y^+=59.5)

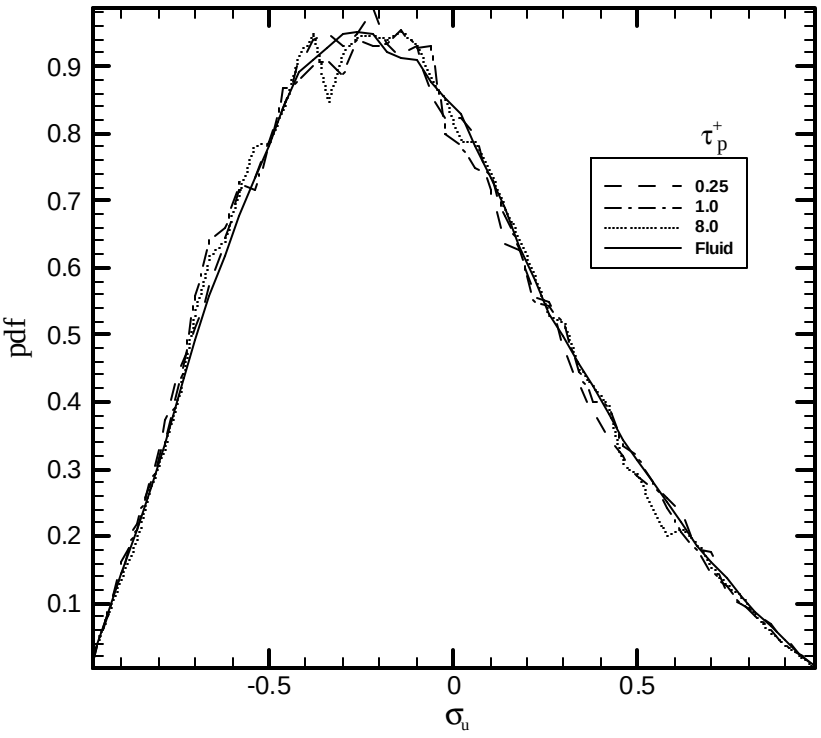

Figure 5.4.5: PDFs of σ_u in the Duct Center Region (x^+=177.2, y^+=177.2)

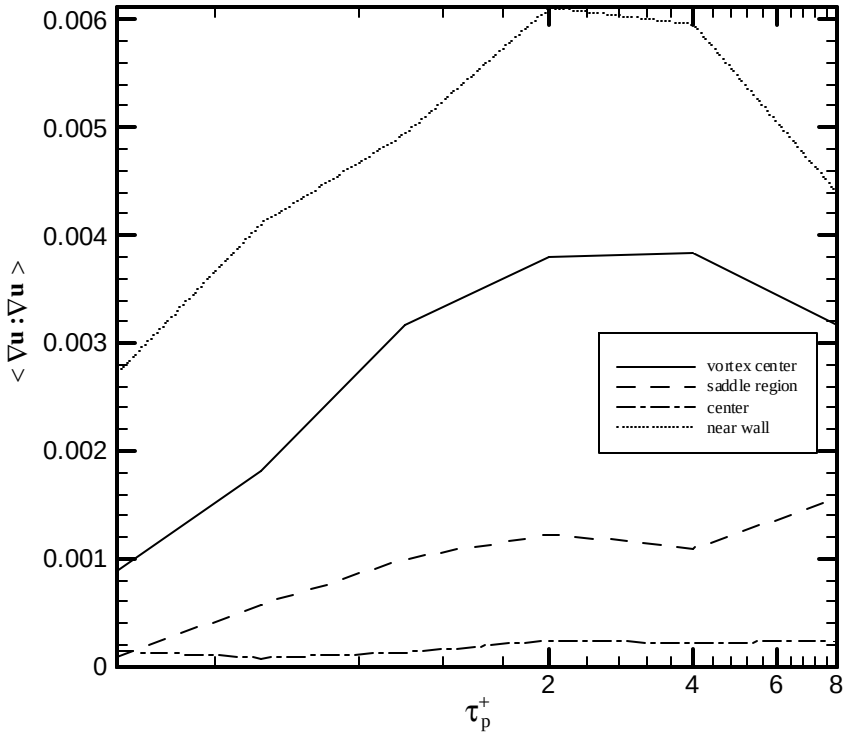

Figure 5.5.1: Mean Values of $\nabla \mathbf{u} : \nabla \mathbf{u}$

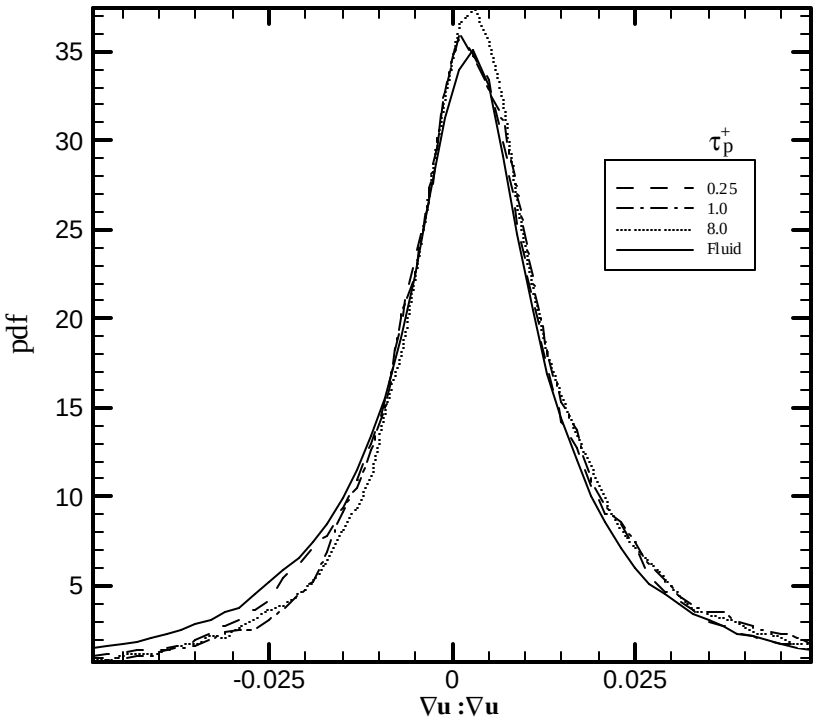

Figure 5.5.2: PDFs of $\nabla\mathbf{u}:\nabla\mathbf{u}$ in the Near Wall Region (x^+=177.2, y^+=19.8)

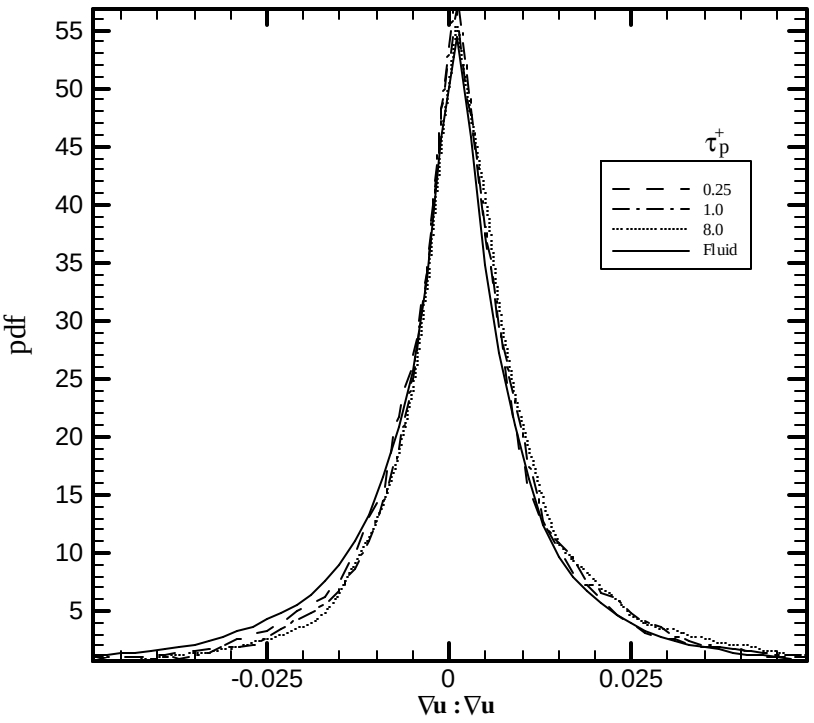

Figure 5.5.3: PDFs of $\nabla\mathbf{u}:\nabla\mathbf{u}$ in the Vortex Center Region (x^+=76.7, y^+=31.2)

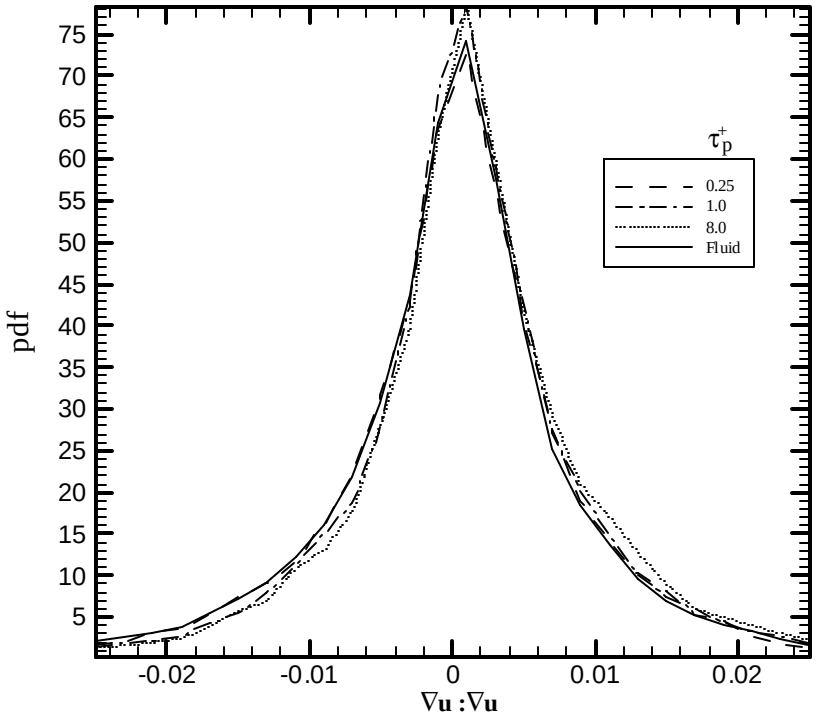

Figure 5.3.4: PDFs of $\nabla\mathbf{u}:\nabla\mathbf{u}$ in the Saddle Region (x^+=59.5, y^+=59.5)

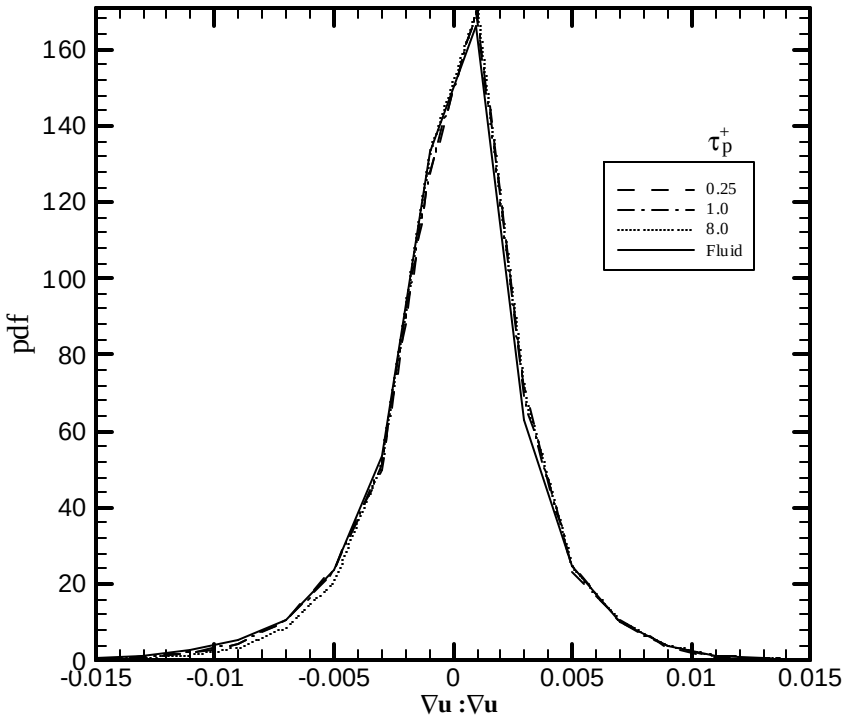

Figure 5.5.5: PDFs of $\nabla\mathbf{u}:\nabla\mathbf{u}$ in the Duct Center Region (x^+=177.2, y^+=177.2)

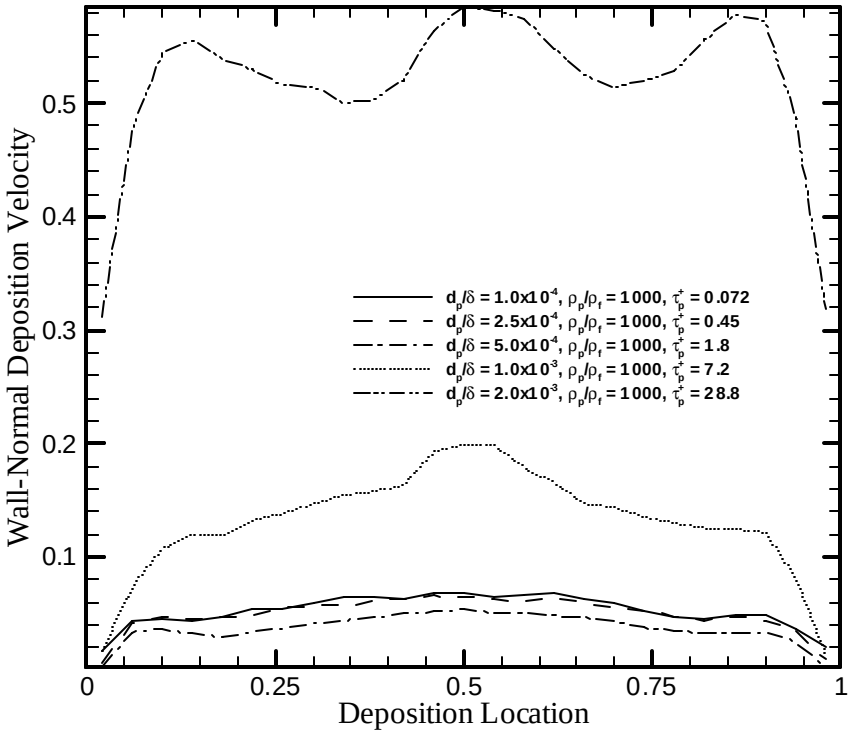

Figure 6.1.1.1: Wall-Normal Deposition Velocity, $\rho_p/\rho_f = 1000$, One-way Coupling

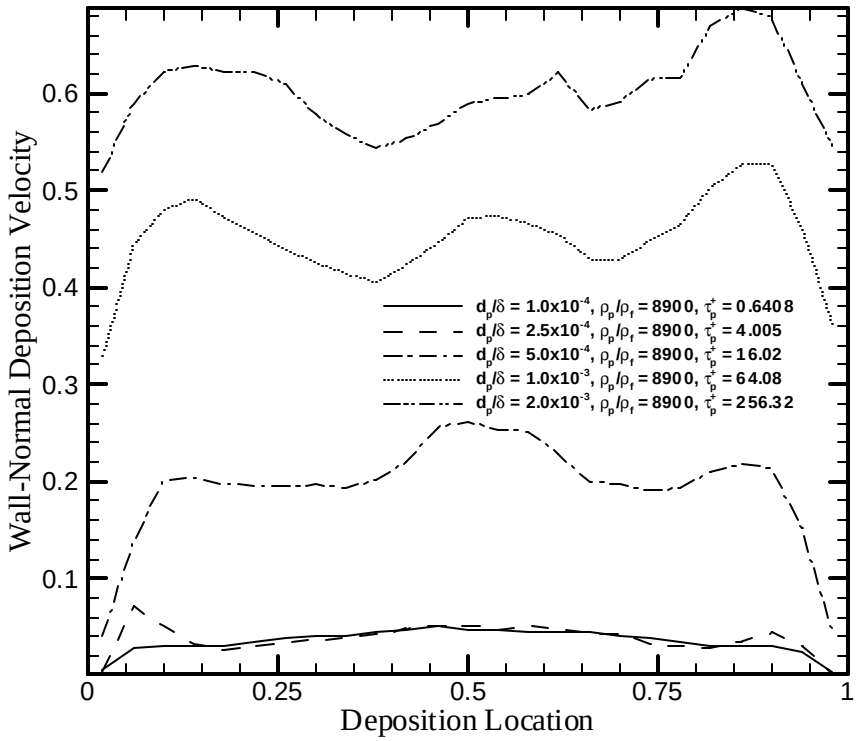

Figure 6.1.1.2: Wall-Normal Deposition Velocity, $\rho_p/\rho_f = 8900$, One-way Coupling

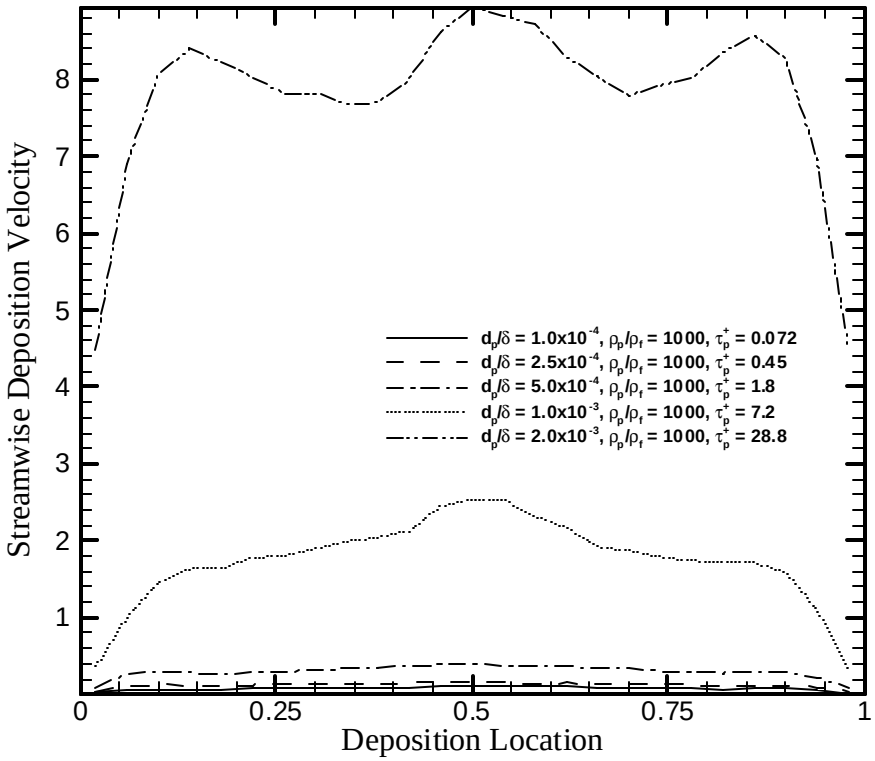

Figure 6.1.2.1: Streamwise Deposition Velocity, $\rho_p/\rho_f = 1000$, One-way Coupling

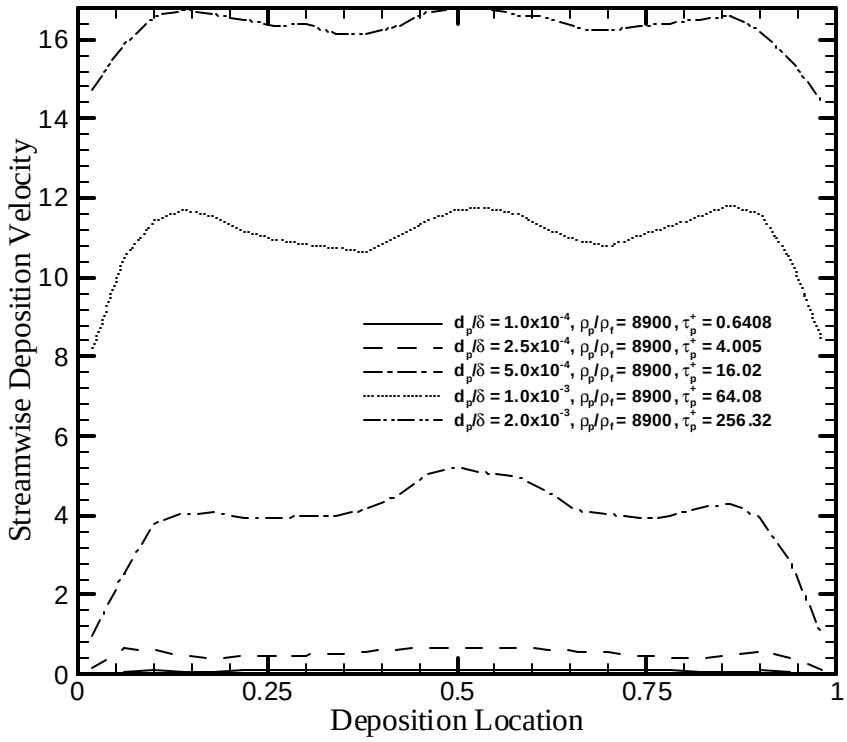

Figure 6.1.2.2: Streamwise Deposition Velocity, $\rho_p/\rho_f = 8900$, One-way Coupling

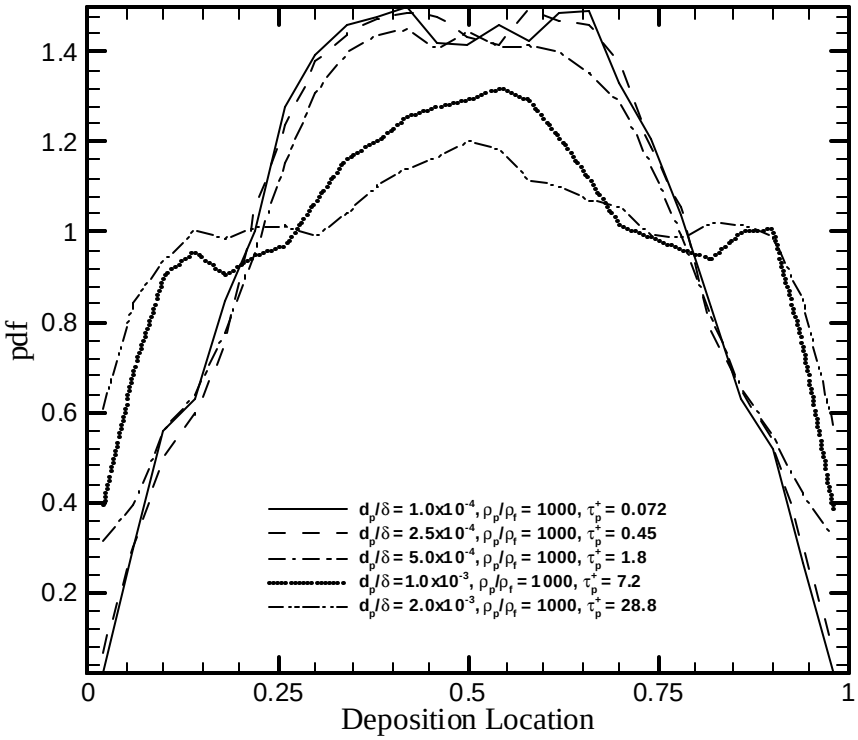

Figure 6.1.3.1: PDFs of Deposition Location, $\rho_p/\rho_f = 1000$, One-way Coupling

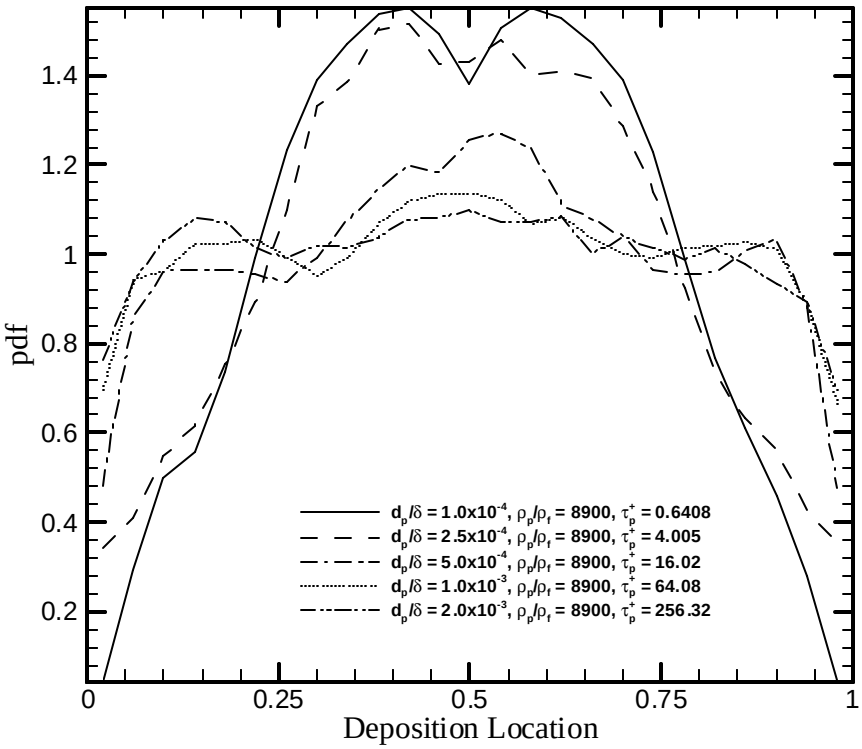

Figure 6.1.3.2: PDFs of Deposition Location, $\rho_p/\rho_f = 8900$, One-way Coupling

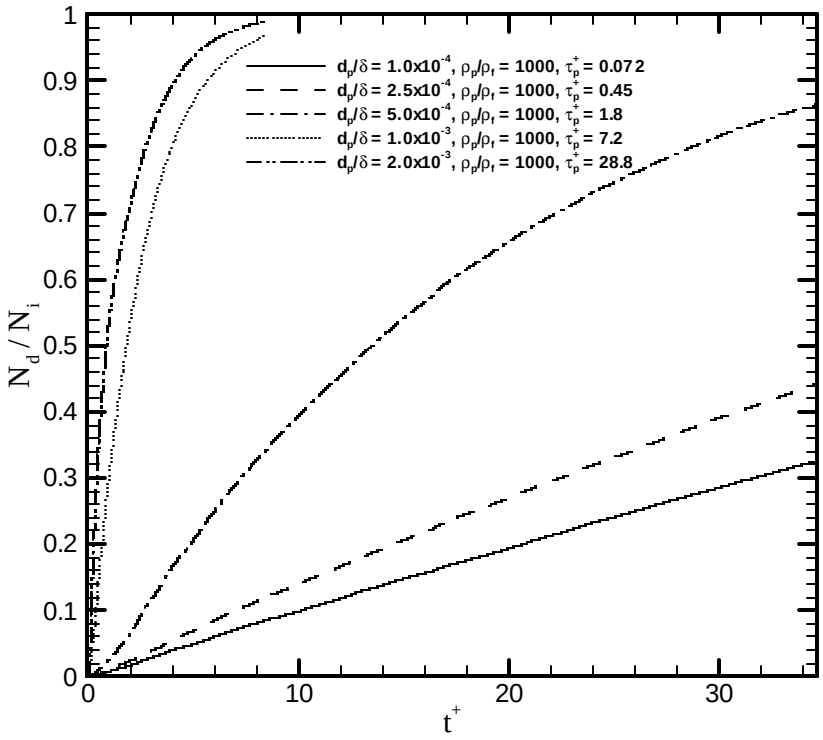

Figure 6.1.4.1: Time History of Particle Deposition, $\rho_p/\rho_f = 1000$, One-way Coupling

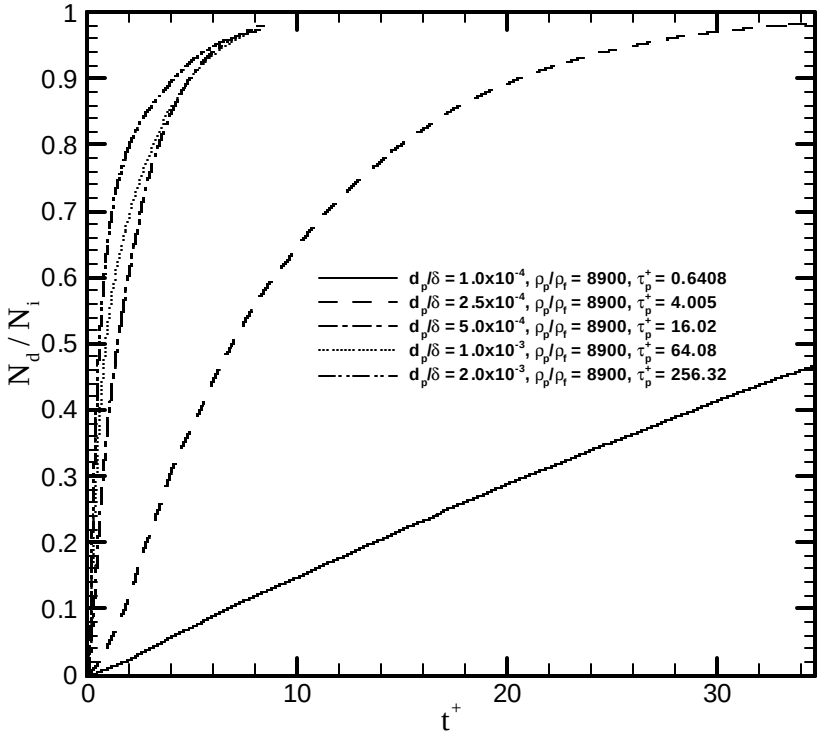

Figure 6.1.4.2: Time History of Particle Deposition, $\rho_p/\rho_f = 8900$, One-way Coupling

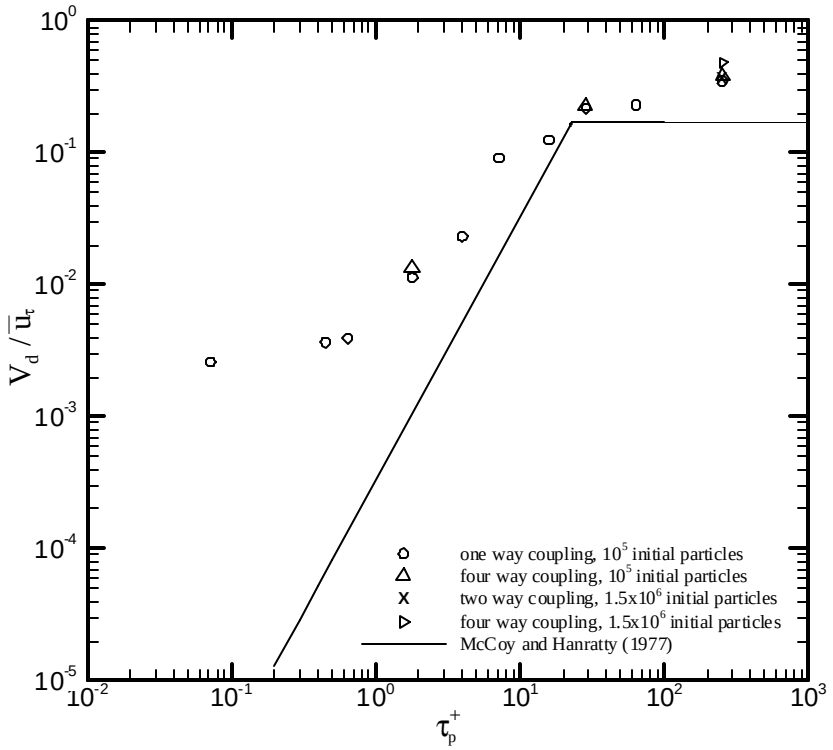

Figure 6.1.4.3: Deposition Rates Compared with Experimental Pipe Flow Data

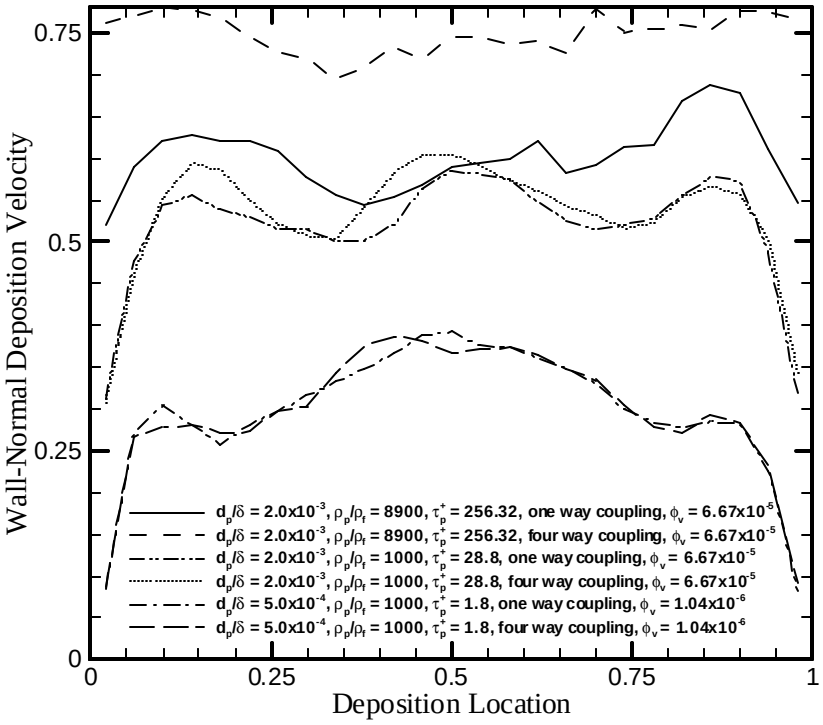

Figure 6.2.2.1: Wall-Normal Deposition Velocity, Four-way Coupling, 10^5 Initial Particles

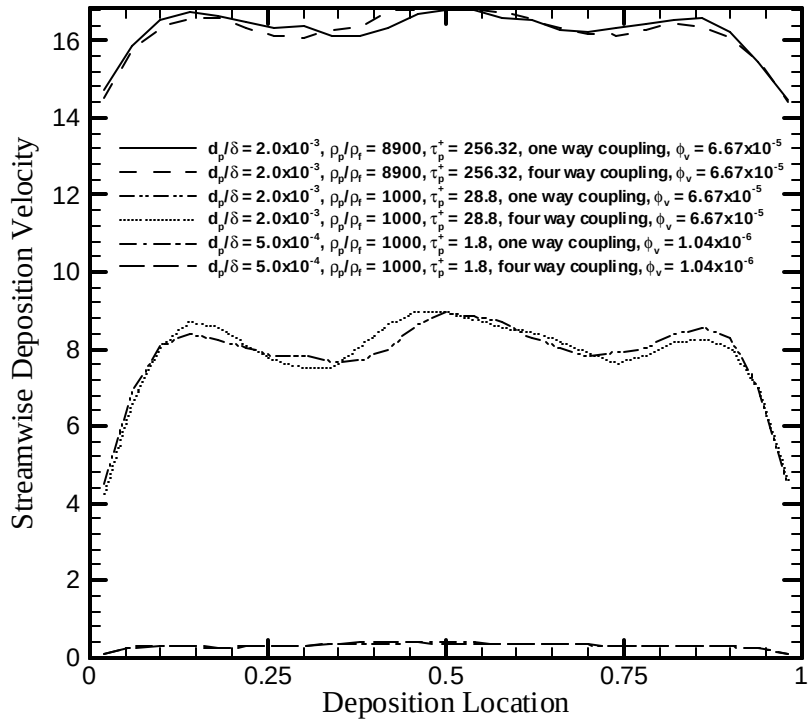

Figure 6.2.1.2: Streamwise Deposition Velocity, Four-way Coupling, 10^5 Initial Particles

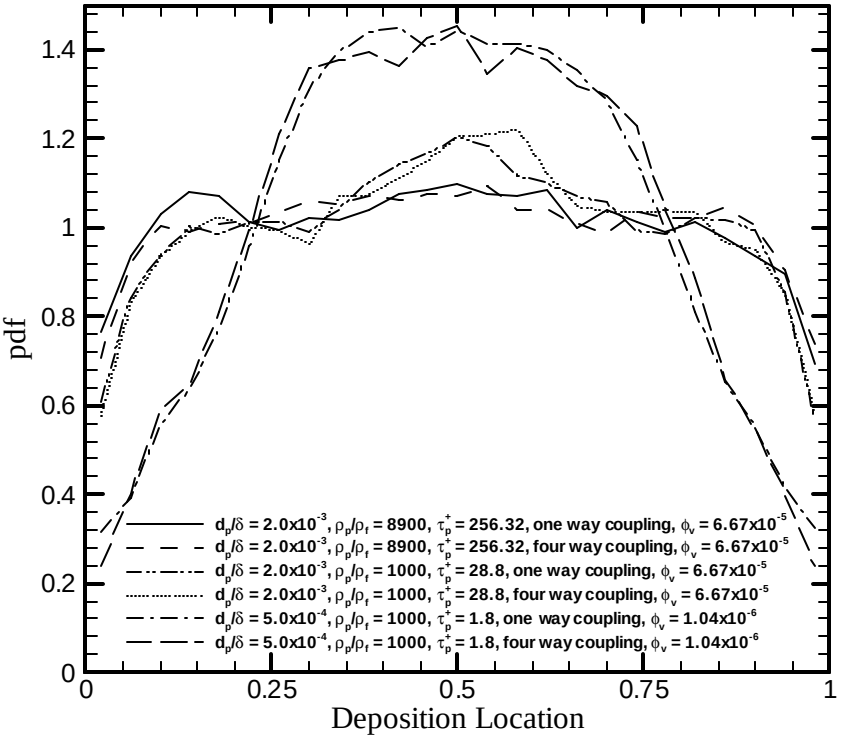

Figure 6.2.1.3: PDFs of Deposition Location, Four-way Coupling, 10^5 Initial Particles

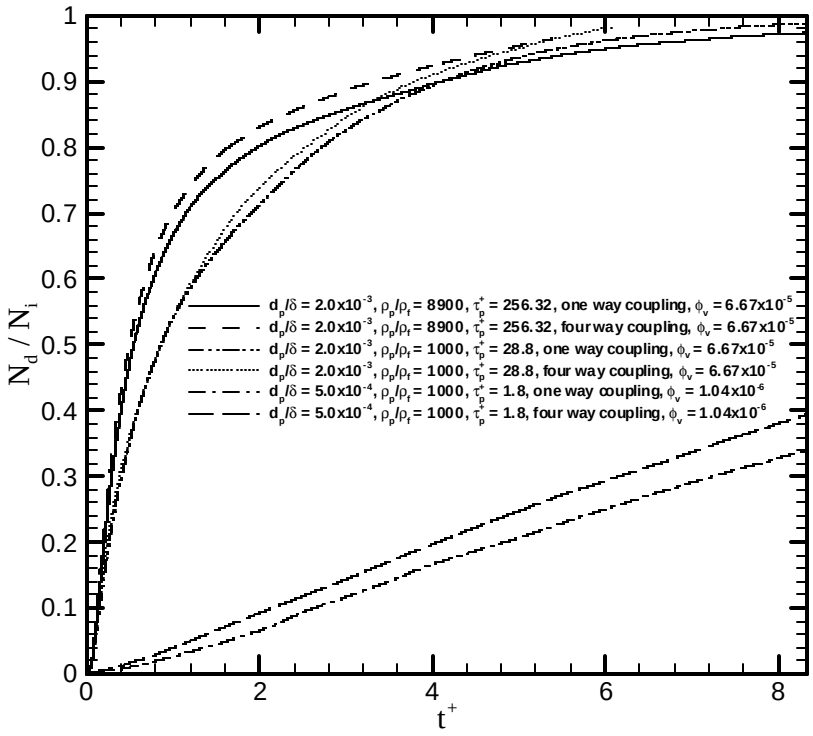

Figure 6.2.1.4: Time History of Particle Deposition, Four-way Coupling, 10^5 Initial Particles

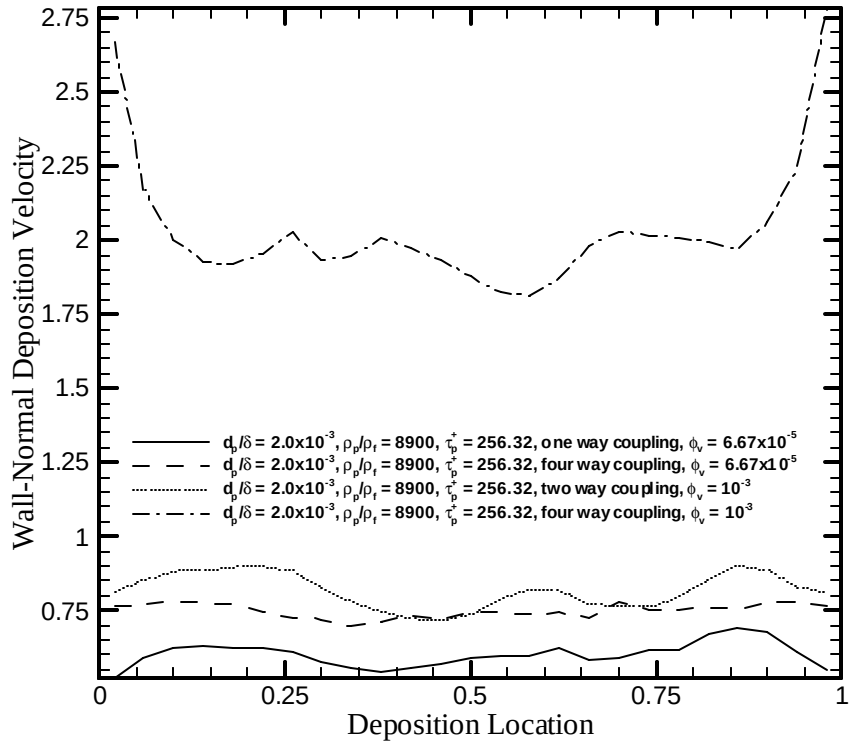

Figure 6.2.2.1: Wall-Normal Deposition Velocity, Two- and Four-way Coupling, Volume Fraction = 10^{-3}

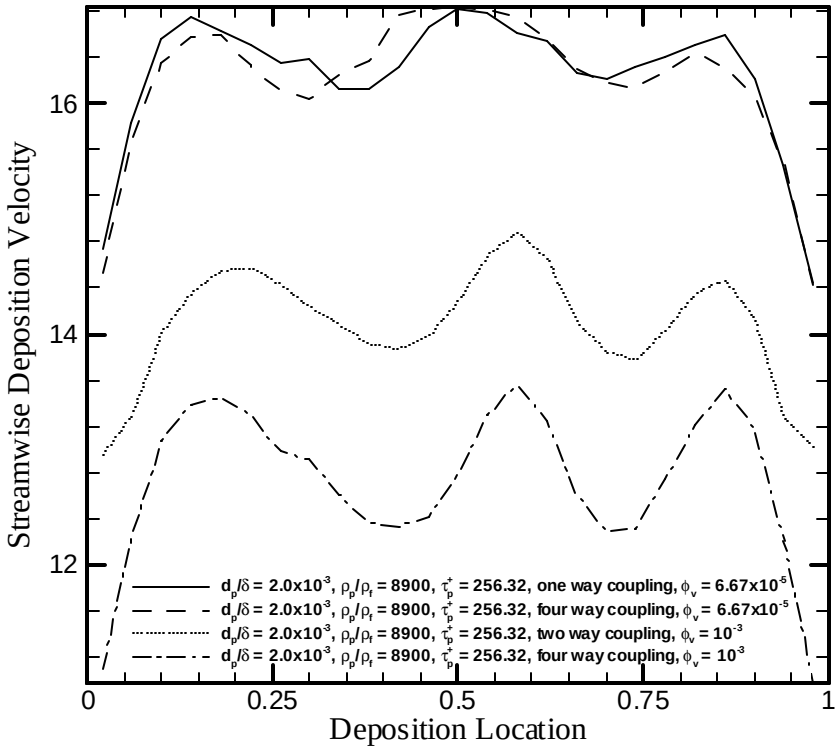

Figure 6.2.2.2: Streamwise Deposition Velocity, Two- and Four-way Coupling, Volume Fraction = 10^{-3}

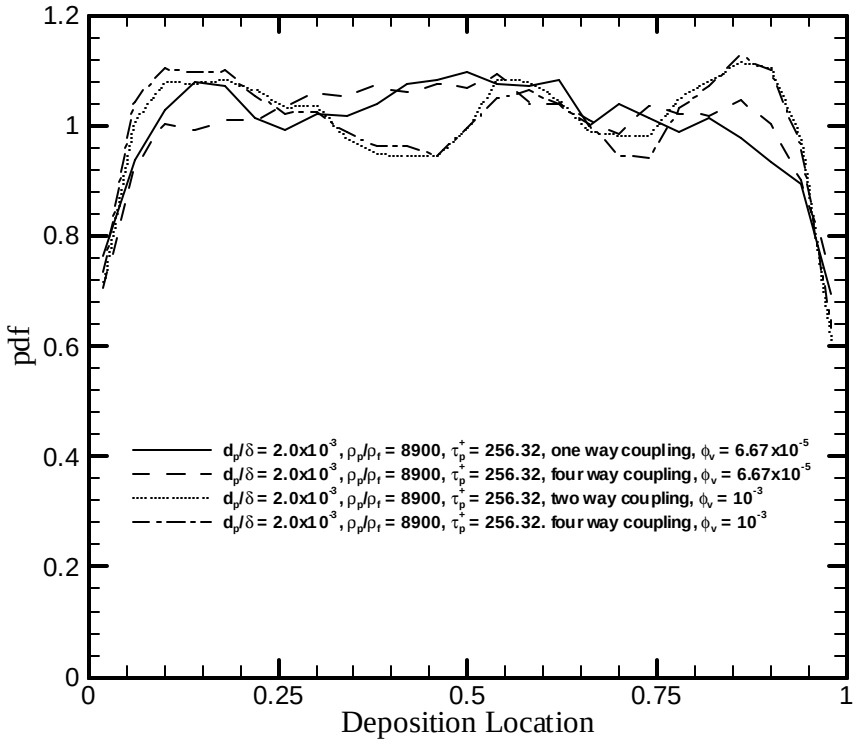

Figure 6.2.2.3: PDFs of Deposition Location, Two- and Four-way Coupling, Volume Fraction = 10^{-3}

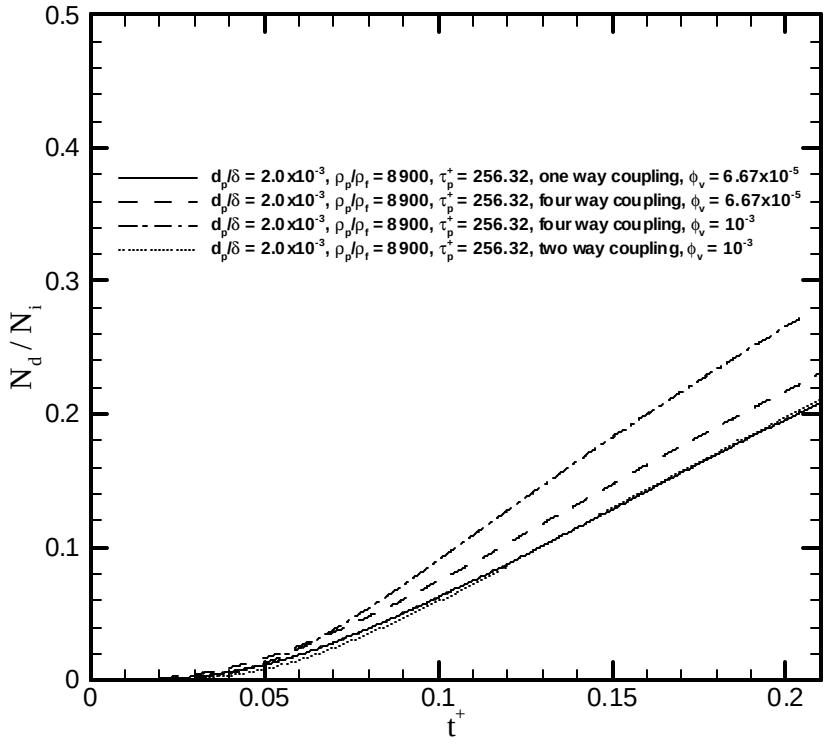

Figure 6.2.2.4: Time History of Particle Deposition, Two- and Four-way Coupling, Volume Fraction = 10^{-3}

Bibliography

Adrian, R. J., Balachandar, S., and Liu, Z. C., "Spanwise Growth of Vortex Structure in Wall Turbulence", Korean Soc. Mech. Engineers Int. J., **15**: pp. 1741-1749, 2001.

Armaly, B. F., Durst, F., Pereira, J. C. F., Schonung, B., "Experimental and Theoretical Investigation of Backward-Facing Step Flow", J. Fluid Mech., **127**: pp. 473-496, 1983.

Armenio, V., Piomelli, U., and Fiorotto, V., "Effect of Subgrid Scales on Particle Motion", Phys. Fluids, **11**(10): pp. 3030-3042, 1999.

Bajura, R. A. and Jones Jr., E. H., "Flow Distribution Manifolds", Transactions of the ASME, **98**(4): pp. 654-666, 1976.

Bajura, R. A., "A Model for Flow Distribution in Manifolds", Journal of Engineering for Power, 9**3**(1): pp. 7-12, 1971.

Bardina, J.E., Huang, P. G., and Coakley, T. J., "Turbulence Modeling Validation", AIAA Paper 97-2121, 1997.

Blackburn, H. M., "Channel Flow LES with Spectral Elements", 13th Australasian Fluid Mechanics Conference, Monsash University, Melbourne, Australia, 1998.

Boivin, M., Simonin, O., and Squires, K. D., "Direct Numerical Simulation of Turbulence Modulation by Particles in Isotropic Turbulence", J. Fluid Mech., **375**: pp. 235-263, 1998.

Boivin, M., Simonin, O., and Squires, K. D., "On the Prediction of Gas-Solid Flows with Two-Way Coupling Using Large Eddy Simulation", Phys. Fluids, **12**(8): pp. 2080-2090, 2000.

Bradshaw, P., "Turbulent Secondary Flows", Ann. Rev. Fluid Mech., **19**: pp. 53-74, 1987.

Brooke, J. W., Hanratty, T. J., and McLaughlin, J. B., "Free-Flight Mixing and Deposition of Aerosols", Phys. Fluids, **8**(10): pp. 3404-3415, 1994.

Brundrett, E., and Baines, W. D., "The Production and Diffusion of Vorticity in Duct Flow", J. Fluid Mech., **19**: pp. 375-394, 1964.

Cabuk, H. and Modi, V., "On the Design of Optimum Flow Headers for Heat Exchangers**",** ASME HTD National Heat Transfer Conference, 108: pp. 161-167, 1989.

Chen, M., Kontomaris, K., and McLaughlin, J. B., "Direct Numerical Simulation of Droplet Collisions in a Turbulent Channel Flow. Part I: Collision Algorithm", Int. J. Multiphase Flow, **24**: pp. 1079-1103, 1998.

Chisolm, D. and Wanniarachchi, A., "Maldistribution in Single-Pass Mixed Channel Plate Heat Exchangers", ASME HTD Compact Heat Exchangers for Power and Process Industries, **201**: pp. 95-99, 1992.

Chung, J. N., and Troutt, T. R., "Simulation of Particle Dispersion in an Axisymmetric Jet", J. Fluid Mech., **186**: pp. 199-222, 1988.

Clark, R. A., Ferziger, J. H., and Reynolds, W. C., "Evaluation of Subgrid-Scale Models Using an Accurately Simulated Turbulent Flow", J. Fluid Mech., **91**: pp. 1-16, 1979.

Crowe, C. T., Troutt, T. R., Chung, J. N., Davis, R. W., and Moore, E. F., "A Turbulent Flow without Particle Mixing", Aerosol Sci. and Tech., **22**: pp. 135-138, 1995.

Datta, A. B. and Majumdar, A. K., "A Calculation Procedure for Two Phase Flow Distribution in Manifolds With and Without Heat Transfer", Int. J. Heat Mass Transfer, **26**(9): pp. 1321-1328, 1983.

de Moura, L. F. M., "Experimental and Numerical Study on the Two-Phase Flow Distribution Between Two Passes of a Heat Exchanger", ASME FED Advances in Gas-Liquid Flows. **99**: pp. 267-273, 1990.

Demuren, A. O., and Rodi, W., "Calculation of Turbulence-driven Secondary Motion in Non-circular Ducts", J. Fluid Mech., **140**: pp. 189-222, 1984.

Drallmeier, J. A. and Peters, J. E., "Liquid- and Vapor-Phase Dynamics of a Solid-Cone Pressure Swirl Atomizer", Atomization and Sprays, **4**(2): pp. 135-158, 1994.

Druzhinin, O. A., and Elghobashi, S., "Direct Numerical Simulations of Bubble-Laden Turbulent Flows Using the Two-Fluid Formulation", Phys. Fluids, **10**(3): pp. 685-697, 1998.

Eggels, J. G. M., Unger, F., Weiss, M. H., Westerweel, J., Adrian, R. J., Friedrich, R., and Nieuwstadt, F. T. M., "Fully Developed Turbulent Pipe Flow: A Comparison between Direct Numerical Simulation and Experiment", J. Fluid Mech., **162**: pp. 175-209, 1994.

Elghobashi, S., "On Predicting Particle-Laden Turbulent Flows", Appl. Sci. Res., **52**: pp. 309-329, 1994.

Elghobashi, S., and Truesdell, G. C., "Direct Simulation of Particle Dispersion in a Decaying Isotropic Turbulence", J. Fluid Mech., **242**: pp. 655-700, 1992.

Elghobashi, S., and Truesdell, G. C., "On the Two-Way Interaction Between Homogeneous Turbulence and Dispersed Solid Particles. I: Turbulence Modification", Phys. Fluids, **5**(7): pp. 1790-1801, 1993.

Ferry, J. and Balachandar, S., "A Fast Eulerian Method for Disperse Two-Phase Flow", Int. J. Multiphase Flow, **27**: pp. 1199-1226, 2001.

Fessler, J. R., and Eaton, J. K., "Particle Response in a Planar Sudden Expansion Flow", Experimental Thermal and Fluid Science, **15**: pp. 413-423, 1997.

Fessler, J. R., and Eaton, J. K., "Turbulence Modification by Particles in a Backward-Facing Step Flow", J. Fluid Mech., **394**: pp. 97-117, 1999.

Fessler, J. R., Kulick, J. D., and Eaton, J. K., "Preferential Concentration of Heavy Particles in a Turbulent Channel Flow", Phys. Fluids, **6**(11): pp. 3742-3749, 1994.

Gavrilakis, S., "Numerical Simulation of Low-Reynolds-number Turbulent Flow Through a Straight Square Duct", J. Fluid Mech., **244**: pp. 101-129, 1992.

Germano, M., "A Statistical Formulation of the Dynamic Model", Phys. Fluids, **8**(2): pp. 565-570, 1996.

Germano, M., Piomelli, U., Moin, P., and Cabot, W. H., "A Dynamic Subgrid-Scale Eddy Viscosity Model", Phys. Fluids, **3**(7): pp. 1760-1765, 1991.

Ghosal, S., Lund, T. S., Moin, P., and Akselvoll, K., "A Dynamic Localization Model for Large-Eddy Simulation of Turbulent Flows", J. Fluid Mech., **286**: pp. 229-255, 1995.

Gresho, P. M., Gartling, D. K., Torczynski, J. R., Cliffe, K. A., Winters, K. H., Garratt, T. J., Spence, A., and Goodrich, J. W., "Is the Steady Viscous Incompressible Two-Dimensional Flow Over a Backward-Facing Step at Re = 800 Stable?", Int. J. for Numerical Methods in Fluids, **17**: pp. 501-541, 1993.

Gullbrand, J., "An Evaluation of a Conservative Fourth Order DNS Code in Turbulent Channel Flow", Center for Turbulence Research Annual Research Briefs: pp. 211-218, 2000.

Gullbrand, J., Bai, X. S., and Fuchs, L., "Large Eddy Simulation of Turbulent Reacting Flows Using Cartesian Grid and Boundary Corrections", 34th AIAA/ASME/SAE/ASEE Joint Propulsion Conference & Exhibit, Cleveland, OH, 1998.

Hopkins, M. A., and Louge, M. Y., "Inelastic Microstructure in Rapid Granular Flows of Smooth Discs", Phys. Fluids, **3**(1): pp. 47-57, 1991.

Horiuti, K., "Large Eddy Simulation of Turbulent Channel Flow by One-Equation Modeling", J. Physical Society of Japan, **54**(8): pp. 2855-2865, 1985.

Huser, A., and Biringen, S., "Direct Numerical Simulation of Turbulent Flow in a Square Duct", J. Fluid Mech., **257**: pp. 65-95, 1993.

Johansen, H., and Colella, P., "A Cartesian Grid Embedded Boundary Method for Poisson's Equation on Irregular Domains", J. Comp. Physics, **147**: pp. 60-85, 1998.

Jones, G. F. and Galliera, J. M., "Isothermal Flow Distribution in Coupled Manifolds: Comparison of Results from CFD and an Integral Model" ASME FED. **247**: pp. 189-195, 1998.

Jordan, S. A., and Ragab, S. A., "On the Unsteady and Turbulent Characteristics of the Three-Dimensional Shear-Driven Cavity." ASME Journal of Fluids Engineering**, 116**(3): pp. 439-449, 1994.

Kajishima, T., and Miyake, Y., "A Discussion on Eddy Viscosity Models on the Basis of the Large Eddy Simulation of Turbulent Flow in a Square Duct", Computers Fluids, **21**(2): pp. 151-161, 1992.

Kim, J., Moin, P., and Moser, R., "Turbulence Statistics in Fully Developed Channel Flow at Low Reynolds Number", J. Fluid Mech., **177**: pp. 133-166, 1987.

Kim, S., Choi, E., and Cho, Y., "The Effect of Header Shapes on the Flow Distributions in a Manifold for Electronic Packaging Applications", Int. Communications in Heat and Mass Transfer, **22**(3): pp. 329-341, 1995.

Kim, W. W. and Menon, S., "Application of the Localized Dynamic Subgrid-Scale Model to Turbulent Wall-Bounded Flows", AIAA 97-0210, 1997.

Kim, W., and Menon, S., "A New Dynamic One-Equation Subgrid-Scale Model for Large Eddy Simulations", 33rd Aerospace Sciences Meeting and Exhibit, Reno, NV, 1995.

Kulick, J. D., Fessler, J. R., and Eaton, J. K., "Particle Response and Turbulence Modification in Fully Developed Channel Flow", J. Fluid Mech., **277**: pp. 109-134, 1994.

Langford, J. A. "Toward Ideal Large Eddy Simulation", Thesis, Theoretical and Applied Mechanics, Urbana, IL, University of Illinois at Urbana-Champaign**:** 2000.

Launder, B. E., and Spalding, D. B., "Mathematical Models of Turbulence", Academic Press, London, 1972.

Launder, B.E., Reece, G. J., and Rodi, W., "Progress in the Development of a Reynolds-Stress Turbulence Closure", J. Fluid Mech., **68**: pp. 537-566, 1975.

Lazaro, B. J., and Lasheras, J. C., "Particle Dispersion in the Developing Free Shear Layer. Part I. Unforced Flow", J. Fluid Mech., **235**: pp. 143-178, 1992a.

Lazaro, B. J., and Lasheras, J. C., "Particle Dispersion in the Developing Free Shear Layer. Part 2. Forced Flow", J. Fluid Mech., **235**: pp. 179-221, 1992b.

Le, H., Moin, P., and Kim, J., "Direct Numerical Simulation of Turbulent Flow Over a Backward-Facing Step", J. Fluid Mech., **330**: pp. 349-374, 1997.

Lesieur, M., and Metais, O., "New Trends in Large-Eddy Simulations of Turbulence", Annu. Rev. Fluid Mech., **28**: pp. 45-82, 1996.

Lilly, D. K., "A Proposed Modification of the Germano Subgrid-scale Closure Model", Phys. Fluids, **4**(3): pp. 633-635, 1992.

Ling, W., Chung, J. N., Troutt, T. R., and Crowe, C. T., "Direct Numerical Simulation of a Three-Dimensional Temporal Mixing Layer with Particle Dispersion" J. Fluid Mech., **358**: pp. 61-85, 1998.

Liu, S., Meneveau, C., and Katz, J., "Experimental Studies of Similarity Subgrid-Scale Models of Turbulence in the Far-Field of a Jet", App. Sci. Res., **54**: pp. 177-190, 1995.

Longmire, E. K., and Eaton, J. K., "Structure of a Particle-Laden Round Jet", J. Fluid Mech., **236**: pp. 217-257, 1992.

Loth, E., "Numerical Approaches for Motion of Dispersed Particles, Droplets and Bubbles", Progress in Energy and Combustion Science, **26**, pp. 161-223, 2000.

Madabhushi, R. K., "Direct and Large Eddy Simulation of Turbulent Flow in a Square Duct", Thesis, Dept. of Mech. Eng., Univ. of Illinois at Urbana-Champaign: 1993.

Madabhushi, R. K., and Vanka, S. P., "Direct Numerical Simulations of Turbulent Flow in a Square Duct at Low Reynolds Number", *Near-Wall Turbulent Flows* (R. M. C. So, C. G. Speziale, and B. E. Launder, Editors), Elsevier, pp. 297-306, 1993.

Madabhushi, R. K., and Vanka, S. P., "Large Eddy Simulation of Turbulence-Driven Secondary Flow in a Square Duct", Phys. Fluids, **3**(11): pp. 2734-2745, 1991.

Maxey, M. R., "The Gravitational Settling of Aerosol Particles in Homogeneous Turbulence and Random Flow Fields", J. Fluid Mech., **174**: pp. 441-465, 1987.

Maxey, M. R., and Riley, J. J., "Equation of Motion for a Small Rigid Sphere in a Nonuniform Flow", Phys. Fluids, **26**(4): pp. 883-889, 1983.

McCoy, D. D., and Hanratty, T. J., "Rate of Deposition of Droplets in Annular Two-Phase Flow", Int. J. Multiphase Flow, **3**: pp. 319-331, 1977.

Meneveau, C., and Katz, J., "Scale-Invariance and Turbulence Models for Large-Eddy Simulation", Annual Rev. Fluid Mech., **32**: pp. 1-32, 2000.

Meneveau, C., Lund, T. S., and Cabot, W. H., "A Lagrangian Dynamic Subgrid-Scale Model of Turbulence", J. Fluid Mech., **319**: pp. 353-385, 1996.

Menon, S., Yeung, P., and Kim, W., "Effect of Subgrid Models on the Computed Interscale Energy Transfer in Isotropic Turbulence", Computers & Fluids, **25**(2): pp. 165-180, 1996.

Menter, F. R., "Two-Equation Eddy-Viscosity Turbulence Models for Engineering Applications", AIAA Journal, **32**: pp. 1299-1310, 1994.

Moin, P., "Numerical and Physical Issues in Large Eddy Simulation of Turbulent Flows", JSME Intl. J. Series B - Fluids and Thermal Engineering, **41**(2): pp. 454-463, 1998.

Moser, R. D., J. Kim, and N. N. Mansour, "Direct Numerical Simulation of Turbulent Channel Flow up to Re_t = 590", Phys. Fluids, **11:** pp. 943–945, 1999.

Neto, A. S., Grand, D., Metais, O., and Lesieur, M., "A Numerical Investigation of the Coherent Vortices in Turbulence Behind a Backward-Facing Step", J. Fluid Mech., **256**: pp. 1-25, 1993.

Nikitin, N. V., Nicoud, F., Wasistho, B., Squires, K. D., and Spalart, P. R., "An Approach to Wall Modeling in Large-Eddy Simulations", Phys. Fluids, **12**(7): pp. 1629-1632, 2000.

Nikuradse, J., "Turbulente Strömungen in Nichtkeisformigen Rohren", Ing. Arch., **1**: pp. 306-332, 1930.

Pan, Y., Tanaka, T., and Tsuji, Y., "Turbulence Modulation by Dispersed Solid Particles in Rotating Channel Flows", Int. J. Multiphase Flow, **28**: pp. 527-552, 2002.

Paris, A. D., and Eaton, J. K., "PIV Measurements in a Particle-Laden Channel Flow", 3rd ASME/JSME Joint Fluids Engineering Conference, San Francisco, CA, 1999.

Parthasarathy, R. N., and Faeth, G. M., "Turbulence Modulation in Homogeneous Dilute Particle-Laden Flows", J. Fluid Mech., **220**: pp. 485-514, 1990a.

Parthasarathy, R. N., and Faeth, G. M., "Turbulent Dispersion of Particles in Self-Generated Homogeneous Turbulence", J. Fluid Mech., **220**: pp. 515-537, 1990b.

Pedinotti, S., Mariotti, G., and Banerjee, S., "Direct Numerical Simulation of Particle Behaviour in the Wall Region of Turbulent Flows in Horizontal Channels", Int. J. Multiphase Flow, **18**(6): pp. 927-941, 1992.

Piomelli, U., Cabot, W. H., Moin, P., and Lee, S., "Subgrid-Scale Backscatter in Turbulent and Transitional Flows", Phys. Fluids, **3**(7): pp. 1766-1771, 1991.

Piomelli, U., Ferziger, J., and Moin, P., "Models for Large Eddy Simulations of Turbulent Channel Flows Including Transpiration", Tech. Report TF-32, Department of Mechanical Engineering, Stanford University, 1987.

Prandtl, L. "Essentials of Fluid Dynamics", Blackie and Son, London, 1952.

Rong, X., Kawaji, M. and Burgers, J. G., "Two-Phase Header Flow Distribution in a Stacked Plate Heat Exchanger", ASME FED Gas-Liquid Flows. **225**: pp. 115-122, 1995.

Samson, E. B., Stark, J. A. and Grote, M. G., "Two-Phase Flow Header Tests", SAE Technical Paper Series, Paper 871440, 1988.

Schmidt, H., and Schumann, U., "Coherent Structure of the Convective Boundary Layer Derived from Large-Eddy Simulation", J. Fluid Mech. **200**: pp. 511-562, 1989.

Schumann, U., "Subgrid Length-Scales for Large-Eddy Simulation of Stratified Turbulence", Theoret. Comput. Fluid Dynamics, **2**: pp. 279-290, 1991.

Schumann, U., "Subgrid Scale Model for Finite Difference Simulations of Turbulent Flows in Plane Channels and Annuli", J. Computational Physics, **18**: pp. 376-404, 1975.

Simons, T. A., and Pletcher, R. H., "Large Eddy Simulation of Turbulent Flows Using Unstructured Grids", 34th AIAA/ASME/SAE/ASEE Joint Propulsion Conference & Exhibit, Cleveland, OH, 1998.

Soteriou, M. C., and Yang, X., "Particle Dispersion in Variable Density and Viscosity Shear Flows", Phys. Fluids, **11**(6): pp. 1373-1386, 1999.

Speziale, C.G., "On Nonlinear k-l and k-epsilon Models of Turbulence", J. Fluid Mech., **178**: pp. 459-475, 1987.

Squires, K. D. and Eaton, J. K., "Preferential Concentration of Particles By Turbulence", Phys. Fluids, **3**(5): pp. 1169-1178, 1991b.

Squires, K. D., and Eaton, J. K., "Measurements of Particle Dispersion Obtained from Direct Numerical Simulations of Isotropic Turbulence", J. Fluid Mech., **226**: pp. 1-35, 1991a.

Squires, K. D., and Eaton, J. K., "Particle Response and Turbulence Modification in Isotropic Turbulence", Phys. Fluids, **2**(7): pp. 1191-1203, 1990.

Stokes, S. D., Glauser, M. N., and Gatski, T. B., "An Examination of a 3D Corner-Step Experiment", Experimental Thermal and Fluid Science **17**: pp. 132-138, 1998.

Sundaram, S., and Collins, L. R., "A Numerical Study of the Modulation of Isotropic Turbulence by Suspended Particles", J. Fluid Mech., **379**, pp. 105-143, 1999.

Sundaram, S., and Collins, L.R., "Numerical Considerations in Simulating a Turbulent Suspension of Finite-Volume Particles", J. Comp. Physics, **124**(2): pp. 337-350, 1996.

Tafti, D. K., and Vanka, S. P., "Large Eddy Simulation of Channel Flow Using Finite-Difference Techniques." Comp. Fluid Dynamics Laboratory Report CFD 90-01, University of Illinois, 1990.

Tageldin, M. S., and Cetegen, B. M., "Development of Mixing and Dispersion in an Isothermal, Droplet-laden, Confined Turbulent Mixing Layer", Combust. Sci. and Tech, **130**: pp. 131-169, 1997.

Thangam, S., and Hur, N., "A Highly-Resolved Numerical Study of Turbulent Flow Past a Backward-Facing Step", Int. J. Engng. Sci., **29**(5): pp. 607-615, 1991.

Thangam, S., and Speziale, C. G., "Turbulent Flow Past a Backward-Facing Step: A Critical Evaluation of Two-Equation Models", AIAA Journal **30**(5): pp. 1314-1320, 1992.

Uijttewaal, W. S. J., and Oliemans, R. V. A., "Particle Dispersion and Deposition in Direct Numerical and Large Eddy Simulations of Vertical Pipe Flows", Phys. Fluids, **8**(10): pp. 2590-2604, 1996.

van Haarlem, B., Boersma, B. J., and Nieustadt, F. T. M., "Direct Numerical Simulation of Particle Deposition onto a Free-Slip and No-Slip Surface", Phys. Fluids, **10**(10): pp. 2608-2620, 1998.

Vance, M. W., and Squires, K. D., "An Approach to Parallel Computing in an Eulerian-Lagrangian Two-Phase Flow Model", Proceedings of ASME FED, 2002 ASME FED Summer Conference, July 14-18, 2002, Montreal, Quebec, Canada.

Volker, S., "Optimal Large-Eddy Simulation of Turbulent Channel Flow", Dept. Mechanical Engineering. Urbana, IL, University of Illinois at Urbana-Chapaign**:** 2000.

Vreman, B., Geurts, B., and Kuerten, H., "Large-Eddy Simulation of the Turbulent Mixing Layer", J. Fluid Mech., **339**: pp. 357-390, 1997.

Wang, Q., and Squires, K. D., "Large Eddy Simulation of Particle Deposition in a Vertical Turbulent Channel Flow", Int. J. Multiphase Flow, **22**(4): pp. 667-683, 1996a.

Wang, Q., and Squires, K. D., "Large Eddy Simulation of Particle-Laden Channel Flow", Phys. Fluids, **8**(5): pp. 1207-1223, 1996b.

Wang, Q., Squires, K. D., Chen, M., and McLaughlin, J. B., "On the Role of the Lift Force in Turbulence Simulations of Particle Deposition", Int. J. Multiphase Flow, **23**(4): pp. 749-763, 1997.

Wang, X. and Peizhen, Y., "Isothermal Flow Distribution in Header Systems", Int. J. Solar Energy, **7**: pp. 159-169, 1989.

Wang, Y., and James, P. W., "On the Effect of Anisotropy on the Turbulent Dispersion and Deposition of Small Particles", Int. J. Multiphase Flow, **25**: pp. 551-558, 1999.

Winkler, C. M., and Peters, J. E., "Refrigerant Droplet Size Measurements in Conjunction with a Novel Method for Improving Flow Distribution in Evaporators", Aerosol Sci. and Technology, **36**: pp. 734-741, 2002.

Winkler, C. M., Rani, S. L., and Vanka, S. P., "Large Eddy Simulations of Particle Deposition in a Fully Developed Turbulent Square Duct Flow", submitted to Int. J. Multiphase Flow.

Winkler, C. M., Rani, S. L., and Vanka, S. P., "Preferential Concentration of Particles in a Fully Developed Turbulent Square Duct Flow", submitted to Int. J. Multiphase Flow.

Xu, H., and Pollard, A., "Large Eddy Simulation of Turbulent Flow in a Square Annular Duct", Phys. Fluids, **13**(11): pp. 3321-3337, 2001.

Yamamoto, Y., Potthoff, M., Tanaka, T., Kajishima, T., and Tsuji, Y., "Large-Eddy Simulation of Turbulent Gas-Particle Flow in a Vertical Channel: Effect of Considering Inter-Particle Collisions", J. Fluid Mech., **442**: pp. 303-334, 2001.

Yang, Y., Crowe, C. T., Chung, J. N., and Troutt, T. R., "Experiments on Particle Dispersion in a Plane Wake", Int. J. Multiphase Flow, **26**: pp. 1583-1607, 2000.

Ye, T., Mittal, R., Udaykuman, H. S., and Shyy, W., "An Accurate Cartesian Grid Method for Viscous Incompressible Flows with Complex Immersed Boundaries", J. Comp. Physics, **156**: pp. 209-240, 1999.

Yeh, T. T. and Mattingly, G. E., "Laser Doppler Velocimeter Studies of the Pipeflow Produced by a Generic Header", National Institute of Standards and Technology NISTIR 1409, 1995.

Yeung, P. K., and Pope, S. B., "Lagrangian Statistics from Direct Numerical Simulations of Isotropic Turbulence", J. Fluid Mech., **207**: p. 531-586, 1989.

Yoshizawa, A., "A Statistically-Derived Subgrid Model for the Large-Eddy Simulation of Turbulence", Phys. Fluids, **25**(9): pp. 1532-1538, 1982.

Zang, Y., Street, R. L., and Koseff, J. R., "A Dynamic Mixed Subgrid-Scale Model and its Application to Turbulent Recirculating Flows", Phys. Fluids, **5**(12): pp. 3186-3196, 1993.

Zhang, H., and Ahmadi, G., "Aerosol Particle Transport and Deposition in Vertical and Horizontal Turbulent Duct Flow", J. Fluid Mech., **406**: pp. 55-80, 2000.

Zhou, J., Adrian, R. J., Balachandar, S., and Kendall, T. M., "Mechanisms for Generating Coherent Packets of Hairpin Vortices in Channel Flow", J. Fluid Mech., **387**: pp. 353-396, 1998.